COOLING RATES FOR RELATIVISTIC ELECTRONS UNDERGOING COMPTON SCATTERING IN STRONG MAGNETIC FIELDS

MATTHEW G. BARING[1], ZORAWAR WADIASINGH[1], AND PETER L. GONTHIER[2]

[1] Department of Physics and Astronomy, MS 108, Rice University, Houston, TX 77251, USA; baring@rice.edu, zw1@rice.edu
[2] Department of Physics, Hope College, 27 Graves Place, Holland, MI 49423, USA; gonthier@hope.edu

ABSTRACT

For inner magnetospheric models of hard X-ray and gamma-ray emission in high-field pulsars and magnetars, resonant Compton upscattering is anticipated to be the most efficient process for generating continuum radiation. This is in part due to the proximity of a hot soft photon bath from the stellar surface to putative radiation dissipation regions in the inner magnetosphere. Moreover, because the scattering process becomes resonant at the cyclotron frequency, the effective cross section exceeds the classical Thomson value by over two orders of magnitude, thereby enhancing the efficiency of continuum production and the cooling of relativistic electrons. This paper presents computations of the electron cooling rates for this process, which are needed for resonant Compton models of non-thermal radiation from such highly magnetized pulsars. The computed rates extend previous calculations of magnetic Thomson cooling to the domain of relativistic quantum effects, sampled near and above the quantum critical magnetic field of 44.13 TG. This is the first exposition of fully relativistic, quantum magnetic Compton cooling rates for electrons, and it employs both the traditional Johnson & Lippmann cross section and a newer Sokolov & Ternov (ST) formulation of Compton scattering in strong magnetic fields. Such ST formalism is formally correct for treating spin-dependent effects that are important in the cyclotron resonance and has not been addressed before in the context of cooling by Compton scattering. The QED effects are observed to profoundly lower the rates below extrapolations of the familiar magnetic Thomson results, as expected, when recoil and Klein–Nishina reductions become important.

Key words: gamma rays: general – magnetic fields – pulsars: general – radiation mechanisms: non-thermal – stars: neutron

Online-only material: color figures

1. INTRODUCTION

Soft gamma-ray repeaters (SGRs) and anomalous X-ray pulsars (AXPs) are astrophysical sources, typically associated with supernova remnants (e.g., AXP 1841-045 associated with the remnant Kes 73, see Vasisht & Gotthelf 1997), that are thought to be magnetars, ultramagnetized isolated neutron stars. Observational evidence for supernova associations of magnetar candidates are discussed in Gaensler (2004) and Vink (2008). The magnetar model was first proposed by Duncan & Thompson (1992) for SGRs and then later extended to AXPs (Thompson & Duncan 1996). They are defined by their high spin-down rates and long periods (2–12 s) in their X-ray and soft gamma-ray pulsations, suggesting characteristically short ages $<10^5$ yr and high inferred surface polar fields, $B_0 \sim 10^{13}$–10^{15} G (e.g., Vasisht & Gotthelf 1997). Quiescent X-ray emission has been observed in both AXPs and SGRs (Tiengo et al. 2002) and although counterparts have been observed in the radio or optical/infrared (Camilo et al. 2006), the bulk of observed bolometric luminosity is in the X-ray band. In both SGRs and AXPs, high persistent X-ray luminosity $\sim 10^{35}$ erg s^{-1} typically exceeds the classical electromagnetic dipolar rotational energy loss rates by two to three orders of magnitude, suggesting an energy source not of rotational spin-down origin, i.e., contrasting the case for the multitude of young radio and gamma-ray pulsars.

Long timescale flux variability is generally low for quiescent 2–10 keV band emission in both SGRs and AXPs. However, bursting activity typical of SGRs was reported by Kaspi et al. (2003) in AXPs. Such outbursts in both classes of sources re-inforce the magnetar hypothesis, since such transient events are predicted (e.g., Thompson & Duncan 1996) as the consequence of violent rearrangements of superstrong magnetic fields thredding the neutron star crust. This soft X-ray emission observed over the past two decades from AXPs and SGRs has been typically fitted by blackbody plus power-law components (e.g., Perna et al. 2001), leading to thermal component temperature estimates of the order of $\sim$0.5–1 keV, while the non-thermal tail component is usually steep. More recently, and surprisingly, pulsed hard X-ray (20–150 keV) tails have been detected by *INTEGRAL* along with *RXTE*, *XMM-Newton*, and *ASCA* data in several AXPs (Kuiper et al. 2004, 2006; den Hartog et al. 2008a, 2008b) and SGRs (Mereghetti et al. 2005; Molkov et al. 2005; Götz et al. 2006; see also Rea et al. 2009 for the new source SGR 0501+4516). The hard X-ray tails are characteristically flatter than the power-law tail in the soft X-ray band, except for SGR 1900+14 which is steeper. Their extension is, however, constrained by upper limits from the COMPTEL instrument on the *Compton Gamma-Ray Observatory*, which imply a spectral turnover around 200–500 keV (e.g., den Hartog et al. 2008a, 2008b), a feature whose existence is more or less reinforced by *Fermi*-LAT upper limits to magnetar emission above 100 MeV (Abdo et al. 2010).

In highly magnetized neutron stars, inverse magnetic Compton scattering of X-ray surface photons is expected to be highly efficient (e.g., Baring & Harding 2007) in generating the X-ray spectra if the real plasma density is super-Goldreich–Julian. There are various scenarios where such plasma densities are plausible in magnetars (e.g., Thompson et al. 2002 or Thompson & Beloborodov 2005). At the cyclotron resonance,

the cross section exceeds the Thomson cross section by two or more orders of magnitude (e.g., Daugherty & Harding 1986; Gonthier et al. 2000). Recently, the steep tail portions of the soft X-ray emission of magnetars has been fitted by a resonant Comptonization model with mildly relativistic electrons (Lyutikov & Gavriil 2006; Rea et al. 2008). The Lyutikov & Gavriil model uses a non-relativistic magnetic Thomson cross section, neglecting electron recoil, and the fits are of comparable accuracy to a canonical blackbody plus power-law prescription. Similar Comptonization analyses have been presented in Güver et al. 2007 and Güver et al. 2008, for the AXPs XTE J1810-197 and 4U 0142+61, respectively, using detailed X-ray spectroscopy to constrain the surface magnetic fields of these magnetars. Nobili et al. (2008a) have also successfully fitted the soft X-ray *XMM-Newton* spectra of AXP CXOUJ1647-4552 using a more sophisticated Monte Carlo resonant Comptonization model.

For the hard tail X-ray magnetar emission, repeated upscattering by hot, mildly relativistic electrons (i.e., Comptonization) may have difficulties in modeling the observed flat spectra due to the relatively high efficiency of photon escape from the interaction region. In contrast, single resonant Compton upscatterings by electrons with ultrarelativistic Lorentz factors $\gamma_e \gg 1$ is potentially a more viable mechanism, provided that such a source of electrons exists in a scattering locale close to the hot photon bath on the surface. Previous work on magnetic inverse Compton scattering, when applied to pulsar magnetospheres (Daugherty & Harding 1989), and also in the context of neutron star models of gamma-ray bursts (e.g., Dermer 1990), computed upscattering spectra and electron cooling rates and in the non-relativistic magnetic Thomson limit (extended from non-magnetic Comptonization in Ho & Epstein 1989). These magnetic Thomson models serve as a crucial check in the non-relativistic or weak field limits of any fully relativistic QED formalism. Sturner (1995) further extended Dermer (1990) and presented more sophisticated cooling rate calculations with consideration of thermal seed photons as well as Klein–Nishina corrections. These analyses are not necessarily sufficient for magnetars' hard X-rays in the relativistic quantum domain, where both fields in excess of the quantum critical value $B_{cr} \approx 4.413 \times 10^{13}$ G, and ultrarelativistic Lorentz factors for electrons, may be realized. Baring & Harding (2007) and Nobili et al. (2008b) have presented some basic analyses in this ultrarelativistic QED domain and find substantive differences relative to results from magnetic Thomson cases. Ultimately, the maximum electron energy and emission spectral characteristics may be well controlled by the cooling rate, so that accurate computation of such rates is essential for complete models of inverse Compton spectral formation. Hence, extending such resonant Compton cooling analyses to treat the relativistic, quantum domain is imperative.

Fully relativistic QED magnetic cross sections in the spin-averaged Johnson & Lippmann (1949, hereafter JL) wave function formalism are found in Herold (1979), Daugherty & Harding (1986), and Bussard et al. (1986), extending earlier non-relativistic quantum mechanical formulations such as Canuto et al. (1971). These have been the tool of choice for resonant Compton scattering implementations in neutron star studies. Yet, in the cyclotron resonance, the *spin-dependent* widths depend on the choice of electron wave functions in a uniform magnetic field, and therefore so also do the Compton cross sections and scattering rates. The JL wave functions are Cartesian coordinate eigenstates of the kinetic momentum operator. The Sokolov & Ternov (1968, hereafter ST) "transverse polarization" states constitute a popular alternative and are eigenfunctions of the

magnetic moment operator that are derived in cylindrical coordinates. The ST states possess important symmetries between electron and positron states (e.g., Herold et al. 1982; Melrose & Parle 1983), and under Lorentz transformations along the magnetic field (Baring et al. 2005). Moreover, Graziani (1993) contended that the ST wave functions are the physically correct choices for incorporating spin-dependent widths in the resonance of the QED scattering cross section, since they diagonalize both the magnetic moment and mass operators. Here, cooling rates are computed for both sets of states, namely, spin-averaged JL scatterings and spin-dependent ST calculations, highlighting significant differences between the two when the cyclotron resonance is sampled. The two wave function choices generate identical Compton cooling rates when the scatterings are non-resonant. This is the first time that ST QED formalism has been deployed in the computation of magnetic Compton rates for the cooling of relativistic electrons. Since the magnetar atmospheric thermal photon energies are much less than the electron rest mass, it is appropriate to specialize to scatterings that leave the electron in the zeroth Landau level, as noted in Gonthier et al. (2000) and adopted by Baring & Harding (2007); this expedient simplification is employed here.

The principal thrust of this paper is to serve as a foundation for the explanation of hard X-ray spectra of magnetars, to enable refinements of the resonant upscattering model of Baring & Harding (2007) that incorporate evolution of the electron distribution due to Compton cooling. It presents, for the first time, numerical calculations of the electron cooling rates, and associated analytical approximations, for magnetic Compton upscattering in the fully relativistic quantum regime. The analysis forms collision integrals for these rates by weighting the scattering cross section. The principal assumption employed is the restriction to ultrarelativistic electrons moving along **B**, an approximation that is generally highly accurate for resonant interactions in high-field pulsars and magnetars. These rates will provide important input for future kinetic equation analyses and Monte Carlo simulations of time-dependent evolution of cooling electron distributions and concomitant Compton upscattering spectra. Relativistic reductions profoundly change the rates; classic inverse Thomson $\dot{\gamma}_e \propto \gamma_e^2$ cooling is not realized in the ultrarelativistic regime since the cross section is well below the Thomson value. The work evaluates rates for both monoenergetic soft photons and thermal surface X-rays; the latter case profoundly alters the kinematic accessibility of the resonance, yielding $\dot{\gamma}_e \propto \gamma_e^{-1}$ regimes extending to extremely high Lorentz factors. The cooling rate calculation also encapsulates arbitrary interaction altitudes and colatitudes in neutron star magnetospheres, via a generalized angular distribution function, under the simplifying assumption of photons emitted isotropically and uniformly over the entire stellar surface. This restriction facilitates greater tractability of the analysis and will be relaxed in future work that accounts for the influence of surface inhomogeneities and anisotropies (e.g., Zavlin et al. 1995; Thompson & Beloborodov 2005). The cooling rate formalism is expounded upon in Section 2, specialized results for Thomson regimes and uniform soft photon fields are discussed in Section 3, before the more general QED cooling calculations for arbitrary locales in the magnetosphere are addressed in Sections 4 and 5. We derive compact analytic asymptotic approximations to resonance cooling rates that verify the numerics. In addition, we observe that the Lorentz factors for the onset of resonant cooling rates are controlled by simple kinematic constraints that depend on the surface temperature and the value of the field strength in the interaction zone.

2. RESONANT SCATTERING COOLING RATE FORMALISM

The focus here is specifically for the case of photons initially propagating along the magnetic field lines. Such a restriction is strongly motivated in gamma-ray pulsar models, since photons engaged in Compton scattering generally collide with ultrarelativistic electrons moving in the magnetosphere. Virtually all magnetospheric pulsar models, both of the polar cap or outer gap varieties, inject electrons with Lorentz factors $\gamma_e \sim 10^4$–10^7. This is effectively mandated by the observation of hard gamma rays in the EGRET and *Fermi* pulsars (see the *Fermi*-LAT Pulsar Catalog; Abdo et al. 2010 for a good synopsis of the status quo). Yet the ensuing cascades generally fail to cool the electrons down to mildly relativistic energies so that the $\gamma_e \gg 1$ assumption holds (Daugherty & Harding 1982; Zhang & Harding, 2000; Hibschman & Arons 2001; Rudak et al. 2002; Sturner 1995; Dyks & Rudak 2000; Harding & Muslimov 2002). In cascade development, the components of the electron momenta perpendicular to **B** are rapidly degraded due to extremely rapid cyclotron/synchrotron cooling, typically in timescales of 10^{-20} to 10^{-16} s. Hence, the assumption that soft X-ray photons scatter off electrons that move ultrarelativistically along the field is generally a secure one, probably extendable to the magnetar regime. This $\gamma_e \gg 1$ restriction will be adopted here, with cases of cooling at mildly relativistic energies being deferred to future work. For such ultrarelativistic electrons, Lorentz transformation to the electron rest frame (ERF) then results in photon propagation along **B**, regardless of the direction of a low energy photon in the magnetospheric frame. This then spawns great simplification of the relativistic differential cross section for JL wave functions from the fully general form presented in Daugherty & Harding (1986), as outlined in Gonthier et al. (2000). A similar simplification is afforded for ST formulations of the cross section (P. L. Gonthier et al. 2011, in preparation). The compact expressions for these two differential cross sections in the case of photon propagation parallel to **B** are presented in Equations (13) and (15) below.

2.1. Upscattering Kinematics

To set the scene for the exposition on collision integral calculations of electron cooling rates, it is necessary to first summarize key kinematic aspects. Both the Lorentz transformation from the observer's or laboratory frame (OF) to the ERF and the scattering kinematics in the ERF are central to determining the character of resonant Compton upscattering spectra and the cooling rates. As choices of photon angles in these two reference frames are not unique, the conventions adopted here are now stated; they follow those used in Baring & Harding (2007). Let the electron velocity vector in the OF be $\vec{\beta}_e$, which is parallel to **B** due to rampant cyclo-synchrotron cooling perpendicular to the field. The dimensionless pre- and post-scattering photon energies (i.e., scaled by $m_e c^2$) in the OF are ε_i and ε_f, respectively, and the corresponding angles of these photons with respect to $-\vec{\beta}_e$ (i.e., field direction) are Θ_i and Θ_f, respectively. With this definition,

$$\mu_{i,f} \equiv \cos\Theta_{i,f} = -\frac{\vec{\beta}_e \cdot \vec{k}_{i,f}}{|\vec{\beta}_e| \cdot |\vec{k}_{i,f}|}, \tag{1}$$

and *the zero angles are chosen anti-parallel to the electron velocity*, corresponding to head-on collisions. Here, $\vec{k}_i$ and $\vec{k}_f$ are the initial and final photon three momenta in the OF, and

the μs denote photon angle cosines hereafter. Whether $\vec{\beta}_e$ is parallel to or anti-parallel to **B** is irrelevant to the scattering problem. Boosting by $\vec{\beta}_e$ to the ERF then yields pre- and post-scattering photon energies in the ERF of ω_i and ω_f, respectively, with corresponding angles with respect to $-\vec{\beta}_e$ of θ_i and θ_f. The relations governing this Lorentz transformation are

$$\omega_{i,f} = \gamma_e \varepsilon_{i,f}(1 + \beta_e \cos\Theta_{i,f}),$$
$$\cos\theta_{i,f} = \frac{\cos\Theta_{i,f} + \beta_e}{1 + \beta_e \cos\Theta_{i,f}}, \tag{2}$$

the kinematic picture of which is illustrated in Figure 1. The inverse transformation relations are obtained from these by the interchange $\theta_{i,f} \leftrightarrow \Theta_{i,f}$ and the substitutions $\omega_{i,f} \to \varepsilon_{i,f}$ and $\beta_e \to -\beta_e$. The form of Equation (2) clearly indicates that head-on collisions in the OF generate the largest values of ω_i and guarantees that for most Θ_i, the initial scattering angle θ_i in the ERF is close to zero when $\gamma_e \gg 1$. Exceptions to this general rule arise when $\cos\Theta_i \approx -\beta_e$, cases that form a small fraction of the upscattering phase space, and generally provide only a small contribution to the cooling rate for ultrarelativistic electrons. The dominance of $\theta_i \approx 0$ interactions motivates the particular laboratory frame angle convention adopted in Equation (1).

In the ERF, the scattering kinematics differ from that described by the familiar Compton formula in the absence of magnetic fields, since momentum conservation perpendicular to the field is not mandated. General forms for the relationship between ω_f and ω_i, θ_i and θ_f are posited, for example, in Herold (1979) and Daugherty & Harding (1986). In the special case $\theta_i \approx 0$ that is generally operable for the $\gamma_e \gg 1$ scenario here, the kinematic formula for the final photon energy ω_f in the ERF can be approximated by

$$\omega_f = \omega'(\omega_i, \theta_f) \equiv \frac{2\omega_i r}{1 + \sqrt{1 - 2\omega_i r^2 \sin^2\theta_f}},$$
$$r = \frac{1}{1 + \omega_i(1 - \cos\theta_f)}, \tag{3}$$

where r is the ratio ω_f/ω_i that would correspond to the non-magnetic Compton formula, which in fact does result if $\omega_i r^2 \sin^2\theta_f \ll 1$. Equation (3) is a rewriting of Equation (15) of Gonthier et al. (2000; see also Equation (9) of Baring & Harding 2007) and can be simply rearranged into the following convenient form:

$$(\omega_f)^2 \sin^2\theta_f - 2\omega_i\omega_f(1 - \cos\theta_f) + 2(\omega_i - \omega_f) = 0. \tag{4}$$

These kinematic forms are realized for the particular case where electrons remain in the ground state (zeroth Landau level) after scattering. Such forms are relevant for common astrophysical situations that sample near and below the cyclotron resonance, though well above the resonance, cases of electron excitation must be entertained (see Gonthier et al. 2000). Unless otherwise stated, hereafter it will be assumed that scattered electrons will be produced in the lowest Landau levels (i.e., spin-down to spin-down transitions), and the kinematics described above applies to any spin-state formalism for the collision cross section.

2.2. General Cooling Rate Formalism

To ascertain representative electron cooling rates in pulsar and magnetar magnetospheres, collision integral calculations of these rates are performed. For the purposes of this paper, the
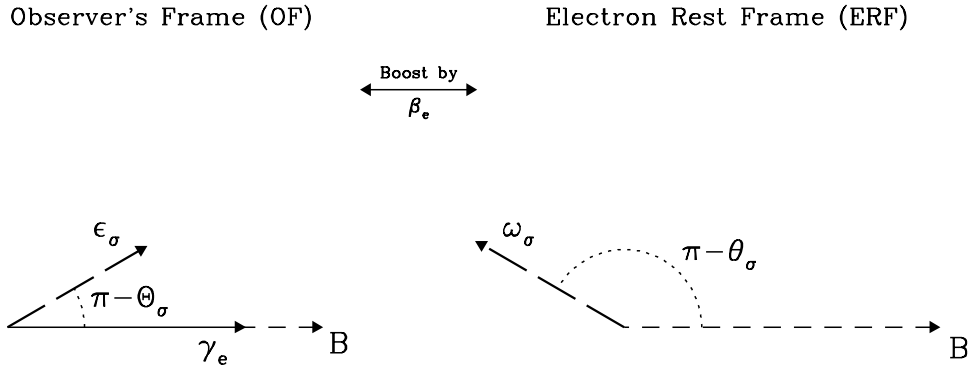
Figure 1. Photon momenta and the kinematic geometry for boosts between the observer's or laboratory frame of the pulsar and the electron rest frame, in which the scattering cross section is most simply expressed. The boost is along the local magnetic field vector since the electrons occupy the lowest Landau level. The label $\sigma = i, f$ represents either the initial (i, incoming) or final (f, scattered) photon. The kinematic relationships between photon energies and angles in the two frames of reference are expressed in Equation (2).

electrons will be assumed to be monoenergetic, with Lorentz factor γ_e and number density n_e, i.e., their distribution function is $n_e \delta(\gamma - \gamma_e)$. To simplify the formalism for the cooling rates, monoenergetic, incident photons of dimensionless energy $\varepsilon_\gamma = \varepsilon_s$ will first be assumed, with the implicit understanding that $\varepsilon_s \sim 3kT/m_e c^2$ forges the connection with surface X-ray temperatures. Clearly values of $\varepsilon_s \sim 3 \times 10^{-4}$–$3 \times 10^{-3}$ are commensurate with thermal photon temperatures $kT \sim$ 0.1–0.3 keV observed in or inferred for middle-aged pulsars (see Becker & Trümper 1997 for a comprehensive exposition on X-ray pulsar emission) and also radio-quiet, long-period-isolated neutron stars (e.g., Haberl 2007), and hotter surface environs ($kT \sim 0.5$–1 keV) in the more highly magnetized AXPs (see Perna et al. 2001). Subsequently, the soft photon energies ε_s will be distributed via a Planck spectrum. This more precise approach provides more than just a smearing out of sharp cooling function features exhibited in the various figures below that pertain to monoenergetic soft photons; it provides an extension of the kinematically accessible phase space for resonant interactions. It will become clear that this extension is a profound inclusion, defining the character of the cooling rates at high Lorentz factors.

The possibility of soft photon anisotropy will be retained in the formalism. This is appropriate for moderate and high altitude locales for scattering interactions, where remoteness from points of origin on the stellar surface incurs stronger anisotropies in the target X-ray population. Accordingly, in the analysis in Sections 3 and 4.1, the soft photon number density distribution will take the form

$$n_\gamma(\varepsilon_i, \mu_i) = n_s \frac{f(\mu_i)}{\mu_+ - \mu_-} \delta(\varepsilon_i - \varepsilon_s)$$

$$\text{for} \quad \int_{\mu_-}^{\mu_+} \frac{f(\mu)\,d\mu}{\mu_+ - \mu_-} = 1 \qquad (5)$$

prescribing the normalization of the angular portion, which is separable from the energy dependence. Observe that the azimuthal dependence is integrated over in forming $f(\mu_i)$, a step that can be taken from the outset since the Compton differential cross section does not depend on such azimuthal angles; this is true regardless of the interaction locality. Details of how azimuthal dependence is subsumed in $f(\mu_i)$ are expounded in Section 5, forging a direct connection to the magnetospheric interaction geometry that is encapsulated in Equation (71). To simplify earlier parts of our analysis, we will first assume photon isotropy within a cone (or hemisphere), which amounts to setting

$f(\mu_i) \to 1$, i.e., a uniform distribution of angle cosines μ_i in some range $\mu_- \leqslant \mu_i \leqslant \mu_+$. This is often broad enough to encompass the resonance, i.e., the value $\mu_i = [B/(\gamma_e \varepsilon_s) - 1]/\beta_e$, but not always so, as will become evident in due course. In Sections 4.2, 4.3, and 5 an alternative normalization protocol will be adopted, being germane to thermal soft X-ray photon anisotropies at and above the surface.

The formulation for upscattering spectra appropriate to the resonant Compton problem was presented in Baring & Harding (2007). This made use of generic Compton upscattering formalism presented in Equations (A7)–(A9) of Ho & Epstein (1989) that is applicable to both Thomson and Klein–Nishina regimes, and moreover is readily adaptable to incorporate magnetic kinematics and the QED cross section for fully relativistic cases of magnetic Compton scattering. The spectrum of photon production $dn_\gamma/(dt\, d\varepsilon_f\, d\mu_f)$, differential in the photon's post-scattering laboratory frame quantities ε_f and $\mu_f = \cos\Theta_f$, can be written as

$$\frac{dn_\gamma}{dt\, d\varepsilon_f} = \frac{n_e n_s\, c}{\mu_+ - \mu_-}$$
$$\times \int_{\mu_l}^{\mu_u} d\mu_f \int_{\mu_-}^{\mu_+} d\mu_i\, f(\mu_i)\, \delta[\omega_f - \omega'(\omega_i, \theta_f)]$$
$$\times \frac{1 + \beta_e \mu_i}{\gamma_e(1 + \beta_e \mu_f)} \frac{d\sigma}{d(\cos\theta_f)}. \qquad (6)$$

Observe that in deriving this, the angle convention specified in Equation (1) requires the substitution $\beta_e \to -\beta_e$ in Equations (A7)–(A9) of Ho & Epstein (1989). Here, the notation $\mu_i = \cos\Theta_i$ and $\mu_f = \cos\Theta_f$ is used for compactness. In Equation (6), the factor $c(1 + \beta_e \mu_i)$ expresses the relative velocity in photon–electron collisions, remembering that $\mu_i = 1$ represents head-on impacts. Also, the $\gamma_e(1 + \beta_e \mu_f)$ factor in the denominator arises because of the Lorentz transformation of the differential cross section between the ERF and the OF. The rate can then be routinely weighted by the factor $-(\varepsilon_f - \varepsilon_i)/n_e \approx -\varepsilon_f/n_e$ when $\gamma_e \gg 1$, and integrated over all produced energies ε_f, to generate the required electron cooling rate:

$$\dot\gamma_e = -\frac{n_s\, c}{\mu_+ - \mu_-}$$
$$\times \int \varepsilon_f\, d\varepsilon_f \int_{\mu_l}^{\mu_u} d\mu_f \int_{\mu_-}^{\mu_+} d\mu_i\, f(\mu_i)\, \delta[\omega_f - \omega'(\omega_i, \theta_f)]$$
$$\times \frac{1 + \beta_e \mu_i}{\gamma_e(1 + \beta_e \mu_f)} \frac{d\sigma}{d(\cos\theta_f)}. \qquad (7)$$

Hereafter the specializations $\mu_l \to -1$ and $\mu_u \to 1$ are adopted to encompass the full cooling parameter space. Explicit presentation of the limits on the ε_f integration is suppressed for the moment, since these are somewhat complicated with this choice of variables.

It is more convenient to change the angular integration variables $\mu_{i,f}$ at this juncture to ω_i and ω_f, for which the Jacobian indentity for this transformation is $d\mu_i \, d\mu_f = d\omega_i \, d\omega_f / (\gamma_e^2 \beta_e^2 \varepsilon_i \varepsilon_f)$. In addition, the substitution $(1 + \beta_e \mu_i)/(1 + \beta_e \mu_f) \to \omega_i \varepsilon_f / (\omega_f \varepsilon_i)$ can be employed. Then the ω_f integration is trivial, and the limits on the subsequent ω_i integration are simply obtained from Equation (2), namely, $\gamma_e(1 + \beta_e \mu_-)\varepsilon_s \leqslant \omega_i \leqslant \gamma_e(1 + \beta_e \mu_+)\varepsilon_s$. The limits on the ε_f integration are less easily derived, since they are formed from the combination of the Lorentz transformation characteristics in Equation (2) and the Compton scattering kinematic constraint on ω_f in Equation (3), in concert with the domain $|\cos\theta_f| \leqslant 1$. The resulting range is

$$\gamma_e(1 - \beta_e)\,\omega_i \leqslant \varepsilon_f \leqslant \frac{\gamma_e(1 + \beta_e)\,\omega_i}{1 + 2\omega_i}, \qquad (8)$$

for which the resonant $\omega_i = B$ specialization is offered in Equation (15) of Baring & Harding (2007). Since the bounds on ε_f are dependent on ω_i, it is expedient to reverse the order of the integrations. Then the final nuance in the manipulations is to change variables from ε_f to $\cos\theta_f$ via $\varepsilon_f = \gamma_e\omega_f(1 - \beta_e\cos\theta_f)$, motivated by the fact that the differential cross section for Compton scattering is expressed most compactly in terms of $\cos\theta_f$. Note that the range in Equation (8) corresponds to $-1 \leqslant \cos\theta_f \leqslant 1$. The culmination of these steps is the final general form for the cooling rate:

$$\dot{\gamma}_e = -\frac{n_s c}{\mu_+ - \mu_-} \, \frac{1}{\gamma_e^2 \beta_e^2 \varepsilon_s^2} \int_{\omega_-}^{\omega_+} \omega_i \, d\omega_i \int_{-1}^{1} d(\cos\theta_f)$$
$$\times \, [1 - \beta_e\cos\theta_f] \, f(\mu_i) \left| \frac{\partial\varepsilon_f}{\partial(\cos\theta_f)} \right| \frac{d\sigma}{d(\cos\theta_f)} \quad (9)$$

for $\mu_i = [\omega_i/(\gamma_e\varepsilon_s) - 1]/\beta_e$, with

$$\omega_+ = \gamma_e(1 + \beta_e\mu_+)\varepsilon_s, \qquad \omega_- = \gamma_e(1 + \beta_e\mu_-)\varepsilon_s. \quad (10)$$

This double integral form provides the basis for the subsequent calculations in this paper. It is understood that ω_f is given by Equation (3). The computational convenience of this result is underlined by the fact that the integration variables are now those embodied in the differential cross section $d\sigma/d(\cos\theta_f)$. Using $\varepsilon_f = \gamma_e\omega_f(1 - \beta_e\cos\theta_f)$ and Equation (4), it can be established that

$$\frac{\partial\varepsilon_f}{\partial(\cos\theta_f)} = \gamma_e(1 - \beta_e\cos\theta_f)\frac{\partial\omega_f}{\partial(\cos\theta_f)} - \gamma_e\beta_e\omega_f \quad (11)$$

for

$$\frac{\partial\omega_f}{\partial(\cos\theta_f)} = \frac{\omega_f^2\,(\omega_i - \omega_f\cos\theta_f)}{2\omega_i - \omega_f[1 + \omega_i(1 - \cos\theta_f)]}. \quad (12)$$

In the Thomson limit where $\omega_f \approx \omega_i \ll 1$, the $\partial\omega_f/\partial(\cos\theta_f)$ term contributes insignificantly to Equation (11) and the Jacobian satisfies $|\partial\varepsilon_f/\partial(\cos\theta_f)| = \gamma_e\beta_e\omega_f$. Finally, we remark that in the neighborhood of the resonance, further manipulation of Equation (9) is detailed in Section 4, so as to facilitate both numerical computations and the derivation of analytic asymptotics for the rates.

2.3. The Differential Cross Section

The last remaining ingredient in the formulation is the differential cross section $d\sigma/d(\cos\theta_f)$. Here, because the possibility of near-critical and supercritical fields is entertained, it is necessary to generalize beyond the magnetic Thomson limit cross sections employed in the cooling calculations of Daugherty & Harding (1989), Sturner (1995), and Harding & Muslimov (1998). Fully relativistic, quantum cross-section formalism for the Compton interaction in magnetic fields can be found in Herold (1979), Daugherty & Harding (1986), and Bussard et al. (1986). These were obtained using the old Johnson & Lippmann (1949) eigenfunctions of the Dirac equation in a uniform magnetic field. These traditional wave functions are Cartesian coordinate eigenstates of the kinetic momentum operator that do not diagonalize the magnetic moment operator. They are conveniently used in cases where information on the spin of the intermediate electron states is not germane and can be averaged over; such is the case for scattering calculations well removed from the cyclotron resonance. The cross section for the alternative Sokolov & Ternov (1968) states is also discussed below, since we employ it as an upgrade over previous treatments of scattering; this development will also incorporate full spin dependence of the cross section near the cyclotron resonance, a desirable advance.

For our $\gamma_e \gg 1$ focus here, where the incoming photons in the ERF move along the field lines, Gonthier et al. (2000) obtained algebraic simplification of the results of Daugherty & Harding (1986). Here, we use Equation (23) of Gonthier et al. (2000), a more compact form of which is presented in Baring & Harding (2007). These forms are specialized to the case of scatterings that leave the electron in the ground state, the zeroth Landau level that it originates from. This expedient choice is appropriate at and below the cyclotron resonance where ground-state-to-ground-state transitions provide the only contribution to the cross section, but must be relaxed well above the resonance where excitations tend to dominate. As will become apparent below, when blackbody soft photon distributions are adopted, the resonant contribution always overwhelms that above resonance (and below the first harmonic) when kinematics render both regimes accessible. Moreover, astrophysical applications of these cooling rates will most likely be employed in contexts where the cooling competitively limits some electron acceleration process so that harmonics of the cyclotron fundamental are not often encountered in neutron star model applications involving hard X-rays. Hence, there is not strong motivation for addressing excitation transitions: they are expected to introduce only small corrections to the results presented here because they possess cross sections near the resonant cyclotron harmonics that are generally much smaller than that in the neighborhood of the fundamental (e.g., see Daugherty & Harding 1986). Moreover, the decay width is larger in the harmonics than in the fundamental (e.g., see Equation (19) of Herold et al. 1982, for trends with harmonic number n in $B \ll 1$ cases, and Figure 3 of Harding & Lai 2006, for an illustration that $\partial\Gamma/\partial n > 0$ in all field regimes), thereby reducing the effective cross section at the peak of the resonance. Such excitation refinements will be deferred to future work.

For the computation of electron cooling rates, it is necessary to sum over final photon polarizations and also to introduce the effective (electron spin-averaged) width Γ associated with the cyclotron decay lifetime for the intermediate electron states. Adapting Equations (12) and (13) of Baring & Harding (2007), the differential Compton cross section in the JL formalism to be

used here takes the form

$$\frac{d\sigma_{\rm JL}}{d(\cos\theta_f)} = \frac{3\sigma_{\rm T}}{16}\frac{(\omega_f)^4\ \mathcal{T}\ \exp\{-\kappa\}}{\omega_i\ [2\omega_i - \omega_f - \zeta\ ]}$$
$$\times \left\{\frac{1}{(\omega_i - B)^2 + (\Gamma/2)^2} + \frac{1}{(\omega_i + B - \zeta)^2}\right\}$$
(13)

for $\kappa = \omega_f^2 \sin^2\theta_f/[2B]$ and $\zeta = \omega_i\omega_f(1 - \cos\theta_f)$. The polarization-averaged factor in the numerator is

$$\mathcal{T} = 1 + \cos^2\theta_f + \omega_i(1 - \cos\theta_f)^2 - \omega_f \sin^2\theta_f,$$
$$\Rightarrow \omega_f\mathcal{T} = 2\omega_i - (1 + \omega_i)\,\omega_f(1 - \cos^2\theta_f),$$
$$\Rightarrow \omega_f^2\mathcal{T} = 2(\omega_i - \omega_f) - 2\omega_i\omega_f(1 + \omega_i)\{1 - \cos\theta_f\} + 2\omega_i^2,$$
(14)

where the kinematic result in Equation (4) has been used in deriving these identities. Note that for magnetic Compton scattering, in this particular case of photons propagating along **B** prior to scattering (i.e., $\theta_i = 0$), the differential cross sections are independent of the initial polarization of the photon (Gonthier et al. 2000). This property is a consequence of circular polarizations forming the natural basis states for $\theta_i = 0$ and guarantees that the electron cooling rates computed in this paper are insensitive to the initial polarization level (zero or otherwise) of the soft photons. Note also that the width Γ should also appear explicitly in the denominator of the second term inside the parentheses of Equation (13), however, since its contribution to this term is almost negligible for all field strengths, it is omitted for simplicity. In addition, only the cyclotron fundamental appears as a resonance, corresponding to an intermediate virtual electron state in the first ($n = 1$) Landau level.

In this paper, the Sokolov & Ternov (1968) transverse polarization eigenstate formulation of the magnetic Compton cross section is also used. Deployment of the JL cross section, while historically convenient, is unsatisfactory in the cyclotron resonance on physical grounds. Since the JL states do not diagonalize the spin operator, they do not yield correct spin-dependent cross sections. Outside the $\omega_i \approx B$ resonance this is irrelevant, since the spin quantum numbers of the intermediate electrons are summed, and differential cross sections are necessarily independent of eigenfunction choices for the intermediate states. However, in the cyclotron resonance, the lifetime of the intermediate electron state is spin dependent so that sums over electron propagator spin states no longer generate simple averages, yielding a feedback between the value of the cross section and the choice of basis states. The ST wave functions are preferred as solutions of the magnetic Dirac equation. Baring et al. (2005) highlighted this by demonstrating that Lorentz transformations along **B** mix the spin states when JL eigenfunctions are employed as a basis, while ST states transform unmixed, thereby providing the inherently attractive simplicity of Lorentz invariance. Moreover, they exhibit symmetry between positron and electron states. Graziani (1993) observed that they are the physically correct choices for spin-dependent treatments and for incorporating widths in the scattering cross section.

A full treatment of the ST state formulation for Compton scattering in strong magnetic fields was presented in Sina (1996) and has been honed analytically and numerically by P. L. Gonthier et al. (2011, in preparation), for the case of

photons incident along the magnetic field lines. Away from the fundamental resonance, the differential cross section matches that of the JL formalism in Equation (13), as it should. In the resonance, both near the peak and in the wings, specifically in the range $0.95 < \omega_i/B < 1.05$, P. L. Gonthier et al. (2011, in preparation) demonstrate that the ST differential cross section can be approximated by the compact analytic spin-dependent form

$$\frac{d\sigma_{\rm ST}}{d(\cos\theta_f)} = \frac{3\sigma_{\rm T}}{64}\frac{\omega_f^2\ e^{-\kappa}}{\omega_i\ [2\omega_i - \omega_f - \zeta\ ]\varepsilon_\perp^3}$$
$$\times \sum_{s=\pm 1}\frac{(\varepsilon_\perp - s)^2\,\Lambda_s}{(\omega_i - B)^2 + (\Gamma_s/2)^2},$$
(15)

for

$$\Lambda_s = (2\varepsilon_\perp + s)\{\omega_f^2\mathcal{T} - [\omega_i - \omega_f]\} - s\,\varepsilon_\perp^2\,[\omega_i - \omega_f].\quad (16)$$

Here, the quantum number s labels the intermediate electron's spin state (either spin up and down), yielding the two Lorentz profiles, which are described by the widths

$$\Gamma_s = \left(1 - \frac{s}{\varepsilon_\perp}\right)\Gamma,\quad \varepsilon_\perp = \sqrt{1 + 2B}\quad (17)$$

that emerge from the ST formulation of cyclotron decay rates from the first Landau level (see Baring et al. 2005, including Equation (1) therein, for details). Here, Γ is the same spin-averaged effective cyclotron width/decay rate as is used in the JL formulation, namely, that in Equation (22) below. Note that Equation (15) is an approximation *deployed only in the resonance* and is generally accurate to better than 0.4% whenever $0.95 < \omega_i/B < 1.05$, for a wide range of fields B: see Figure 11 in Appendix A.2. It contains no non-resonant term (which has been eliminated for simplicity) like the one appearing in Equation (13) that is generated by the second Feynman diagram (see Gonthier et al. 2000) for the scattering process. It is therefore used as a *patch* over the interval $0.95 < \omega_i/B < 1.05$, with Equation (13) being used for all other values of ω_i/B, since it represents the spin-averaged differential cross section appropriate to any eigenstate basis. A brief discussion of the derivation of Equation (15) from the starting point of Equation (3.25) in Sina (1996) is offered in Appendix A.2. Noting the identity

$$\frac{1}{\varepsilon_\perp^3}\sum_{s=\pm 1}(\varepsilon_\perp - s)^2\,\Lambda_s = 4\,\omega_f^2\mathcal{T},\quad (18)$$

it becomes clear that the discontinuity in mapping over from the ST patch in Equation (15) to the spin-averaged JL differential cross section in Equation (13) should be small in the wings of the resonance; numerically, for $0.01 < B < 10^2$ it is found to be smaller than 1% at $|\omega_i/B - 1| = 0.05$. The influence of this discontinuity is negligible on the ST rate calculations, being dominated by the contribution from much nearer the peak of the resonance at $\omega_i = B$.

The effective width Γ does not appear explicitly in the cross-section evaluations of Herold (1979), Daugherty & Harding (1986), Bussard et al. (1986), and Gonthier et al. (2000). It must be incorporated in order to account for the fact that the intermediate electron states effectively have a finite lifetime $1/\Gamma_{\rm cyc}$ to cyclotron decay that should formally be embedded in the resonant denominators that appear in the matrix elements for the Compton interaction. Normally this modification is omitted from papers focusing on cross-section calculations.

Yet its inclusion is necessary in spectral and rate computations since they sample convolutions of the entire resonance that are integrably divergent without the presence of natural widths to truncate the cyclotron resonance, thereby generating Lorentz line profiles. Comprehensive discussions of the incorporation of such widths in QED scattering formalism via a Breit–Wigner prescription are provided by Harding & Daugherty (1991), and later Graziani (1993) with an extensive formal exposition. Subtleties appear there in relativistic regimes (i.e., $B \gtrsim 1$) that mandate an update of the *ansatz* $\Gamma \to \Gamma_{\mathrm{cyc}}(p_z = 0)$ that was adopted by Baring & Harding (2007) and is predicated on common precedent for use in non-relativistic Thomson regimes (e.g., see Xia et al. 1985; Daugherty & Harding 1989; Dermer 1990; Baring 1994; Liu et al. 2006). Harding & Daugherty (1991; see their Equation (19)) observed that when incorporating the cyclotron decay width formally in the denominators, an extra factor of $\mathcal{E}_n = \sqrt{1 + 2nB + p_z^2}$ appears when the matrix elements are squared. The upgraded *ansatz* then becomes $\Gamma \to \mathcal{E}_n \Gamma_{\mathrm{cyc}}(p_z)$. Here, $n = 1$ is the quantum number of the intermediate state for the fundamental cyclotron resonance. The non-zero value of p_z that must be inserted in both $\mathcal{E}_1$ and $\Gamma_{\mathrm{cyc}}(p_z)$ is that obtained by parallel momentum conservation in the cyclotron interaction when the electron in the ERF absorbs the incoming photon propagating along **B**, namely, $p_z = \omega_i \approx B$ for our case of $\theta_i = 0$. Therefore, in the resonance $\mathcal{E}_1 \to 1 + B$.

Values for the width Γ that is needed for the spin-averaged JL calculation, and the spin-dependent ST formulation, can be inferred from the cyclotron decay analysis of Baring et al. (2005; see also Latal 1986; Pavlov et al. 1991; Harding & Lai 2006). The average rates for $1 \to 0$ transitions at non-zero p_z can be found in their Equations (13) or (23) and are scaled (by $\hbar/m_e c^2$) into dimensionless form here:

$$\Gamma_{\mathrm{cyc}}(p_z) = \overline{\Gamma}_{1 \to 0}(p_z) = \frac{\alpha_{\mathrm{f}} B}{\mathcal{E}_1} \, I_1(B), \quad \mathcal{E}_1 = \sqrt{1 + 2B + p_z^2}, \tag{19}$$

with

$$I_1(B) = \int_0^{\Phi} \frac{d\phi \, e^{-\phi}}{\sqrt{(\Phi - \phi)(1/\Phi - \phi)}} \left[1 - \frac{\phi}{2} \left(\Phi + \frac{1}{\Phi} \right) \right],$$
$$\Phi = \frac{\sqrt{1 + 2B} - 1}{\sqrt{1 + 2B} + 1} \tag{20}$$

expressing the integration over the angles of radiated cyclotron photons. Observe that right at the peak of the cyclotron resonance, $\omega_i = B$, the parameter Φ is just that identified in the scattering analysis in Appendix A, and the integration variable ϕ is effectively $\omega_f^2 \sin^2 \theta_f / (2B)$, i.e., the final angle variable employed in the analytic developments pertaining to resonant scattering. The integral for $I_1(B)$ can alternatively be expressed as an infinite series,

$$I_1(B) = \sum_{k=0}^{\infty} \frac{(-1)^k}{k!} \left\{ Q_k \left(1 + \frac{1}{B} \right) - \left(1 + \frac{1}{B} \right) Q_{k+1} \left(1 + \frac{1}{B} \right) \right\}, \tag{21}$$

where the $Q_\nu(z)$ are Legendre functions of the second kind. These special functions are finite sums of elementary logarithmic and polynomial functions of z (e.g., see Abramowitz & Stegun 1965). Properties of these functions that are germane to their numerical evaluation are supplied in the Appendix of Baring et al. (2005). The presence of the $\mathcal{E}_1$ factor in Equation (19) essentially accounts for time dilation when

boosting along **B** from the electron rest ($p_z = 0$) frame; the Lorentz factor for this boost is simply $\gamma = \mathcal{E}_1 / \sqrt{1 + 2B}$. The net *ansatz* is that the effective width Γ to be inserted into Equations (13) and (17) can be expressed as

$$\Gamma = \mathcal{E}_1 \Gamma_{\mathrm{cyc}}(p_z) \equiv \sqrt{1 + 2B} \, \Gamma_{\mathrm{cyc}}(p_z = 0) = \alpha_{\mathrm{f}} B \, I_1(B), \tag{22}$$

which is independent of $p_z = \omega_i$. When $B \ll 1$, this reduces to the commonly invoked form $\Gamma \approx 2\alpha_{\mathrm{f}} B^2/3$, which can be deduced using Equation (26) of Baring et al. (2005), or the $\Phi \ll 1$ limit of the integral in Equation (20). The enhancement of the width by the extra "relativistic" factor $\sqrt{1 + 2B}$ in supercritical fields is more than offset by the ultraquantum reductions in the cyclotron decay rate. The $\Phi \to 1$ limit of Equation (20) quickly reveals that $\Gamma \approx \alpha_{\mathrm{f}} B (1 - 1/e)$ when $B \gg 1$. Therefore, $\Gamma/B \ll 1$ always, regardless of the value of the field strength.

3. COOLING RATES IN THE MAGNETIC THOMSON REGIME

The exploration of resonant Compton cooling rates focuses first on the familiar magnetic Thomson regime, commonly treated in the pulsar literature, before addressing the new territory of the influences of a full QED treatment of the scattering process. This section will restrict considerations to monoenergetic soft photons that are uniformly distributed in angles within a conical sector of the sphere, so as to capture the essence of the magnetic Thomson cooling characteristics. Furthermore, only the JL cross section will be employed, for simplicity, though with a width choice that essentially maps over to the spin-dependent ST picture.

The Thomson regime is when $B \ll 1$ and $\omega_f \approx \omega_i \ll 1$, for which the JL differential cross section in Equation (13) simplifies to

$$\frac{d\sigma_{\mathrm{T}}}{d(\cos \theta_f)} \approx \frac{3\sigma_{\mathrm{T}}}{16} \left[1 + \cos^2 \theta_f \right] \Sigma_\kappa \left(\frac{\omega_i}{B} \right), \tag{23}$$

where the subscript T denotes here the magnetic Thomson domain, and

$$\Sigma_\kappa(\psi) = \frac{\psi^2}{(\psi - 1)^2 + \kappa^2} + \frac{\psi^2}{(\psi + 1)^2}, \quad \kappa = \frac{2\alpha_{\mathrm{f}} B}{3} \tag{24}$$

encapsulates both the resonant and non-resonant contributions to the cross section using ψ as the incoming photon energy scaled in terms of B. Here, σ_{T} is the field-free Thomson cross section. This form is commonly encountered in past neutron star radiative applications (e.g., see Dermer 1990; Baring 1994; Liu et al. 2006). The parameter $\kappa = \Gamma_{\mathrm{cyc}}/(2B)$ is a scaling of the non-relativistic natural line width $\Gamma_{\mathrm{cyc}} = 4\alpha_{\mathrm{f}} B^2/3$ of the cyclotron harmonic, the only resonance that appears in the Thomson limit. However, observe that this choice is precisely twice the $B \to 0$ limit of the spin-averaged width of the JL cross section encapsulated in Equation (19). The reason for this choice stems from the fact that in this $B \ll 1$ domain, the cyclotron rate is highly spin-asymmetric: spin-flip decays $n = 1 \to 0$ are profoundly inhibited so that only spin-down to spin-down transitions are probable (e.g., see Melrose & Zheleznyakov 1981; Herold et al. 1982). This no-spin-flip cyclotron transition has a rate given by $\Gamma_{\mathrm{cyc}} = 4\alpha_{\mathrm{f}} B^2/3$, exactly the classical rate (e.g., Bekefi 1966), so that the spin-averaged decay rate is exactly half of this, as outlined in Latal (1986) and
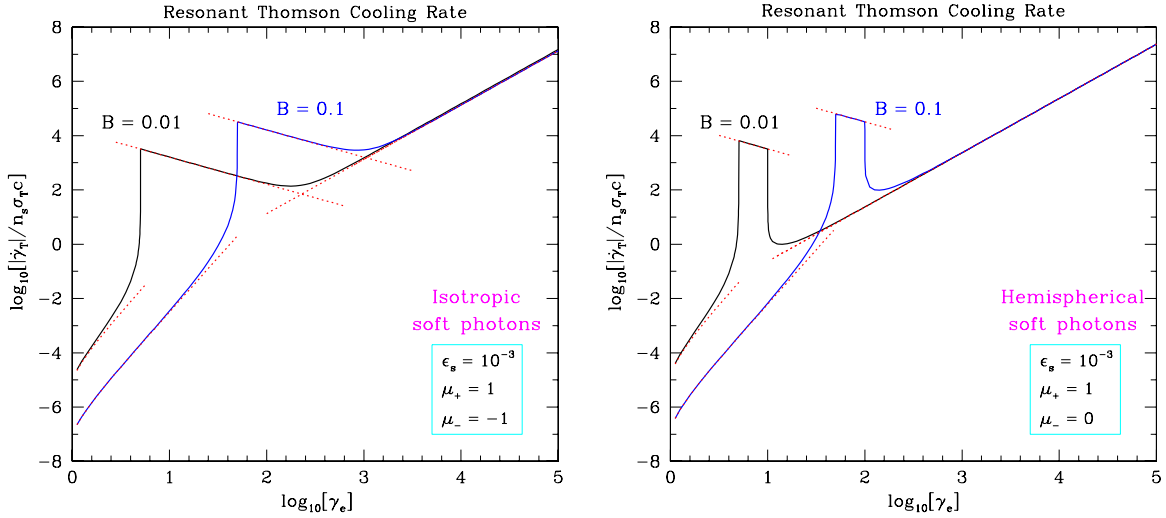
Figure 2. Resonant Thomson cooling rates for two different field strengths, as labeled, in units of $B_{cr} \approx 4.413 \times 10^{13}$ G, calculated using Equation (25), i.e., corresponding to the differential cross section in Equation (23). The soft photon energy distribution is monoenergetic, with $\varepsilon_s = 10^{-3}$, typical of that for neutron star surface X-rays. The two cases portrayed are isotropic soft photons (left panel) and hemispherical $n_s(\varepsilon_s)$ (right panel), the latter being fairly representative of interaction locations near the stellar surface. In both panels, the dotted lines encapsulate the asymptotic approximations embodied in Equations (30)–(32) (see the text). (A color version of this figure is available in the online journal.)

Baring et al. (2005). It is this higher, spin-biased width that has been adopted in the aforementioned astrophysical applications of magnetic Thomson scattering. This presumes that one spin state is prepared by successive, predominantly no-spin-flip cyclotron transitions from much higher states, a description that is satisfactory for semi-classical or non-relativistic quantum cyclotron problems. In the full, spin-dependent, ST cooling rate offering in Section 4 below, the scattering process itself biases the spin preparation of the intermediate state, and this nuance is taken into account self-consistently in this paper.

For a uniform conical beam of incident photons centered on an axis coincident with the local magnetic field vector, $f(\mu_i) = 1$ in the range $\mu_- \leqslant \mu_i \leqslant \mu_+$, and zero outside. The Thomson limit then reduces the Jacobian in Equation (9) to a simple form $|\partial \varepsilon_f / \partial (\cos \theta_f)| = \gamma_e \beta_e \omega_f \approx \gamma_e \beta_e \omega_i$, so that the cooling rate in Equation (9) becomes analytically tractable. The θ_f integration is almost trivial, and the resulting compact analytic form, valid for $\gamma_e \gg 1$, is

$$\dot{\gamma}_e = -\frac{n_s \sigma_T c}{2(\mu_+ - \mu_-)} \frac{B^3}{\gamma_e \beta_e \varepsilon_s^2} \left[\mathcal{I}_\kappa^2(\psi_+) - \mathcal{I}_\kappa^2(\psi_-) \right],$$

$$\psi_\pm = \frac{\omega_\pm}{B} = \frac{\gamma_e \varepsilon_s}{B}(1 + \beta_e \mu_\pm), \qquad (25)$$

where the pertinent integrals over ω_i lead to the definitions of the functions

$$\mathcal{I}_\kappa^p(\psi) = \int_1^\psi t^p \Sigma_\kappa(t) \, dt + c_p(\kappa). \qquad (26)$$

The constant terms $c_p(\kappa)$ are merely introduced to render the forms of the $\mathcal{I}_\kappa^p(\psi)$ more compact, and cancel out in all computations of $\dot{\gamma}_e$. The specific case of interest here is $p = 2$, for which

$$\mathcal{I}_\kappa^2(\psi) = \frac{2\psi^3}{3} + (6 - \kappa^2)\psi - \frac{1}{1+\psi} - 4\log_e(1+\psi)$$
$$+ 2(1 - \kappa^2) \log_e[(\psi - 1)^2 + \kappa^2]$$
$$+ \frac{1 - 6\kappa^2 + \kappa^4}{\kappa} \arctan\left(\frac{\psi - 1}{\kappa}\right), \qquad (27)$$

and

$$c_2(\kappa) \equiv \mathcal{I}_\kappa^2(1) = \frac{37}{6} - \kappa^2 + 4 \log_e \frac{\kappa}{2} - 4\kappa^2 \log_e \kappa. \qquad (28)$$

The combination of Equations (25) and (27) agrees algebraically with the leading order ($\gamma_e B \gg \varepsilon_s$) contribution for the resonant Thomson cooling rate in Equation (22) of Dermer (1990). Since $\kappa \ll 1$, the mathematical character of $\mathcal{I}_\kappa^2(\psi)$ is that of a step function smoothed on the scale of κ. Useful asymptotic forms for $\mathcal{I}_\kappa^2(\psi)$ are given by

$$\mathcal{I}_\kappa^2(\psi)$$
$$\approx \begin{cases} -\frac{\pi}{2\kappa}(1 - 6\kappa^2) - 1 + \frac{2}{5}\psi^5 + O(\psi^7) + O(\kappa^2), & \psi \ll 1, \\ \frac{\pi}{2\kappa}(1 - 6\kappa^2) + \frac{2\psi^3}{3} + O(\psi) + O(\kappa^2), & 1 \ll \psi. \end{cases}$$
$$(29)$$

Only these leading order terms are required for the results subsequently listed. Cooling rates computed using the magnetic Thomson limit in Equation (25) are displayed in Figure 2, for both isotropic ($\mu_\pm = \pm 1$) and hemispherical ($\mu_- = 0$, $\mu_+ = 1$) monoenergetic soft photon distributions. In both cases, the resonant contribution appears as a sharp "wall" signifying its onset at low γ_e, resolving into a slowly declining rate. The hemispherical case is for roughly head-on collisions between the soft photons and the relativistic electrons. In comparing the two panels of the figure, it becomes apparent that the removal of those soft photons that chase the electrons kinematically curtails the resonant "plateau" at higher Lorentz factors γ_e, so that this feature becomes narrower: its width is defined by the boundaries $\psi_\pm = 1$. Other asymptotic domains for the cooling rate are not qualitatively influenced by such soft photon collimation.

Various asymptotic cooling rates can now be obtained to establish correspondence with extant results in the literature and also to define the characteristics of general cooling rate numerics in uniform fields. The most familiar of these is the non-magnetic cooling rate, which is generally most salient for $B \ll 1$. In principal, for magnetic scattering events this domain

is realized when $1 \ll \psi_- \leqslant \psi_+$, i.e., $B/(\gamma_e \varepsilon_s) \ll 1 + \beta_e \mu_-$, for which the resonance is never sampled kinematically. In practice, this non-magnetic cooling situation often does not arise until γ_e is extremely large, or it may not arise at all. For example, if $\mu_- \approx -1$, corresponding to electrons and soft photons chasing each other along $\vec{B}$, then $1 + \beta_e \mu_- \approx 1/(2\gamma_e^2)$, so that $1 \ll \psi_-$ cases are not attained in highly magnetized systems that satisfy $B \gtrsim \varepsilon_s$. This occurrence could be common in high-field pulsars. However, a sufficient condition for the realization of a non-magnetic cooling rate is that the contribution of the resonance is dwarfed by non-resonant cooling. This arises when $\psi_- < 1 \ll \psi_+$, specifically when $\psi_+^3 \gg 3\pi/(4\kappa)$, and this domain is always accessible for the cross section in Equation (23), regardless of the value of μ_-. Then, the second form in Equation (29) readily yields the classical Thomson cooling rate

$$
\dot{\gamma}_e \approx \dot{\gamma}_{\mathrm{T}} = -n_s\,\sigma_{\mathrm{T}} c\, \gamma_e^2 \varepsilon_s\, \frac{(1 + \beta_e \mu_+)^3 - (1 + \beta_e \mu_-)^3}{3\beta_e\,(\mu_+ - \mu_-)},
$$
$$
\gamma_e \varepsilon_s (1 + \beta_e \mu_+) \gg \left(\frac{3\pi B^2}{8\alpha_{\mathrm{f}}} \right)^{1/3}. \tag{30}
$$

For isotropy with $\mu_+ = 1$ and $\mu_- = -1$, the β_e-dependent factor simply yields $4/3$ when $\gamma_e \gg 1$, and this rate then corresponds to the well-known classical form in Equation (7.16a) of Rybicki & Lightman (1979). It shall become apparent in Section 4 below that in strong fields, this regime will never be realized because Klein–Nishina reductions above the resonance will reduce the cross section below the Thomson scale, σ_{T}.

As the field is increased, or equivalently γ_e is reduced, the phase space for resonant interaction becomes larger, so that domains $\psi_- < 1 < \psi_+$ can be accessed. For these, the cooling rate is dominated by the contribution of the cyclotron resonance, and if $\psi_- \lesssim 1 \ll \psi_+$, with $\psi_+^3 \ll 3\pi/(4\kappa)$, then both the forms in Equation (29) are employed in arriving at the resonant Thomson cooling rate:

$$
\dot{\gamma}_e \approx \dot{\gamma}_{\mathrm{T,RES}} \equiv -\frac{3\pi}{4\alpha_{\mathrm{f}}}\, \frac{n_s\,\sigma_{\mathrm{T}} c}{\mu_+ - \mu_-}\, \frac{B^2}{\gamma_e \varepsilon_s^2},
$$
$$
B \ll \gamma_e \varepsilon_s (1 + \beta_e \mu_+) \ll \left(\frac{3\pi B^2}{8\alpha_{\mathrm{f}}} \right)^{1/3}. \tag{31}
$$

This is exactly equivalent to the $\gamma_e \gg 1$ limit of Equation (24) of Dermer (1990) in the specific case of monoenergetic soft photons. If the ratio $B/(\gamma_e \varepsilon_s)$ is increased further, the cooling again becomes non-resonant, but this time accessing an energy-dependent regime of the cross section, namely, $\sigma_{\mathrm{T}} \propto \omega_i^2$. This then introduces a stronger dependence on γ_e than in Equation (30), principally via the extra factor $(\omega_i/B)^2 \propto \gamma_e^2 \varepsilon_s^2/B^2$ that appears because $\psi_- \leqslant \psi_+ \ll 1$. Then

$$
\dot{\gamma}_e \approx -n_s\,\sigma_{\mathrm{T}} c\, \frac{\gamma_e^4 \varepsilon_s^3}{B^2}\, \frac{(1 + \beta_e \mu_+)^5 - (1 + \beta_e \mu_-)^5}{5\beta_e\,(\mu_+ - \mu_-)},
$$
$$
\gamma_e \varepsilon_s (1 + \beta_e \mu_+) \ll B. \tag{32}
$$

If $B \lesssim \varepsilon_s$, this third asymptotic regime is clearly never realized. Moreover, because it critically depends on ω_i^2 cross-section behavior for incident photons propagating along the field, relatively small incident photon angles θ_i in the ERF will modify it profoundly. When $\sin\theta_i \gtrsim \omega_i/B$, the scattering cross section below the resonance is approximately $\sigma_{\mathrm{T}} \sin^2\theta_i$ (for incoming photons of $\parallel$ polarization only; e.g., see Herold 1979), and since

$\theta_i \sim 1/\gamma_e$, at low Lorentz factors $\gamma_e \lesssim (B/\varepsilon_s)^{1/2}$ such non-zero ERF θ_i will cause the cooling rate to saturate at a finite value $\dot{\gamma}_e \sim -n_s \sigma_{\mathrm{T}} c\, \varepsilon_s$ (a suggestion of the onset of this appears in Figure 2 of Xia et al. 1985). In other words, the curves in Figure 2 will be modified for mildly relativistic electrons with $\gamma_e \lesssim 3$–5, when taking into account this finite ERF incidence angle θ_i effect. Finally, observe that as γ_e decreases from very high values, these three asymptotic regimes are accessed sequentially in order from Equation (30) to Equation (32).

It is important to note also that for the classical Thomson regime in Equation (30) to be effectively realized in practice, the neutron star local magnetic field must be relatively low, considerably lower than the field choices illustrated. When B approaches a sizeable fraction of unity, the constraint on γ_e pushes the scattering into the Klein–Nishina domain $\gamma_e \varepsilon_s \sim 1$, wherein the simplifying assumptions concerning the cross section that underpin this asymptotic result are strictly not valid. In order to realize a truly Thomson regime, one requires $B^2/\alpha_{\mathrm{f}} \ll 10^{-3}$, specifically $B \lesssim 3 \times 10^{-4}$ (i.e., $\lesssim 10^{10}$ G). This will occur only at moderately high altitudes in conventional pulsars, such as 10 stellar radii above the surface, or down near the surface of a millisecond pulsar. For proximity of collision locales to the polar cap of normal or high-field pulsars, the Klein–Nishina reductions and recoil effects embodied in the full magnetic scattering cross section must be included, thereby motivating developments in the subsequent sections, the focal thrust of this paper.

4. ELECTRON COOLING RATES IN SUPERSTRONG FIELDS

While the cyclotron resonance to the scattering process is encapsulated in quantum formulations, it is not an intrinsically quantum aspect: it is obtained in classical descriptions (e.g., Canuto et al. 1971) that introduce it via magnetic modifications to the dispersion relation. Quantum effects such as Klein–Nishina declines and electron recoil influences extend beyond the resonance and can be seen in a range of energies in the ERF. Here, fully quantum regimes where $B \gtrsim 0.1$ are explored. The focus is on surface emission at the polar cap, where the photon angular distribution is uniform within a cone whose axis coincides with the neutron star magnetic dipole axis; the next section will treat rates appropriate to arbitrary locales in the magnetosphere. First, we explore the particular characteristics of high-field regimes where electron recoil and Klein–Nishina declines are paramount. Then we consider thermally distributed soft photons and highlight how even a modest breadth in the range of ε_s, such as that present in the Planck spectrum, profoundly alters the resonant rates. Then this section will conclude with a brief exposition on the mean energy loss in γ–e collisions that isolates the field domain for which recoil is significant.

4.1. Characteristics of High-field Regimes: Monoenergetic Soft Photons

Cooling rates discussed here are computed using the full formulation in Equation (9). These are double integrals in general, though we anticipate analytic developments in Section 4.2 below that will reduce one of these integrations. For now, specialization to monoenergetic soft photons is retained. For the purposes of illustration, the spin-averaged JL cross section in Equation (13) is employed in computing these rates. The numerical results, obtained using Mathematica coding, are displayed in Figure 3, for two local field strengths $B = 1, 10$. When the
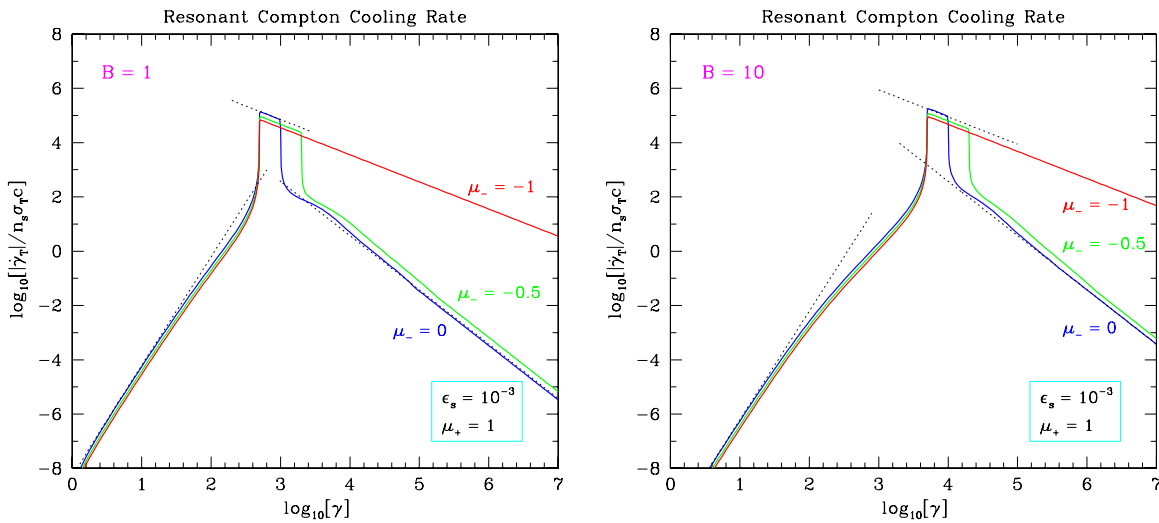
Figure 3. Resonant Compton cooling rates for two different field strengths, $B = 1$ (left panel) and $B = 10$ (right panel), again in units of $B_{cr} \approx 4.413 \times 10^{13}$ G. These are computed using the QED differential cross section in Equation (13). The soft photon energy distribution is monoenergetic, with $\varepsilon_s = 10^{-3}$, corresponding to typical surface X-ray temperatures. In each panel, three cases are depicted: isotropic ($\mu_- = 1$) and hemispherical ($\mu_- = 0$) soft photons, and an intermediate case, $\mu_- = -1/2$. In both panels, the dotted lines encapsulate the asymptotic approximations listed in Equations (32), (37), and (38) for the $\mu_- = 0$ hemispherical soft photon case.

(A color version of this figure is available in the online journal.)

rates are computed using the spin-dependent ST cross section, similar curve morphology emerges. The rates are obtained for soft photons distributed uniformly within conical sectors with axes coincident with the **B** vector. All cases have $\mu_+ = 1$, so that head-on collisions abound; the curves therefore represent interactions at the magnetic pole near (or just beneath) the stellar surface for electrons heading into the neutron star. The cooling rate curves display a steeply rising portion below the resonance peak, a $1/\gamma_e$ dependence in the resonance "plateau," and steeply declining section at γ_e above the resonance. It is this high Lorentz factor regime that evinces profoundly different character from that in the Thomson domain exposition in Figure 2: the rapid decline reflects the reduction of the cross section in the Klein–Nishina regime when $B \gtrsim 1$ (see Gonthier et al. 2000). Since the Thomson cross section in Equation (23) does not possess such a decline, the cooling rates illustrated in Figure 2 exhibit the classic γ_e^2 Thomson cooling rate at high γ_e. Therefore, when $B \gtrsim 0.03$, the full relativistic quantum cross section must be used.

It is insightful to generate analytic approximations pertinent to Figure 3. In supercritical fields, whenever $\omega_i \gg 1$ the differential cross section in Equation (13) is extremely sensitive to the amount of electron recoil in a scattering, by virtue of the exponential factor. Specifically, the focus here is on the $\omega_i^2/B \gg 1$ domain. This spawns a strong dependence of $d\sigma_{JL}/d(\cos\theta_f)$ on θ_f, with the dominant contribution arising from narrow collimation about forward scattering, $\theta_f \approx 0$. The collimation is controlled by the exponential factor so that outside the range $(1 - \cos\theta_f) \lesssim 3B/\omega_i^2$, corresponding to recoil being either moderate or strong, the contributions to the differential cross section and the total cooling rate are insignificant when $B \gg 1$ and $\omega_i \gg 1$. With this restriction, $\omega_f \approx \omega_i$ and the kinematics are quasi-Thomson. The differential cross section in Equation (13) accordingly simplifies dramatically to

$$\frac{d\sigma_{JL}}{d(\cos\theta_f)} \approx \frac{3\sigma_T}{8} \exp\left\{-\frac{\omega_i^2}{B}(1 - \cos\theta_f)\right\} \Sigma_\kappa\left(\frac{\omega_i}{B}\right), \quad (33)$$

using the definition of $\Sigma_\kappa(\psi)$ in Equation (24). Furthermore, the Jacobian in Equation (9) again reduces to a simple form $|\partial\varepsilon_f/\partial(\cos\theta_f)| = \gamma_e\beta_e\omega_f \approx \gamma_e\beta_e\omega_i$, so that the cooling rate in Equation (9) for $B \gg 1$ is analytically tractable. The dominant contribution from the relative velocity factor $1 - \beta_e\cos\theta_f = (1-\beta_e) + \beta_e(1-\cos\theta_f)$ is from the $\beta_e(1-\cos\theta_f)$ portion, since β_e is so nearly unity. Assuming a uniform beam of incoming photons such that $f(\mu_i) = 1$ on $\mu_- \leqslant \mu_i \leqslant \mu_+$, the θ_f integration is simple, and the resulting compact result is

$$\dot{\gamma}_e \approx -\frac{3n_s\sigma_T c}{8(\mu_+ - \mu_-)} \frac{B^3}{\gamma_e\beta_e\varepsilon_s^2}\left[\mathcal{I}_\kappa^{-2}(\psi_+) - \mathcal{I}_\kappa^{-2}(\psi_-)\right],$$

$$\psi_\pm = \frac{\gamma_e\varepsilon_s}{B}(1 + \beta_e\mu_\pm). \quad (34)$$

The definition of the $\mathcal{I}_\kappa^{-2}$ function is given in Equation (26), and it can be expressed as

$$\mathcal{I}_\kappa^{-2}(\psi) = -\frac{1}{1+\psi} + \frac{1}{\kappa}\arctan\left(\frac{\psi - 1}{\kappa}\right),$$

$$c_0(\kappa) \equiv \mathcal{I}_\kappa^0(1) = -\frac{1}{2}. \quad (35)$$

Again, since generally $\kappa \ll 1$, the mathematical character of $\mathcal{I}_\kappa^{-2}(\psi)$ is that of a step function smoothed on the scale of κ. Useful asymptotic forms for $\mathcal{I}_\kappa^{-2}(\psi)$ are given by

$$\mathcal{I}_\kappa^{-2}(\psi) \approx \begin{cases} -\dfrac{\pi}{2\kappa} - \dfrac{\kappa^2}{3} + \psi - \psi^2 + O(\psi^3) + O(\kappa^2), & \psi \ll 1, \\[2mm] \dfrac{\pi}{2\kappa} - \dfrac{1}{\psi} + \dfrac{1}{\psi^2} + O\left(\dfrac{1}{\psi^3}\right) + O(\kappa^2), & 1 \ll \psi. \end{cases}$$

$$(36)$$

Equation (34) formally applies only to $B \gg 1$ regimes. An alternative formulation that addresses arbitrary field strengths is offered in Section 4.2 below.

As with the Thomson regime considerations, there are three main asymptotic domains of potential interest here. At low Lorentz factors, specifically when $\gamma_e\varepsilon_s \ll 1$, the relevant analytic approximation is that in Equation (32), so that $\dot{\gamma}_e \propto \gamma_e^4$.

This form is depicted in both panels of the figure and again follows from the $\sigma \propto \omega_i^2$ dependence of the cross section. When $\gamma_e \varepsilon_s$ exceeds unity, but still is below B, Klein–Nishina reductions emerge below the resonance. This regime is evident for the $B = 10$ case in Figure 3. The resonant cooling rate for highly supercritical fields is

$$\dot{\gamma}_e \approx -\frac{3\pi}{4}\frac{n_s\,\sigma_{\rm T}c}{\mu_+ - \mu_-}\frac{B^4}{\gamma_e\beta_e\varepsilon_s^2}\frac{1}{\Gamma}$$

$$= -\frac{9\pi}{16\alpha_{\rm f}}\frac{n_s\,\sigma_{\rm T}c}{\mu_+ - \mu_-}\frac{B^2}{\gamma_e\beta_e\varepsilon_s^2}, \qquad (37)$$

if we use the low-field cyclotron decay width. Well above the resonance, recoil influences are profound, Klein–Nishina reductions are dramatic, and the cooling rate is

$$\dot{\gamma}_e \approx -\frac{3}{4}\frac{n_s\,\sigma_{\rm T}c}{(1 + \beta_e\mu_+)(1 + \beta_e\mu_-)}\frac{B^2}{\gamma_e^2\varepsilon_s^3},$$

$$1 \ll B \ll \gamma_e\varepsilon_s(1 + \beta_e\mu_-), \qquad (38)$$

where the $\psi \gg 1$ limit of Equation (36) has been invoked. This limit is depicted in the figure. Clearly, for isotropic soft photons with $\mu_- = -1$, it is never realized since the resonance can always be accessed kinematically for large γ_e, so that the resonant contribution dominates all others. It will become evident below, that distributing the soft photon energies can also circumvent the appearance of a regime exhibiting this profoundly reduced cooling rate.

4.2. Thermal Soft Photons

Contributions to pulsar and magnetar spectra in the X-ray band from the neutron star surface are necessarily approximately thermal, due to the high radiative opacities in their atmospheres. The spectrum is not expected to be of a perfect Planck form because there are radial and colatitudinal temperature gradients; line processes can be involved in its formation, and therefore Kirchhoff's Third Law seeds the expectation that absorption lines can be present. A plethora of theoretical models of neutron star atmospheres exist, differing in assumptions about composition, ionization balance, and active radiative transport processes. Generally, they now predict non-Planckian forms with at most modest spectral structure due to the smearing of features by spatial distribution or vacuum polarization effects (e.g., see Bulik & Miller 1997; Özel 2001; Ho et al. 2007, and references therein). Discrete lines have not been unambiguously observed below 10 keV, but there are indications of deviations from isothermal Planck forms. For example, state-of-the-art spectroscopy of some neutron stars, like RX J1856.53754, in the *Chandra/XMM-Newton* era suggests two-component blackbody models as the best fits to data (e.g., see Burwitz et al. 2003). In addition, radiative transfer and heat conduction in surface layers is heavily suppressed perpendicular to the field, so the photon distribution must be decidedly anisotropic, as discussed by Zavlin et al. (1995), Pérez-Azorín et al. (2005), and Mori et al. (2007). This anisotropy and departures from Planck spectral form for the soft photons are higher order influences on resonant Compton cooling rates. The focus here is the exploration of the major features of distributing the soft photons in energy beyond the delta function approximation in Equation (5). To this end, for interaction locales on the magnetic polar axis, the Planck spectral form

$$n_\gamma(\epsilon_s) = \frac{\Omega_s}{\pi^2\lambdabar^3}\frac{\epsilon_s^2}{e^{\epsilon_s/\Theta} - 1} \qquad (39)$$

is employed in the computation of Equation (9) for the Compton cooling rate. Here, $\Theta = kT/m_ec^2$ is the dimensionless temperature of the thermal surface photons, and $\lambdabar = \hbar/(m_ec)$ is the Compton wavelength over 2π. Also, Ω_s represents the solid angle of the blackbody photon population, divided by 4π. This fractional solid angle is introduced to accommodate anisotropic soft photon cases, in particular hemispherical populations ($\Omega_s = 1/2$) just above the stellar atmosphere. The total number density of soft photons is therefore $2\Omega_s\zeta(3)/(\pi^2\lambdabar^3)$, for $\zeta(n)$ being the Riemann *zeta* function. The analysis of this section will be restricted to interaction points on the magnetic axis, for which the angular distribution is flat topped and within a range specified in Equation (63). In such axisymmetric cases, the solid angle factor Ω_s is neatly separable from the ω_i integration. As will soon be apparent, the spreading of seed photon energies profoundly alters the morphology of the cooling rate curves at high Lorentz factors γ_e, a feature that is apparent in magnetic Thomson cooling rate expositions (e.g., Dermer 1990; Sturner 1995).

The triple integration in Equation (9) for photons with a Planck spectrum is computationally expensive. Below the resonance, the integrands are relatively stable and Mathematica was used without undue burden on the integration time. At the high Lorentz factors where the resonance is generally sampled, numerical evaluations of the triple integration are computationally inefficient, and asymptotic approximations are desirable. The dominance of the resonance in determining the rate does in fact lead to analytic simplification of the integrations, so that two of them can be rendered tractable, thereby leaving a single numerical integration. Retaining the full mathematical structure of the Lorentz profile limits the simplification: if one imposes just a $\gamma_e \gg 1$ approximation, then the cooling rates distill to double integrations. In either case, the non-resonant term in the cross section is neglected as a small contribution whenever the cyclotron resonance is sampled. The analysis for these developments is presented in Appendix A; here an outline of the results is presented. If one takes the $\gamma_e \gg 1$ limit, the Jacobian factor in Equation (9) simplifies according to Equation (A1). Then a change of variables for the angle integration is employed. Consider first the JL resonant cross section, which constitutes the first piece in Equation (13). For monoenergetic soft photons, these manipulations yield a JL cooling rate in and near the resonance of

$$\dot{\gamma}_{e,{\rm JL}} \approx -\frac{3}{4}\frac{n_s\,\sigma_{\rm T}c}{\mu_+ - \mu_-}\frac{1}{\gamma_e\varepsilon_s^2}$$

$$\times \int_{\omega_-}^{\omega_+}\frac{\mathcal{F}(z_\omega,\,p) - \mathcal{G}(z_\omega,\,p)}{(\omega_i - B)^2 + (\Gamma/2)^2}\frac{\omega_i^4\,d\omega_i}{(1 + 2\omega_i)^2},$$

$$z_\omega = 1 + \frac{1}{\omega_i}, \qquad (40)$$

for $p = \omega_i/B \approx 1$ parameterizing how ω_i maps through the peak and wings of the resonance. As before, $\omega_\pm = \gamma_e\varepsilon_s(1 + \beta_e\mu_\pm)$ defines the kinematic extrema of incoming photon energies in the ERF. The functions $\mathcal{F}$ and $\mathcal{G}$ express the integration over $\cos\theta_f$ and take the functional forms

$$\mathcal{F}(z,\,p) = \int_0^{\Phi(z)}\frac{f(z,\,\phi)\,e^{-p\,\phi}\,d\phi}{\sqrt{1 - 2z\phi + \phi^2}},$$

$$\mathcal{G}(z,\,p) = \frac{2(z-1)}{(1+z)^2}\int_0^{\Phi(z)}\frac{g(z,\,\phi)\,e^{-p\,\phi}\,d\phi}{(1-\phi)\sqrt{1 - 2z\phi + \phi^2}},$$

$$(41)$$

for $f(z, \phi)$ and $g(z, \phi)$ being polynomial functions of z and ϕ as defined in Equations (A15) and (A16), respectively. The incoming photon energy parameter is conveniently expressed via

$$\Phi(z) = z - \sqrt{z^2 - 1} \quad \Leftrightarrow \quad z = \frac{1}{2}\left(\Phi + \frac{1}{\Phi}\right) \qquad (42)$$

thereby defining the upper limit to the integrals in Equation (41), with $0 \leqslant \Phi(z) < 1$ for $z \geqslant 1$. Both $\mathcal{F}$ and $\mathcal{G}$ can be approximated by analytic functions to the required accuracy, as described in Appendix B, sparing the user of a numerical evaluation of the integrals. Series expansions of the integrations in terms of Legendre functions are possible, but do not significantly expedite the evaluations. A similar form for the resonant rates is obtained for the general ST cooling rate in and near the resonance:

$$\dot{\gamma}_{e,\text{ST}} \approx -\frac{3}{16} \frac{n_s \sigma_T c}{\mu_+ - \mu_-} \frac{1}{\gamma_e \varepsilon_s^2}$$
$$\times \sum_{s=\pm 1} \int_{\omega_-}^{\omega_+} \frac{(s\varepsilon_\perp + 1)\Upsilon_s(z_\omega, p)}{(\omega_i - B)^2 + (\Gamma_s/2)^2} \frac{\omega_i^4 d\omega_i}{(1 + 2\omega_i)^2},$$
$$z_\omega = 1 + \frac{1}{\omega_i}, \qquad (43)$$

for $p = \omega_i/B \approx 1$, and

$$\Upsilon_s(z, p) = \left\{\left(\frac{s}{\varepsilon_\perp} + 1\right)[\mathcal{F}(z, p) - \mathcal{G}(z, p)]\right.$$
$$\left. + \left(\frac{s}{\varepsilon_\perp} - 1\right)[\mathcal{F}_\Delta(z, p) - \mathcal{G}_\Delta(z, p)]\right\}. \quad (44)$$

The label $s = \pm 1$ refers to the spin-state quantum number for the intermediate electron. The $\mathcal{F}_\Delta$ and $\mathcal{G}_\Delta$ functions are specified by

$$\mathcal{F}_\Delta(z, p) = (z + 1)\int_0^{\Phi(z)} \frac{\phi(1-\phi)e^{-p\phi}}{\sqrt{1 - 2z\phi + \phi^2}} d\phi$$
$$\mathcal{G}_\Delta(z, p) = 2\frac{z-1}{z+1}\int_0^{\Phi(z)} \frac{\phi^2(z + 2\phi z - \phi^2)e^{-p\phi}}{(1-\phi)\sqrt{1 - 2z\phi + \phi^2}} d\phi, \qquad (45)$$

and, like $\mathcal{F}$ and $\mathcal{G}$, can be approximated by analytic functions (detailed in Appendix B).

Both Equations (40) and (43) represent single integrations within this construct. For the cases treated here of interaction points on the magnetic axis, the additional integration over the Planck spectrum in Equation (39) can be handled in an analytic manner by reversing the order of the resulting double integral and using the definition/identity

$$\ell_T(\chi) = \int_\chi^\infty \frac{dx}{e^x - 1} \equiv \log_e \frac{1}{1 - e^{-\chi}}. \qquad (46)$$

With this re-ordering, the ω_i integrations for the two rates are semi-infinite, i.e., on the interval $0 \leqslant \omega_i \leqslant \infty$, but the ε_s integration is now over a finite interval, defined by

$$\chi_- \leqslant \chi \equiv \frac{\varepsilon_s}{\Theta} \leqslant \chi_+ \qquad \chi_\pm = \frac{B}{\gamma_e \Theta(1 + \beta_e \mu_\mp)}. \qquad (47)$$

One can then quickly write down the result for the neighborhood

of the resonance in the ST formulation as

$$\dot{\gamma}_{e,\text{ST}} \approx -\frac{3\Omega_s}{16} \frac{n_s \sigma_T c}{\gamma_e}\{\ell_T(\chi_+) - \ell_T(\chi_-)\}$$
$$\times \sum_{s=\pm 1} \int_0^\infty \frac{(s\varepsilon_\perp + 1)\Upsilon_s(z_\omega, p)}{(\omega_i - B)^2 + (\Gamma_s/2)^2} \frac{\omega_i^4 d\omega_i}{(1 + 2\omega_i)^2}, \qquad (48)$$

with a similar factor $\ell_T(\chi_+) - \ell_T(\chi_-)$ appearing in the equivalent JL formulation. Generally, this factor has approximately logarithmic dependence on γ_e and is of the order of unity for $\chi_- \lesssim 1$, however when $\chi_- \gg 1$ and the angular phase space for access to resonant interactions samples the high-energy tail of the Planck spectrum, the resonant rate is exponentially suppressed. Such compact forms were used to compute asymptotic results for the cooling rates in the resonant domains for the graphical illustrations in the remainder of this paper.

One remaining analytic refinement is addressed before proceeding to the display of numerical results. For all field strengths, the width of the resonance is comparatively small, in the sense that $\Gamma \ll B$, a statement that applies to the spin-averaged width in Equation (22), but also extends to spin-dependent contexts when Equation (17) is employed. In such cases, the Lorentz profile in Equations (40) and (43) can be approximated by a delta function in ω_i space of identical normalization:

$$\frac{1}{(\omega_i - B)^2 + (\Gamma/2)^2} \rightarrow \frac{2\pi}{\Gamma} \delta(\omega_i - B). \qquad (49)$$

This then trivially evaluates the ω_i integration. When also integrated over the Planck spectrum, the asymptotic expression for the resonant ST rate, for monoenergetic electrons is

$$\dot{\gamma}_{e,\text{ST}} \approx -\frac{3\Omega_s}{4\pi} \frac{\sigma_T c}{\lambda^3} \frac{\Theta}{\gamma_e \Gamma} \mathcal{R}_{\text{ST}}(B)\{\ell_T(\chi_+) - \ell_T(\chi_-)\},$$
$$\gamma_e \Theta \gtrsim B, \qquad (50)$$

using the function

$$\mathcal{R}_{\text{ST}}(B) = \frac{B^2}{(1+z)^2}\{[\mathcal{F}(z) - \mathcal{G}(z)] + [\mathcal{F}_\Delta(z) - \mathcal{G}_\Delta(z)]\}$$
$$\approx \begin{cases} \dfrac{2B^4}{3}, & B \ll 1, \\ B^2\left(1 - \dfrac{2}{e}\right), & B \gg 1, \end{cases} \qquad (51)$$

for $z = 1 + 1/B$, to define the major portion of the magnetic field dependence of the integrations over the resonance. Here, $\mathcal{F}(z) \equiv \mathcal{F}(z, 1)$ represents the $p = \omega_i/B = 1$ specialization, and similarly for $\mathcal{G}$, $\mathcal{F}_\Delta$, and $\mathcal{G}_\Delta$. Observe that when $\mu_- = 0$, as is the case for outgoing electrons at the neutron star surface, $\ell_T(\chi_+) \rightarrow 0$. The equivalent result to Equation (50) for the JL formulation is simply obtained by replacing $\mathcal{R}_{\text{ST}}(B)$ by the function $\mathcal{R}_{\text{JL}}(B)$ that is given by

$$\mathcal{R}_{\text{JL}}(B) = \frac{2B^2}{(1+z)^2}\{[\mathcal{F}(z) - \mathcal{G}(z)]\}$$
$$\approx \begin{cases} \dfrac{4B^4}{3}, & B \ll 1, \\ B^2\left(1 - \dfrac{2}{e}\right), & B \gg 1. \end{cases} \qquad (52)$$

The JL $B \ll 1$ limit, when substituted into Equation (50), reproduces exactly the thermal cooling rate in Equation (54) of
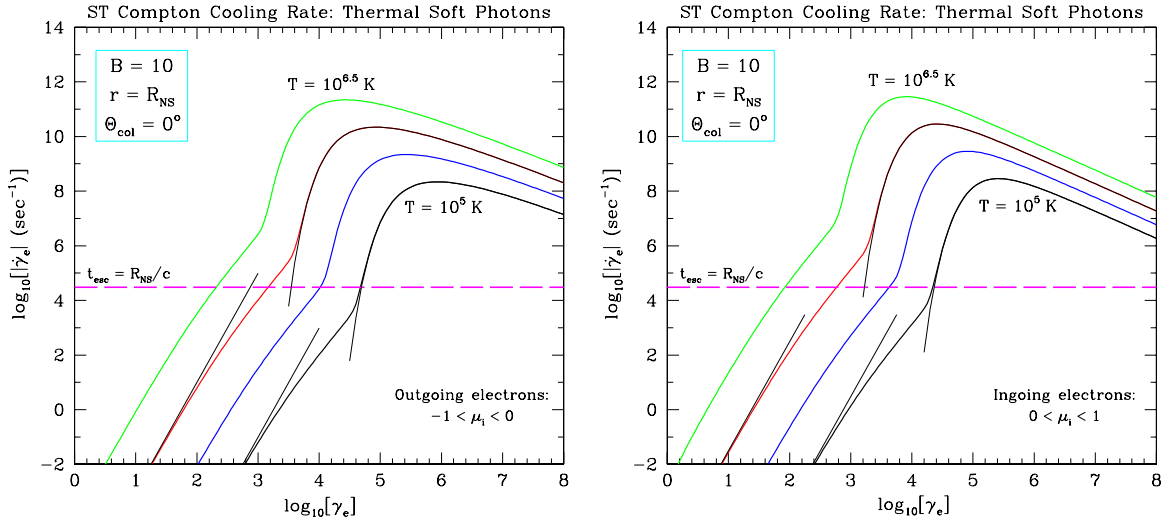
Figure 4. Resonant Compton cooling rates for field strength $B = 10$, in units of $B_{cr} \approx 4.413 \times 10^{13}$ G, for interaction locales at the surface ($r = R_{NS}$) and the magnetic pole ($\Theta_{col} = 0°$) of the neutron star. These are computed using the Sokolov & Ternov differential cross section in Equation (15) in the resonance, and the spin-averaged JL form in Equation (13) at all other ERF energies ω_i. The two cases depicted are for outgoing electrons (upward; left panel) and ingoing (downward; right panel) electrons. The soft photon energy distribution is thermal, with surface X-ray temperatures as labeled, and is isotropic within a hemisphere. In both panels, the lightweight lines encapsulate the asymptotic approximations for the resonant and non-resonant regimes, embodied in Equations (50) and (54), respectively. The horizontal dashed line denotes the light escape timescale t_{esc} corresponding to a stellar radius.

(A color version of this figure is available in the online journal.)

Dermer ([1990]) for choices of $\Omega_s = 1/2$, namely, hemispherical soft photons at the surface, and $\Gamma = 4\alpha_f B^2/3$, the standard classical cyclotron decay width. Comparing Equations (51) and (52), the ratio of the resonant cooling rates in the two formulations is just described by the simple function $\mathcal{R}_{ST}(B)/\mathcal{R}_{JL}(B)$ of the magnetic field strength:

$$\frac{\mathcal{R}_{ST}(B)}{\mathcal{R}_{JL}(B)} = \frac{1}{2}\left\{ 1 + \frac{\mathcal{F}_\Delta(z) - \mathcal{G}_\Delta(z)}{\mathcal{F}(z) - \mathcal{G}(z)} \right\}, \quad z = 1 + \frac{1}{B}. \quad (53)$$

This function ranges from $1/2$ in the magnetic Thomson domain, where $\Gamma_{+1} \ll \Gamma_{-1}$ in Equation (17), to unity in the ultraquantum, $B \gg 1$ regime, where the choice of wave functions is immaterial since the spin-dependent widths $\Gamma_{\pm 1}$ collapse to the spin-averaged one Γ. Note that the resonant cooling rates scale roughly as Θ/γ_e, modulo the logarithmic factors. If the electron Lorentz factor drops too low, the leading order mildly relativistic correction is of the order of $1/\gamma_e^2$; see, for example, Equation (35) of Harding & Muslimov ([1998]). The derived asymptotic rates at resonance (i.e., Equation (50) for the ST formulation and its JL equivalent) provide useful checks on the ensuing numerical evaluations and expressions that can be used with facility in resonant Compton cooling models for X-ray and gamma-ray emission in neutron star systems.

It is also possible to derive asymptotic approximations to the rate in the non-resonant regime at much lower Lorentz factors. By integrating Equation (32) over the Planck spectrum, in the low γ_e quasi-Thomson regime, all values of ε_s are sampled, and an analytic approximation is obtainable:

$$\dot{\gamma}_e \approx -\frac{8\pi^4 \Omega_s}{315} \frac{\sigma_T c}{\lambdabar^3} \frac{\gamma_e^4}{\beta_e} \frac{\Theta^6}{B^2} \{(1 + \beta_e\mu_+)^5 - (1 + \beta_e\mu_-)^5\},$$
$$\gamma_e\Theta(1 + \beta_e\mu_+) \ll B. \quad (54)$$

This result is applicable to both JL and ST formulations, since the differential cross section is independent of electron spin-state choice outside the resonance. It coincides precisely with the result one would generate by taking the leading order,
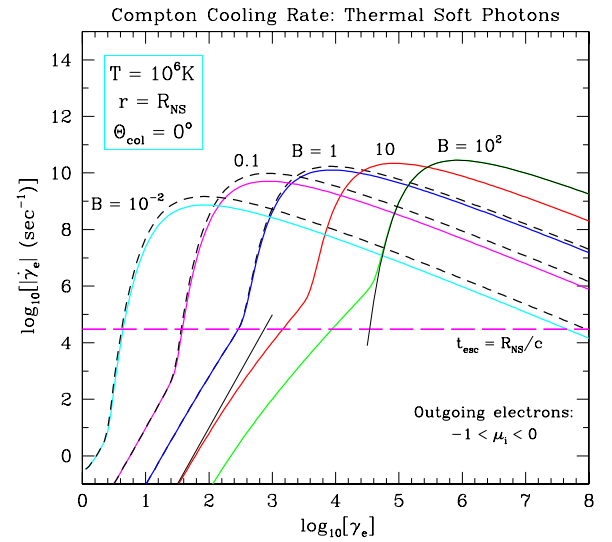

Figure 5. Resonant Compton cooling rates for five different field strengths, as labeled, and in units of $B_{cr} \approx 4.413 \times 10^{13}$ G. All curves are for surface thermal temperatures $T = 10^6$ K, for scatterings at the polar surface with colatitude $\Theta_{col} = 0°$, and for outgoing (upward moving) electrons. Solid curves are for Sokolov & Ternov (ST) cases, and the dashed curves for $B = 10^{-2}, 0.1, 1$ are Johnson & Lippmann (JL) evaluations. The $B = 10, 100$, JL evaluations are essentially indistinguishable on this plotting scale from their ST counterparts, and so were not exhibited. The light solid curve in the resonant regime is the $B = 100$ asymptotic ST result in Equation (50). The light solid straight line for the low γ_e, non-resonant regime is the $B = 10$ asymptotic result in Equation (54). As in Figure 4, the horizontal dashed line denotes the light escape timescale t_{esc} corresponding to a stellar radius.

(A color version of this figure is available in the online journal.)

γ_e^4, term of Equation (20) of Dermer ([1990]) and inserting the Planck spectrum of Equation (39) therein, for any choice of soft photon solid angle Ω_s. For the on-magnetic axis illustrations in Figures 4 and 5, the hemispherical choice $\Omega_s = 1/2$ is adopted, corresponding to near-surface electron–photon collisions. It should be emphasized that when $\gamma_e \lesssim 10$, this formula should

be corrected using more general forms of the differential cross section than are employed here, namely, those applying to non-zero incoming photon angles θ_i in the ERF. The mathematical involvement of such generalizations is substantial (e.g., see Daugherty & Harding 1986; Bussard et al. 1986) and is beyond the scope of the current work, whose focus is mainly on higher Lorentz factor, resonant domains.

Cooling rates for soft photons with the Planck distribution are exhibited in Figure 4. These constitute surface polar collisions for the two cases of outward-propagating (left panel) and inward-moving (right panel) electrons. While the outgoing case mimics the situation invoked on models of conventional gamma-ray pulsars, returning pair currents in such pulsars and twisted magnetosphere models for magnetars include the possibility of inward-propagating electrons. Of course, the Doppler beaming of scattered photon angles guarantees that such downward electron cases spawn upscattered photons that mostly impact and thereby heat the neutron star surface, if the interaction altitude is low. The morphology of the cooling rate curves in the figure is very similar for the two electron directions, with modest numerical differences incurred due to the differing angular phase space in scatterings for the two cases. Notably, greater logarithmic curvature is evident in the resonant domain for outgoing electrons since then $\chi_+ \gg \chi_-$. The key feature of these plots is that resonant interaction parameter space extends now to arbitrarily high Lorentz factors, contrasting the strong drops at the upper end of the "resonant plateaux" evinced in the monoenergetic soft photon cases. This extension of the resonant contribution, also realized in the magnetic Thomson studies of Dermer (1990), Sturner (1995), and Harding & Muslimov (1998), is borne in the fact that as γ_e increases, there is always a low soft photon energy ε_s available to access the cyclotron resonance at $\omega_i = B$. Therefore, the shapes of the cooling curves in the resonant contribution serve as inverted images of the Planck spectrum: the exponential tail is sampled in the sharp rises on the left, the peak being controlled by the $\varepsilon_s \sim \Theta = kT/(m_e c^2)$ regime, and the high γ_e portion where $\dot{\gamma}_e \propto 1/\gamma_e$ samples the Rayleigh–Jeans tail of the Planck distribution.

For each surface temperature T, the cooling curves depicted were calculated using the ST differential cross section in Equation (15) in the resonance, with the spin-averaged JL form in Equation (13) being employed at all other ERF energies ω_i. The numerical results were obtained as full two-dimensional integrations based on Equation (9), but employing an integration by parts over the ε_s variable so as to eliminate the ω_i integration, and the weaken sensitivity of the integrand to ε_s. This computational protocol can be simply adopted only for cases where $f(\mu_i)$ is constant over the integration range; hemispherical angular distributions satisfy this constraint. At this high field strength of $B = 10$, resonant JL cooling rates are indistinguishable on the scale of this plot from the displayed ST ones. Also depicted in the plots for $T = 10^5$ K and $T = 10^6$ K are the asymptotic resonant rates resulting from Equation (50), which are just single integrations. The precision of this asymptotic form is considerably better than 1% when compared with the full numerical integrations. Hence, it is expedient to use the asymptotic approximation whenever resonant cooling rates are needed in pulsar and magnetar models incorporating Compton upscattering interactions.

An illustration of the magnetic field dependence of the cooling rates at polar surface locales is offered in Figure 5, for outgoing electrons, and for Planckian soft photons of temperature $T =$

10^6 K possessing a hemispherical distribution ($\Omega_s = 1/2$). Close agreement with the ST asymptotic forms in Equations (50) and (54) is evident for the highlighted choices and is numerically obtained for all field strengths. For $B = 10$ and $B = 100$, the resonant JL cooling rates are indistinguishable on the scale of this plot from the displayed ST ones, deviating by less than around 2% for $B \gtrsim 10$. However, for $B = 1$, the dashed curve depicts the JL cooling rate that differs in the resonant domain from the ST one by a factor of 1.32, according to Equation (53), a departure that increases to a factor of ≈ 2 when $B = 10^{-2}$. A notable feature of this figure is that at the "peak" of the resonance, defined by $\gamma_e \sim B/\Theta$, the value of the cooling rate is almost independent of the field strength. This property can readily be deduced from Equation (50) using the supercritical field proportionality $\mathcal{R}_{ST}(B) \propto B^2$ in Equation (51) and also the width dependence $\Gamma \propto B$ deducible from Equation (22) in the same field regime. This behavior changes for subcritical fields. It is clear from Equations (50) and (51) that when $B \ll 1$, the cooling rates scale with field as B^2 at fixed γ_e, which indicates a decline of the peak rate as subcritical fields are accessed. Moreover, the difference between the $\dot{\gamma}_e \propto B^2$ behavior at $B \ll 1$ and the weaker dependence ($\dot{\gamma}_e \propto B$) in supercritical regimes is noteworthy. Previous Thomson regime expositions on cooling rates (e.g., Daugherty & Harding 1989; Dermer 1990; Sturner 1995), essentially employ the $B \ll 1$ limit of the JL field dependence listed in Equation (52). If extrapolated to the $B \gtrsim 1$ domain, such a protocol would introduce an overestimate of the resonant cooling rate by the factor $4B^4/(3\mathcal{R}_{ST})$, which is approximately $4B^2(1 - 2/e)/3$, when $B \gg 1$. This large inaccuracy motivates the deployment of the relativistic quantum magnetic scattering formalism offered here: a principal conclusion of this paper is that the QED cooling rates profoundly improve upon the older magnetic Thomson formulations when $B \gtrsim 0.1$.

One measure of the effectiveness of resonant Compton cooling is whether its length scale is shorter than the neutron star radius. One naturally anticipates that this may be the case near the neutron star surface, where the field is high, the X-ray photon bath is intense, and accordingly the scattering is very efficient. To assess this quantitatively, we form resonant Compton cooling lengths $\lambda_c = \gamma_e c/|\dot{\gamma}_e|$ from the cooling rates and plot them in Figure 6. For illustrative purposes, the λ_c are displayed only for ST evaluations of the cooling rates. The neutron star radius R_{NS} is highlighted to benchmark the cooling scales. It is evident that for this $B = 10$, polar colatitude example, when $T \gtrsim 3 \times 10^5$ K, $\lambda_c \lesssim R_{NS}$, and cooling is very efficient near the magnetic poles. This is true also near the equator, as will become evident when colatitudinal influences on the cooling rates are explored in Section 5. The shortest cooling lengths arise at the onset of the resonant contribution, which is defined by setting $\gamma_e \Theta \sim B$ in Equation (50), and approximating the logarithmic ℓ_T terms by unity. This generates the scaling

$$\lambda_c|_{\gamma_e \sim B/\Theta} \sim \frac{4\pi}{3\Omega_s} \frac{1}{\Theta^3} \frac{\lambda^3}{\sigma_T} \frac{B^2\Gamma}{\mathcal{R}_{ST}} \equiv \frac{1}{2\Omega_s\Theta^3} \frac{\lambda}{\alpha_f} \frac{B^2\Gamma}{\alpha_f\mathcal{R}_{ST}} \quad (55)$$

for the ST computation. Using Equation (22) for the width Γ, and Equation (51) for $\mathcal{R}_{ST}$, it becomes clear that the $B^2\Gamma/(\alpha_f\mathcal{R}_{ST})$ factor is $1/2$ when $B \ll 1$, i.e., is independent of B. For surface polar interaction locales, when $\Omega_s = 1/2$, this sets $\lambda_c \sim \lambda/(2\alpha_f\Theta^3)$ at the onset of resonant cooling in the magnetic Thomson domain. In contrast, for highly supercritical fields, the $B^2\Gamma/\mathcal{R}_{ST}$ factor yields a field dependence proportional to B, a signature of the Klein–Nishina reduction of the cross section in
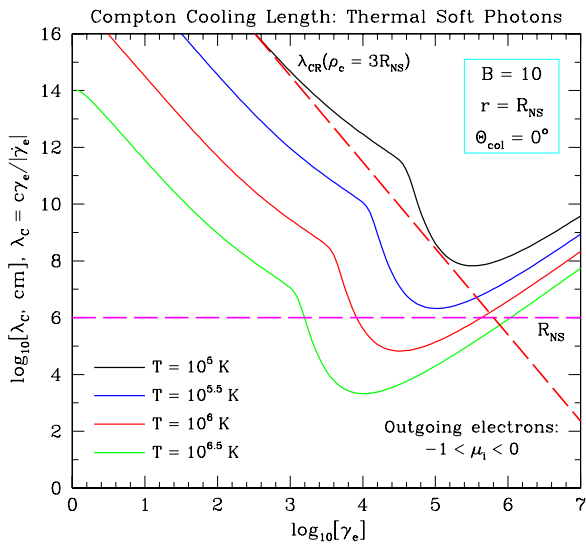
Figure 6. Resonant Compton cooling lengths for $B = 10$ corresponding to the cooling lengths in the left panel of Figure 4, for different X-ray soft photon temperatures, as marked. The outgoing electrons are scattered just above the polar cap ($\Theta_{col} = 0°$), and at the stellar surface ($r = R_{NS}$), so that the X-rays are defined by a hemispherical angular distribution. Only ST calculations are exhibited, with JL evaluations virtually coinciding with these curves because $B \gg 1$. The diagonal, dashed line represents the curvature radiation cooling length near the surface, according to Equation (56). When $T > 10^{5.5}$ K, cooling arises on scales shorter than R_{NS} for a range of e^- Lorentz factors.

(A color version of this figure is available in the online journal.)

this ultraquantum regime. Then $\lambda_c \sim 2\lambdabar B/(\alpha_f \Theta^3)$ for $B \gg 1$ at the magnetic pole on the stellar surface. Observe that the shapes of the cooling length curves are qualitatively similar to those computed in Daugherty & Harding (1989) and Sturner (1995), who both employed the magnetic Thomson cross section rather than the full magnetic QED forms that are the focus here.

It is natural to compare these results with the key length scale in polar cap models of gamma-ray pulsars. In these energetic neutron stars, the principal mechanism for primary photon production is curvature emission in the presumed dipolar field morphology. The cooling rate $\dot{\gamma}_{CR}$ for classical curvature radiation in pulsar models (e.g., Ruderman & Sutherland 1975; Daugherty & Harding 1982) can be employed to express the curvature emission cooling length λ_{CR}:

$$\dot{\gamma}_{CR} = -\frac{2}{3}\frac{r_0 c}{\rho_c^2}\gamma_e^4 \quad \Rightarrow \quad \lambda_{CR} = \frac{\gamma_e c}{|\dot{\gamma}_{CR}|} = \frac{3}{2\gamma_e^3}\frac{\rho_c^2}{r_0}. \quad (56)$$

Here, $r_0 = \alpha_f \lambdabar = e^2/(m_e c^3)$ is the classical electron radius. Also, ρ_c is the local radius of field curvature, which generally scales as the altitude r in a pulsar magnetosphere, except above the pole, where it scales as $r^{1/2}$. In general, $\rho_c > r$, and the curvature radius decreases with colatitude. As a representative case, the curvature cooling length λ_{CR} obtained from Equation (56) for the (optimal) near-surface interaction case $\rho_c/R_{NS} = 3$ is depicted in the right panel of Figure 6 as the steep, dashed red line. Clearly, if $\gamma_e \lesssim 10^{5.5}$, resonant Compton cooling is much more efficient than that due to curvature emission when $T \gtrsim 10^{5.5}$ K. The origin for this is obviously that the scattering process masquerades in some sense as stimulated cyclotron/synchrotron emission at the resonance, and so its efficiency far exceeds that for curvature radiation.

A different assessment of the efficiency of resonant Compton cooling is defined by the conditions under which it quenches electron acceleration in the magnetosphere. The rate of electro-

static acceleration in the magnetospheres of either gamma-ray pulsars or magnetars is largely an unknown commodity. The simplest assumption is that the parallel electric field $E_\parallel$ invoked in an electrostatic gap due to departures from Goldreich–Julian (Goldreich & Julian 1969) current flow (e.g., Shibata 1995; Takata et al. 2006) is a sizable fraction of the co-rotation $\mathbf{v} \times \mathbf{B}$ electric field, which scales as $\sim r\Omega B/c$. Such is approximately the case in twisted magnetosphere models for magnetar energization/dissipation (e.g., see Thompson & Beloborodov 2005; Zane et al. 2011). Defining an acceleration efficiency parameter η via $E_\parallel = 2\pi R_{NS}\eta B/(Pc)$, the electrostatic acceleration rate $\dot{\gamma}_{acc}$ and length scale λ_{acc} can quickly be written down

$$\dot{\gamma}_{acc} = \frac{2\pi \eta R_{NS} B}{P\lambdabar} \quad \Rightarrow \quad \lambda_{acc} = \frac{\gamma_e c}{|\dot{\gamma}_{acc}|} = \frac{\gamma_e}{2\pi B}\frac{\lambdabar Pc}{\eta R_{NS}},$$

$$\quad (57)$$

where the magnetic field B in this equation is expressed in units of B_{cr}. Evaluation of this for conditions typical of magnetars yields acceleration length scales of the order of $\lambda_{acc} \sim 10^{-2}$–$10^0$ cm when $\gamma_e \sim 10^4$; these short scales are consequences of the extremely high $E_\parallel$ assigned by a Goldreich–Julian construct near the surface of a magnetar. Such values are clearly inferior to the cooling lengths by at least three to four orders of magnitude; a similar situation arises for normal pulsars—see Figure 3 of Harding & Muslimov (1998). Accordingly, for resonant Compton to affect a radiation-reaction-limited acceleration (RRLA) in a magnetar, the accelerating fields must be weak enough to set $\eta \lesssim 10^{-4}$. Then, the maximum Lorentz factor is controlled by the onset of resonant interactions and is proximate to the minima exhibited in Figure 6 near $\gamma_e \sim B/\Theta$. RRLA is commonly invoked in models of young- and middle-aged gamma-ray pulsars using curvature emission at fairly high altitudes where the magnetic field is much weaker and λ_{CR} is much longer than illustrated in the figure. In such circumstances, higher values of η can be tolerated and the equality $\lambda_{acc} = \lambda_{CR}$ is realized for $\gamma_e \sim 10^6$–10^7. Then, cooling due to resonant Thomson scattering can intervene to temporarily slow, but not halt, the acceleration (e.g., Daugherty & Harding 1996; Harding & Muslimov 1998). Returning to magnetars, if η exceeds around 10^{-4}, then the accelerating electric fields must be quenched by some process other than resonant Compton cooling. Screening of the fields by magnetic pair creation $\gamma \rightarrow e^\pm$ is an obvious candidate, given its invocation in models of conventional pulsars. If the electrons can acquire modest pitch angles or populate sufficiently high Landau levels in the strong magnetic field, then RRLA spawned by cyclo-synchrotron radiation is also a possibility.

4.3. Mean Energy Losses for Electrons

The cooling rates computed so far are immediately useful for kinetic equation analyses where the cooling is *continuous*, i.e., changes in the electron energy incurred by resonant Compton interactions are small or infinitesimal: this is the Thomson scattering regime. In Compton cooling problems where Klein–Nishina domains are sampled and electron recoil is significant, kinetic equation formulations of the evolution of the electron distribution function require a more complicated treatment involving collisions integrals (e.g., see Blumenthal & Gould 1970), whose differences do not collapse to Fokker–Planck type differential constructs where $\dot{\gamma}_e$ explicitly appears. Therefore, it is instructive to assess when the resonant Compton process is in quasi-Thomson regimes, or when electron recoil is substantial. Intuitively, Klein–Nishina cases are expected to correspond to

$\gamma_e \varepsilon_s \gtrsim 1$ or $B \gtrsim 1$, and this turns out to be the case. To quantify this parameter space, here the *mean energy loss per collision* is calculated, as a function of neutron star parameters B (localized) and surface temperature Θ. This requires an additional derivation of the Compton *collision rate* to augment the cooling rates computed so far, which are essentially averages of the dimensionless electron energy loss, $-\Delta\gamma_e = \varepsilon_f - \varepsilon_i$, weighted by the differential cross section. The incoming photon energy can be neglected, so that the $\dot{\gamma}_e$ rates approximately average the value of $\Delta\gamma_e$. If the reaction rate of the collisions per electron is $\dot{n}_e/n_e = 1/\tau_e$, i.e., the inverse collision timescale, then the mean energy exchange per collision is

$$-\frac{\langle \Delta\gamma_e \rangle}{\gamma_e} = \frac{\tau_e |\dot{\gamma}_e|}{\gamma_e}. \tag{58}$$

The reaction rate can be assembled simply by replacing the $\varepsilon_f = \gamma_e \omega_f (1 - \beta_e \cos\theta_f) \equiv \omega_f/\gamma_e/(1 + \beta_e \mu_f)$ factor in the integrand of the cooling rate expression in Equation (6) by unity. The number density rate per electron can then be written down by applying this routine modification to Equation (9), which then yields

$$\frac{1}{\tau_e} = \frac{n_s c}{\mu_+ - \mu_-} \frac{1}{\gamma_e^3 \beta_e^2 \varepsilon_s^2}$$
$$\times \int_{\omega_-}^{\omega_+} \omega_i \, d\omega_i \int_{-1}^{1} d(\cos\theta_f) \frac{f(\mu_i)}{\omega_f} \left| \frac{\partial\varepsilon_f}{\partial(\cos\theta_f)} \right| \frac{d\sigma}{d(\cos\theta_f)}, \tag{59}$$

a minus sign being introduced to render the rate positive. The development of this integration is identical to that for the cooling rates and follows the procedures outlined in Appendix A. The collisional reaction rate can then be written in a form that parallels Equation (40), namely,

$$\frac{1}{\tau_{e,\text{JL}}} \approx \frac{3}{4} \frac{n_s \sigma_T c}{\mu_+ - \mu_-} \frac{1}{\gamma_e^2 \varepsilon_s^2}$$
$$\times \int_{\omega_-}^{\omega_+} \frac{\mathcal{F}_\tau(z_\omega, p) - \mathcal{G}_\tau(z_\omega, p)}{(\omega_i - B)^2 + (\Gamma/2)^2} \frac{\omega_i^3 \, d\omega_i}{1 + 2\omega_i},$$
$$z_\omega = 1 + \frac{1}{\omega_i}, \tag{60}$$

for $p = \omega_i/B \approx 1$, for the JL formulation; the partner result for ST collisional rates is given in Equation (A37). These forms can be routinely integrated over the Planck spectrum for the soft photons in Equation (39). Numerical computations of these collisional rates are not explicitly illustrated in this paper. The general forms for these rates are summarized in Appendix A via approximations appropriate to the resonant regime in Equations (A40) and (A41), together with low- and high-field asymptotic results.

Combining the cooling and collisional rates, the ratio in Equation (58) for the mean energy exchange per collision is illustrated in Figure 7 for the ST cross section. These were computed for surface interactions at the magnetic pole, where $\Omega_s = 1/2$, and soft photon temperatures $T = 10^5$ K and $T = 10^6$ K. We note that since both the cooling and collisional rates scale as Ω_s, the solid angle dependence drops out of the problem for on-magnetic axis locales. The curves evince a clear delineation between two regimes. At low Lorentz factors, $\gamma_e \lesssim 1/(10\Theta)$, the fractional energy loss by the electrons is much less than unity, and a quasi-Thomson regime emerges where the interactions are not resonant. This is the portion
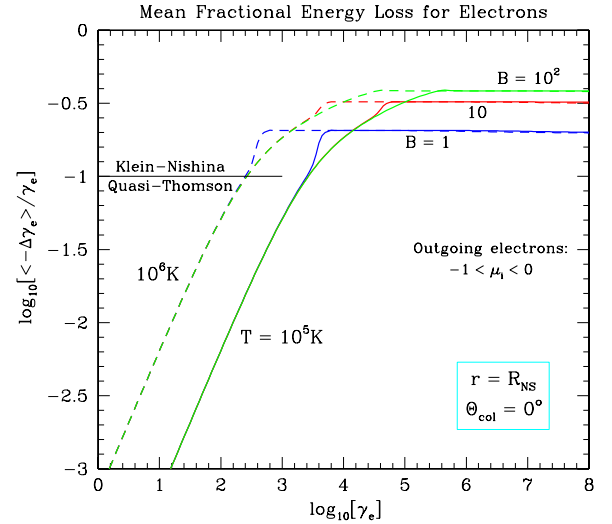

Figure 7. Mean fractional energy loss for electrons in magnetic Compton interactions, as defined in Equation (58), with thermal photons at the neutron star surface and at the magnetic pole ($\Theta_{\text{col}} = 0°$). The six cases correspond to two temperatures, $T = 10^5$ K (solid curves) and $T = 10^6$ K (dashed curves), and for each three magnetic fields, $B = 1, 10, 100$, as labeled. They constitute Sokolov & Ternov (ST) evaluations for outgoing (upward moving) electrons. At low Lorentz factors, $\langle -\Delta\gamma_e \rangle \ll \gamma_e$ and the scatterings are in the quasi-Thomson regime, with the mean fractional energy loss being given by Equation (61). At high γ_e, a magnetic Klein–Nishina regime delineated approximately by $\langle -\Delta\gamma_e \rangle/\gamma_e > 0.1$ is realized, where the upscattered photons acquire a sizable fraction of the incident electron energy. As $\gamma_e \to \infty$, the fractional energy loss depends only on B, and not on temperature T, as given by Equation (62).
(A color version of this figure is available in the online journal.)

of phase space where cooling modifications to the evolution of electron distributions can be modeled using Fokker–Planck forms for kinetic equations. Using the analysis in Appendix A, the ratio of the cooling rate in Equation (54) to the reaction rate in Equation (A44) for thermal soft photon spectra is independent of B and leads to

$$-\frac{\langle \Delta\gamma_e \rangle}{\gamma_e} = \frac{\tau_e |\dot{\gamma}_e|}{\gamma_e} \approx \frac{4\pi^6}{945\,\zeta(5)} \gamma_e \Theta \frac{(1 + \beta_e\mu_+)^5 - (1 + \beta_e\mu_-)^5}{(1 + \beta_e\mu_+)^4 - (1 + \beta_e\mu_-)^4},$$
$$\gamma_e \Theta \ll 1, \tag{61}$$

where $\zeta(n)$ is the Riemann *zeta* function. In the case where γ_e is moderately large so that $\beta_e \approx 1$ and $\mu_+ = 0, \mu_- = -1$ at the surface on the magnetic axis, the numerical factors yield a ratio of $3.924\gamma_e\Theta$. This analytic form nicely describes the curves in Figure 7 for $\gamma_e \lesssim 10^2$. Since the scattering in the ERF generates $\omega_f \approx \omega_i \propto \gamma_e\varepsilon_s$, i.e., Thomson kinematics, the upscattered photon energy in the OF scales as $\gamma_e^2\Theta$ so that one naturally anticipates a fractional energy change proportional to $\gamma_e\Theta$, and independent of the field strength. As expected, since the resonance is not sampled in this γ_e range, Equation (61) applies to both JL and ST cases.

At the higher γ_e, the mean energy exchange saturates at sizable fractions of unity that are dependent on the field strength. This Klein–Nishina domain of large electron recoil is coincident with resonant interactions, and for such Lorentz factors, the evolution of electron populations due to magnetic Compton cooling must be treated using full Boltzmann collisional integrals. The mean energy losses for $\gamma_e \gtrsim 1/\Theta$ are assembled in Appendix A; using Equations (A42) and (A43), together with the equivalent JL and ST asymptotic limits for the cooling rates earlier in Appendix A, it can be inferred that they possess the

limiting forms

$$-\frac{\langle \Delta \gamma_e \rangle}{\gamma_e} = \frac{\tau_e |\dot{\gamma}_e|}{\gamma_e} \approx \begin{cases} \frac{e-2}{e-1} \approx 0.418, & B \gg 1, \\ B, & B \ll 1. \end{cases} \quad (62)$$

Note that these limiting ratios apply to both JL and ST ratios, which are identical; in other words, the spin-dependent nuances in each of the cooling and collisional rates cancel in both the $B \ll 1$ and $B \gg 1$ domains. It should be noted that for field strengths in between these limits there is, in general, a modest difference between the JL and ST predictions for the mean energy loss, maximized at just under 9% in the $B \sim 2$–3 range. Clearly when $B \lesssim 1$, the resonant interactions do not sample Klein–Nishina reductions, and a magnetic Thomson description suffices. The insensitivity to the value of γ_e is evident from a comparison of Equations (40) and (60), from which one can also infer that integrating over the Planck spectrum will yield $\tau_e \dot{\gamma}_e / \gamma_e$ also independent of temperature, as is observed. In strong recoil regimes, information on the initial photon energy is obscured as the electron loses much of its energy in a scattering event. Note that the morphology of the curves in Figure 7 is similar for other interaction altitudes and colatitudes.

5. ALTITUDINAL AND COLATITUDINAL INFLUENCES

The focus on isotropic photon distributions of the previous section needs to be extended to include geometric influences at arbitrary locations in pulsar magnetospheres. The electron cooling rate determinations depend on the altitude r above the neutron star surface and the colatitude Θ_{col} away from the magnetic axis, due to the changing photon angle with respect to the magnetic field and because of a curtailed sampling of photons from the surface at high altitudes. We now assume that target X-ray photons are emitted uniformly and radially from the star surface, and thus at a given altitude are collimated in a cone of angle θ_c given by

$$\cos \theta_c = \sqrt{1 - \left(\frac{R_{\text{NS}}}{r}\right)^2}, \quad r \geqslant R_{\text{NS}} \quad (63)$$

(e.g., Rybicki & Lightman 1979; Dermer 1990). The solid angle of the soft photon population therefore is $\Omega_s \equiv 2\pi(1 - \cos \theta_c)$, so that $\Omega_s \approx (R_{\text{NS}}/r)^2$ describes the inverse-square law when $r \gg R_{\text{NS}}$. Departures from the simplification in Equation (63) are required when taking into account anisotropies that arise in radiative transfer models of magnetic neutron star atmospheres (e.g., Zavlin et al. 1995; Pérez-Azorín et al. 2005; Mori et al. 2007), and temperature non-uniformities in transitioning from polar to equatorial zones; treatment of such refinements is deferred to future work. In this section, we specialize to the dipole magnetic field, but other cases such as a twisted dipole field (e.g., Thompson & Beloborodov 2005) also follow the logical developments below, with just routine geometrical modifications. Also, in the analysis here, flat spacetime will be presumed, so that general relativistic effects are neglected: photons propagate in straight lines, and the photon energy and field morphology are not modified by a stellar gravitational potential. It is expected that the general character of the results presented here would not change appreciably with the accurate treatment of curved spacetime in Schwarzschild or rotating metrics. Including general relativistic effects such as magnetic field distortion and the enhancement of photon temperatures and densities in the local inertial frame, and the curvature of photon

trajectories, would incur only moderate changes to the shape and position of the cooling curves.

Considering interaction points remote from the magnetic axis, the local magnetic field is in general at an angle θ_{Br} with respect to the radial direction, which is easily found compactly using in the dipole form of the magnetic field $\vec{B} = B_0 r^{-3}(2 \cos \Theta_{\text{col}} \hat{r} + \sin \Theta_{\text{col}} \hat{\theta})/2$ in terms of specified colatitude $\theta \equiv \Theta_{\text{col}}$,

$$B = \frac{B_0}{2r^3}\sqrt{1 + 3\cos^2 \Theta_{\text{col}}},$$

$$\cos \theta_{Br} \equiv \frac{\vec{B} \cdot \hat{r}}{|\vec{B}|} = \frac{2\cos \Theta_{\text{col}}}{\sqrt{1 + 3\cos^2 \Theta_{\text{col}}}}. \quad (64)$$

The magnitude of the local magnetic field, central to the cross section and cyclotron width calculations, and of critical import at resonance, also depends on altitude and colatitude, and the surface polar magnetic field, B_0. At varying locales, we may have $\theta_c \leqslant \theta_{Br}$ or $\theta_c \geqslant \theta_{Br}$, the former being realized at high altitude or close to the magnetic equator, while the latter at low altitudes or close to the magnetic axis. These delineate two algebraic regimes in the ensuing analysis, corresponding to comparatively small or large radii of curvature for the field lines. For more generalized, non-dipolar magnetic field geometries, the principal modifications to the subsequent developments can be introduced via alternative expressions for B and θ_{Br} to those in Equation (64).

We wish to derive the $f(\mu_i)$ angular distribution function (normalized to unity) at a given colatitude and altitude as a function of the photon angle with respect to the magnetic field, $\Theta_i = \arccos \mu_i$, in the inertial frame of the star, but independent of the azimuthal angles since the cross section is independent of such. This involves the intersection of two spherical caps, one with a radial axis and one along the magnetic field direction, and an integration over the azimuthal angle with respect to the magnetic field; the global geometry is displayed in the left panel of Figure 8. Let Θ_i and ϕ_i denote the spherical polar and azimuthal angles, respectively, with respect to the magnetic field in the OF. Similarly, let θ_r and ϕ_r be the angles with respect to the radial vector at some colatitude θ. These angles and the pertinent geometry are displayed in Figure 8 for the case of outgoing electrons. The case of ingoing electrons differs from the outgoing case by the simple mirroring of the angular distribution, $\pi - \Theta_i \to \Theta_i$ in the ensuing algebra below. From spherical trigonometry's laws of cosines and sines, we have the following relations:

$$-\cos \Theta_i = \cos \theta_r \cos \theta_{Br} + \sin \theta_r \sin \theta_{Br} \cos \phi_r$$

$$\cos \theta_r = -\cos \theta_{Br} \cos \Theta_i - \sin \theta_{Br} \sin \Theta_i \cos \phi_i \quad (65)$$

$$\sin \theta_r = \frac{\sin \Theta_i \sin \phi_i}{\sin \phi_r}.$$

Here, θ_r is uniformly distributed in the range $0 \leqslant \theta_r \leqslant \theta_c$ reflecting the uniform brightness approximation of the surface emission, together with the constancy of light intensity during propagation in a flat spacetime. It is easy to show that the Jacobian of the solid angle transformation is unity between the two spherical caps, i.e., $d\mu_r d\phi_r = d\mu_i d\phi_i$, signifying the conservation of volume elements under rotations. Thus, the $f(\mu_i)$ dependence is imposed merely by geometrical restriction of the limits of integration over the azimuthal angles ϕ_i.

These limits are specified by the two values of the azimuthal angle ϕ_i at the intersection of extremities to the spherical
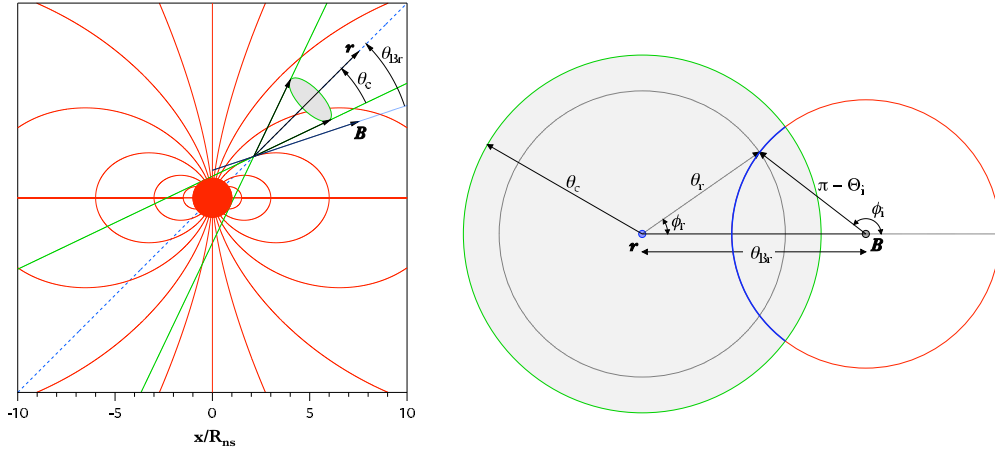
Figure 8. Geometry for Compton collisions at arbitrary altitudes and colatitudes in the magnetosphere. Left panel: magnetospheric view depicting an interaction point located at $r/R_{NS} = 3$ and a colatitude of $\Theta_{col} = 45°$. Here, θ_{Br} lies outside the soft photon cone of opening angle θ_c. The spatial scale is linear, in units of R_{NS}. Right panel: an outside blow-up perspective of the interaction cones, with the circles representing caps on angular cones with apexes at the interaction point $\vec{r}$. The left (shaded) circle defines the solid angle of the collimated soft photon cone above the stellar surface. The unshaded circle at the right represents the cap of a cone, whose axis coincides with the local $\vec{B}$ vector, and whose opening angle $\pi - \Theta_i$ defines the incoming photon angle with respect to **B** in the observer's frame. The highlighted (blue) arc on this circle that lies within the soft photon cone's cap signifies the azimuthal angles permitting interactions for a specified Θ_i. Various angles in the depicted triangle are related by spherical trigonometry according to Equation (65).
(A color version of this figure is available in the online journal.)

caps, corresponding to the "threshold" values $\pm\phi_{rt}$ of the azimuthal angle ϕ_r that are defined by the condition $\theta_r = \theta_c$ (see Figure 8, right panel), which has solutions provided that $|\theta_{Br} - \theta_c| \leqslant \pi - \Theta_i \leqslant \theta_{Br} + \theta_c$. Using the spherical law of cosines, these values are expressed as functions of Θ_i:

$$\phi_{rt} = \arccos[\mu_{rt}], \qquad \mu_{rt} \equiv \frac{-\cos\Theta_i - \cos\theta_c \cos\theta_{Br}}{\sin\theta_c \sin\theta_{Br}},$$
(66)

while taking the appropriate branch cut for the inverse trigonometric function arccos. The corresponding threshold angle ϕ_{it} is found in terms of ϕ_{rt} via the spherical law of sines,

$$\sin\phi_{it} = \frac{\sin\theta_c}{\sin\Theta_i}\sqrt{1 - \mu_{rt}^2},$$
(67)

so that the threshold intersection ϕ_{it} is given by the appropriate definition of arcsin such that $0 \leqslant \phi_{it} \leqslant \pi$. After some routine algebra, we can express ϕ_{it} terms of $\mu_\pm$ for the case $\theta_{Br} > \theta_c$,

$$\sin\phi_{it} = \frac{1}{\sin\theta_{Br}}\sqrt{\left[\frac{\mu_+ - \mu_i}{1 - \mu_i}\right]\left[\frac{\mu_i - \mu_-}{\mu_i + 1}\right]}, \quad \theta_{Br} > \theta_c.$$
(68)

Here, the lower (μ_-) and upper (μ_+) limits to the μ_i integration in the cooling rate are restricted to the domain, where $f(\mu_i)$ is non-vanishing, and hence become functions of altitude and colatitude according to

$$\mu_+ = -\cos(\theta_{Br} + \theta_c)$$
$$\mu_- = \begin{cases} -1, & \text{if } \theta_{Br} \leqslant \theta_c \\ -\cos(\theta_{Br} - \theta_c), & \text{if } \theta_{Br} > \theta_c \end{cases}$$
(69)

for the case of outgoing electrons. From these forms, one can deduce that on the magnetic axis, $(\mu_-, \mu_+) = (-1, -\cos\theta_c)$, and at the surface on the equator, $(\mu_-, \mu_+) = (-1, 1)$. It is clear that for $\mu_- < \mu_i < \mu_+$, the argument of the square root in Equation (68) is positive definite, and so that this equation can be inverted to generate a well-defined value of ϕ_{it}. The value of ϕ_{it} controls the azimuthal contribution to the angular distribution

for a particular interaction angle $\pi - \Theta_i$ with respect to the magnetic field direction.

Without loss of generality, the inversion of Equation (68) is established by restricting the range of the arcsin x function to the interval $[0, \pi/2]$. The extremities of this interval, where $|\sin\phi_{it}| = 1$, correspond to a critical value of Θ_i, denoted by $\hat{\Theta}_i = \arccos[\cos\theta_c/\cos\theta_{Br}]$. This division point delineates two branches to the inversion, encapsulated in the identity

$$\phi_{it} = \begin{cases} \arcsin\left[\frac{\sin\theta_c}{\sin\Theta_i}\sqrt{1 - \mu_{rt}^2}\right], \\ \qquad\qquad \text{if } \pi - \Theta_i \leqslant \arccos\left[\frac{\cos\theta_c}{\cos\theta_{Br}}\right] \\ \pi - \arcsin\left[\frac{\sin\theta_c}{\sin\Theta_i}\sqrt{1 - \mu_{rt}^2}\right] \quad \text{otherwise.} \end{cases}$$
(70)

These branches span the intervals $0 \leqslant \phi_{it} \leqslant \pi/2$ and $\pi/2 \leqslant \phi_{it} \leqslant \pi$, respectively. Integrating over the azimuthal angles as restricted above, and normalizing to unity when at the magnetic pole at the surface (i.e., $\Theta_{col} = 0°$ and $r = R_{NS}$), we obtain the angular distribution function for various cases,

$$f(\mu_i) = \begin{cases} 1 - \frac{1}{\pi}\phi_{it}(\Theta_i, \theta_{Br}, \theta_c), & \text{if } \Theta_i \neq \pi \text{ and } \theta_{Br} \neq 0 \\ 1, & \text{if } (\pi - \Theta_i \leqslant \theta_c \text{ and } \theta_{Br} = 0) \\ & \text{or } (\Theta_i = \pi \text{ and } \theta_{Br} < \theta_c) \\ 1/2, & \text{if } \Theta_i = \pi \text{ and } \theta_{Br} = \theta_c \\ 0, & \text{if } (\Theta_i = \pi \text{ and } \theta_{Br} > \theta_c) \\ & \text{or } \Theta_i < 0 \end{cases}$$
(71)

with $\cos\Theta_i = \mu_i \equiv [\omega_i/(\gamma_e\epsilon_s) - 1]/\beta_e$ forging a connection to the scattering kinematics. Clearly $f(\mu_i)$ vanishes on a domain that is a function of altitude and colatitude, a constraint transmitted through the values of θ_{Br} and θ_c. Angular distributions defined according to Equation (71) are depicted in Figure 9 and deployed in the computations below. Only intermediate colatitudes, $\Theta_{col} = 30°$ and $\Theta_{col} = 60°$, are illustrated. The polar axis cases are simple top-hat functions, while the equatorial cases are quasi-circular bubbles that are concentrically declining in size
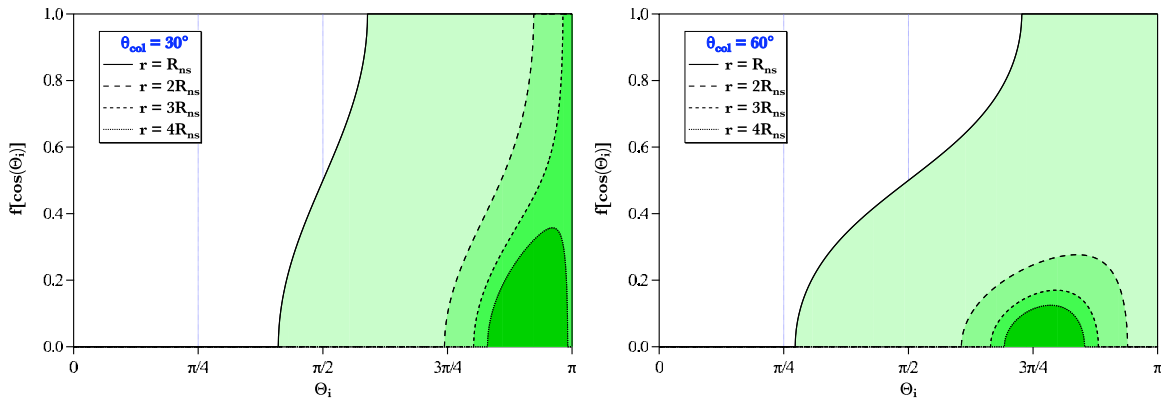
Figure 9. Shown here is the angular distribution function $f(\mu_i)$ for two intermediate colatitudes Θ_{col} and four altitudes r, as labeled, for outgoing electrons. It is readily apparent that as the photon cone becomes collimated at high altitudes, the phase space of angles around the local magnetic field is both distorted and curtailed, as highlighted for altitudes $r/R_{NS} = 1, 2, 3, 4$ by the solid, long-dash, short-dash, and dotted lines, respectively. Moreover, the normalization of the areas under $f(\mu_i)$ in μ_i coordinates as a function of altitude yields $1 - \mu_c$, i.e., the inverse-square law to first order at high altitudes. As one moves to the equatorial regions ($\Theta_{col} \sim 60°$–$90°$), the ranges of angles sampled migrate toward a phase space in the neighborhood of $\Theta_i = \pi/2$. Distributions for ingoing electrons are simply obtained by invoking a $\Theta_i \to \pi - \Theta_i$ transformation.

(A color version of this figure is available in the online journal.)

at high altitudes (much like the $\Theta_{col} = 60°$ case in Figure 9), and centered on and symmetric about $\Theta_i = \pi/2$. The declining size of the envelope loci with altitude reflects the dilution of the soft photon population with remoteness from the stellar surface.

Finally, the above derivation and analysis was performed for the case of upward propagating electrons for $0 \leqslant \Theta_{col} \leqslant \pi/2$. For the case of ingoing electrons, the polarity of **B** flips and distribution is identical to the outgoing case for $\pi/2 \leqslant \Theta_{col} \leqslant \pi$. Moreover, the downward propagating distribution for $0 \leqslant \Theta_{col} \leqslant \pi/2$ is simply a mirror of the upward case in terms of Θ_i, i.e., $\Theta_i \to \pi - \Theta_i$, along with some obvious redefinitions of $\mu_\pm$, namely, $\mu_- = \cos(\theta_{Br} + \theta_c)$ and $\mu_+ = \cos(\theta_{Br} - \theta_c)$ if $\theta_{Br} > \theta_c$. When $\theta_{Br} \leqslant \theta_c$, one sets $\mu_+ = 1$. These identities keep the original definition of θ_{Br} from Equation (64).

Numerical evaluations of the cooling rates at representative locales in the magnetosphere are illustrated in Figure 10. The rates were generally computed as fully three-dimensional integrals using Equation (9) as a basis, inserting in the angular distribution given by Equation (71), and then integrating over the Planck spectrum in Equation (39). The $\Theta_{col} = 0°$, $r = R_{NS}$ case was computed as detailed in Section 4.2. Most curves are displayed for ST cases, though each panel displays a single JL case for $r = 4R_{NS}$ for comparison (JL computations at other altitudes are omitted in the interest of clarity of the illustration). The resonant portions of JL cooling rates are closest to the depicted ST ones at the surface, where the fields are the strongest, and exhibit the greatest departures from ST values at high altitudes and therefore low local B (but never by more than a factor of two). Below the resonant portions, the JL and ST rates are, of course, identical. The general shapes and spectrum of regimes are similar for all altitudes and colatitudes of the interaction point: at low γ_e the cooling is non-resonant and approximately proportional to γ_e^4, and at high Lorentz factors, the cooling is resonant, sampling the Rayleigh–Jeans tail of the Planckian, and scales roughly as $1/\gamma_e$ (i.e., modulo logarithmic factors). These global characteristics extend to both lower and higher surface polar fields B_0, though the specific values for γ_e for the onset of the resonant cooling, and the normalizations of the cooling curves are modified accordingly, as identified in Section 4.

The principal differences in comparing curves for the various colatitudes are imposed by the kinematic constraints due to

the $\mu_\pm$ values in Equation (69) associated with the angular distribution. Above the magnetic pole, where photons and electrons are predominantly chasing each other, altitudinal collimation of the soft photons does not dramatically curtail the phase space for accessibility to resonant interactions beyond the $1/r^2$ dilution trend. There is significant compensation between the altitudinal decline of the $1 + \beta_e \cos \Theta_i$ factor in Equation (2) and the decline of B, so that the value of γ_e marking the onset of resonant collisions does not appreciably depend on r. The normalization of the resonant portion of the curves declines roughly as r^{-3}, reflecting the drop in the field strength at the locale of interaction. As the colatitude increases, the reduction of θ_c not only diminishes the number density of soft photons, but, for fixed γ_e, pushes the kinematic conditions that permit access to the resonance deeper into the Rayleigh–Jeans tail. This means that for fixed γ_e, there is both an impact of the altitude in reducing the range of μ_i values that contribute to the cooling rate, and a concomitant reduction in $\dot{\gamma}_e$ due to the decline in the field strength. Accordingly, these reinforcing effects precipitate a decline with r at the equator that is considerably faster than that above the pole. In addition, the effective pinning of $\Theta_i \approx \pi/2$ in high altitude equatorial regions forces the onset of resonant interactions to much lower Lorentz factors, being approximately described by $\gamma_e \propto B \propto r^{-3}$. This trend is evident in Figure 10(d).

In all cases, polar, equatorial, or in between, the onset of resonant cooling at $30 < \gamma_e < 10^4$ occurs on scales much shorter than the neutron star light crossing time, and also the curvature emission cooling timescale, at least for altitudes below around $5 - 10R_{NS}$ (i.e., coincident with the Compton resonaspheres enunciated in Baring & Harding 2007). This mirrors the discussion for surface polar locales at the end of Section 4.2. The implication is that for moderately scaled accelerating electric fields that permit resonant Compton RRLA (the radiation-reaction limit), the maximum electron Lorentz factors in the acceleration zone will be considerably lower for electrodynamic potentials located in the equatorial regions as opposed to polar zones. The scattering kinematics then sets the maximum dimensionless photon energy ε_f to be less than but around γ_e for Klein–Nishina interactions with strong recoil, or more appropriately $\gamma_e^2 \Theta$ for magnetic Thomson collisions when $B \lesssim 1$ at higher altitudes. Consequently, one expects
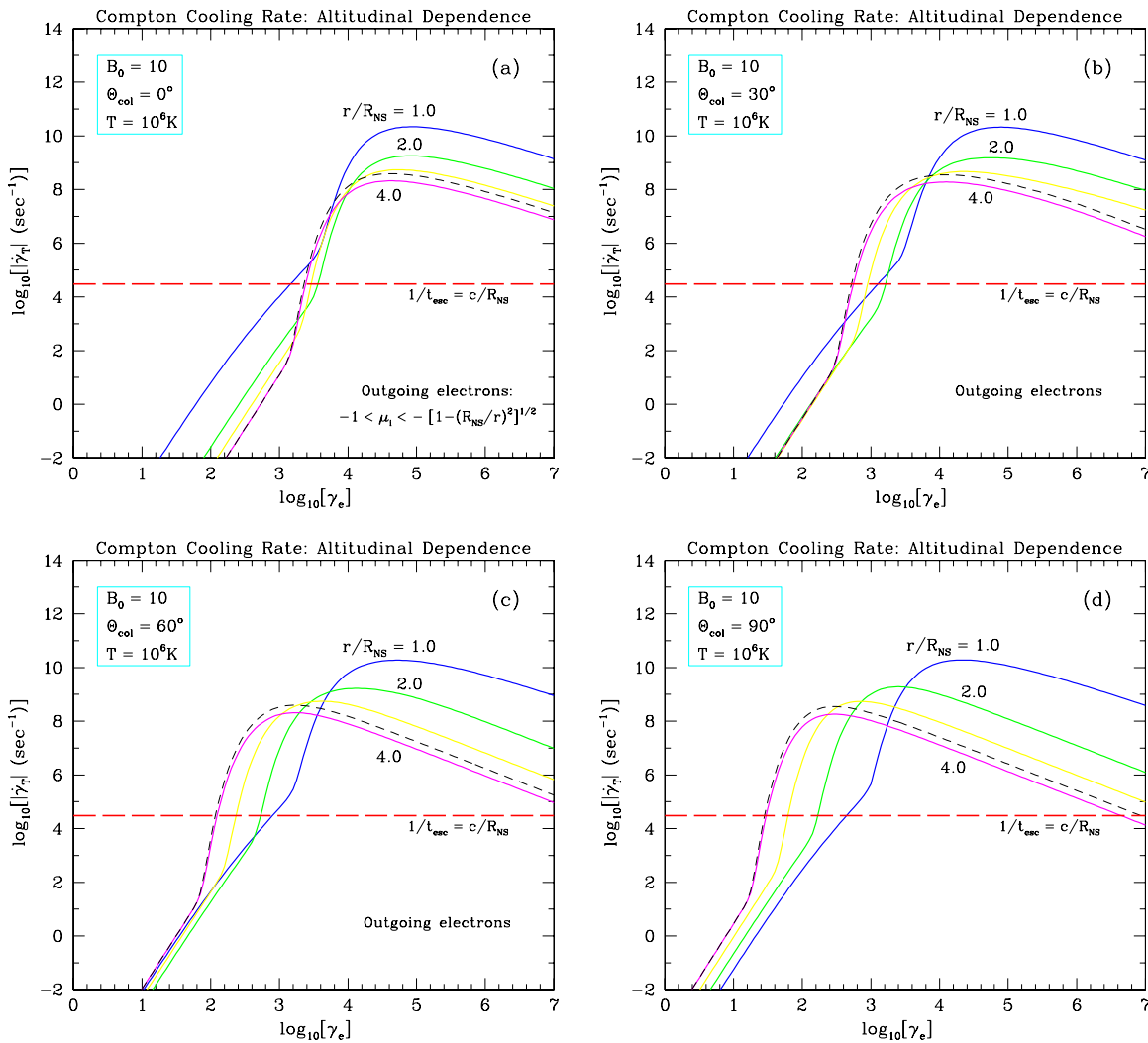
Figure 10. Resonant Compton cooling lengths for surface polar field strength $B_0 = 10$, as in Figure 4, for interaction locales at and above the surface ($r/R_{NS} = 1$ (blue), 2 (green), 3 (yellow, unlabeled), 4 (magenta), i.e., from top to bottom in the resonant regime) and at different magnetic colatitudes: (a) $\Theta_{col} = 0°$ (above the pole), (b) $\Theta_{col} = 30°$, (c) $\Theta_{col} = 60°$, and (d) $\Theta_{col} = 90°$, i.e., above the equator. The solid curves are for ST evaluations, while the sole dashed curve in each panel is for JL rates at $r = 4R_{NS}$. At lower altitudes, JL and ST cooling rates are visually indistinguishable on this scale. All curves are computed for outgoing electrons, which at the equator becomes equivalent to inwardly propagating e^-. The angular distributions for panels (b) and (c) are displayed in Figure 9.

(A color version of this figure is available in the online journal.)

that the emergent spectrum from this process can potentially extend to 1 GeV in polar emission geometries, such as is seen in some high-field *Fermi* pulsars, but perhaps only to around 1 MeV in equatorial acceleration locations. This provides an interesting context for resonant Compton upscattering models of magnetars, such as that proposed by Baring & Harding (2007): a quasi-equatorial RRLA picture at altitudes above $2–3R_{NS}$ should generate emission spectra that are not too disparate from those needed to accommodate the Comptel upper limits (e.g., Kuiper et al. 2006; den Hartog et al. 2008a, 2008b; Götz et al. 2006) at a few hundred keV to quiescent AXP and SGR hard X-ray tail emission. The detailed assessment of the viability of this picture awaits an exploration of a combined photon emission and electron cooling analysis in neutron star magnetospheres, including a foray into scenarios invoking non-dipolar field morphologies (e.g., Thompson & Beloborodov 2005). The development of time-dependent cooling of electrons for such future models will build upon the foundations laid and understanding presented in this paper.

6. CONCLUSIONS

This paper has presented a formulation for resonant Compton cooling rates of ultrarelativistic electrons in magnetars and high-field pulsars for arbitrary altitudes and colatitudes. Such electrons can be energized in the dynamic environments of these neutron stars, and their cooling rates in collisions with thermal surface X-rays has never before been explored using full QED scattering physics. We present both numerical computations and analytic asymptotic forms of electron cooling rates and reaction rates, using standard Boltzmann equation formulations in terms of the scattering differential cross section. The evaluations of the cooling rates employ, for the first time, the state-of-the-art ST spin-dependent cross section for magnetic Compton scattering. This choice affords a more physically appropriate description of spin-dependent contributions to the width of the cyclotron resonance, and generates significant corrections relative to results obtained using the older JL cross section in this context, i.e., up to factors of two in subcritical fields.

Both the numerical work and the analytic approximations will serve as useful tools for magnetic Compton upscattering model development in the future.

It is demonstrated that the cooling rates scale with field as B^2 in subcritical fields, but with a weaker dependence ($\propto B$) in supercritical field regimes, due to the Klein–Nishina and recoil effects, and an ultraquantum reduction of the cyclotron decay width. Accordingly, a principal conclusion of this paper is that older magnetic Thomson formulations will overestimate the cooling rates by orders of magnitude if extrapolated to $B \gg 1$ cases. This underpins the major motivation for employing the full QED formalism developed herein. Yet, as with previous magnetic Thomson cooling studies, it is found here that distributing the soft photons with a thermal spectral energy distribution, as is the case for surface X-ray seeds for scattering, profoundly alters the collision kinematics accessed and the resulting form of the electron cooling rates. In such cases, the resonance is always sampled above a certain Lorentz factor that is dependent on the photon temperature, the interaction altitude and colatitude for a fixed polar magnetic field. This enhances the cooling rates at Lorentz factors above 10^5 by orders of magnitude over those computed for monoenergetic soft photons. Resonant Compton cooling is demonstrated to be highly effective in cooling electrons; putative magnetospheric acceleration of electrons can be halted effectively at lower altitudes and Lorentz factors than typically occurs when using curvature radiation. Moreover, the cooling lengths are inferior to the neutron star radius for $10^3 < \gamma_e < 10^5$ when the soft photon temperature exceeds around 3×10^5 K. This renders the inner magnetospheric, closed-field region, a prime site for Compton-cooling-limited non-thermal emission in magnetars. In particular, it is found that resonant cooling is accessed at lower Lorentz factors in equatorial locales in a dipole field configuration, suggesting that such a process might generate scattered photons only up to energies of an MeV or so at high colatitudes; such a circumstance may prove quite relevant to the hard X-ray tail quiescent emission seen in magnetars.

These developments can be used in future investigations that simultaneously treat the spatial and temporal evolution of photon and electron distributions due to the resonant Compton process. Their general facility permits deployment in both kinetic equation or Monte Carlo techniques. Importing geometrical considerations and appropriate acceleration/injection of electrons in such magnetospheric studies should permit the detailed modeling of the hard X-ray tail spectra and pulse profiles in observed in AXPs and SGRs, and also be pertinent to gamma-ray emission from high-field pulsars such as PSR B1509-58.

APPENDIX A

ANALYTIC REDUCTION OF COMPTON COOLING AND COLLISION RATES IN $\gamma_e \gg 1$ DOMAINS

The expressions for the asymptotic resonant rates in supercritical fields that are summarized in Section 4 and validate the numerical computations therein, are derived in this appendix. For thermal photons of dimensionless temperature Θ, they correspond to the regime $\gamma_e \Theta \gtrsim B$. Yet, it must be noted that the core equations developed in this appendix, Equation (A14) for the JL case, and Equation (A25) for the ST formalism, are also applicable to non-resonant cases, but only under the $\gamma_e \gg 1$ ultrarelativistic presumption. Soft photon anisotropies at high altitudes and non-polar colatitudes are not encapsulated by the developments herein.

A.1. Resonant Cooling Rates: Johnson & Lippmann Formalism

The starting point is the full formulation in Equation (9). The resonant domain is realized in the $\gamma_e \gg 1$ regime, for which the Jacobian in Equation (11) receives a leading order contribution of

$$\left| \frac{\partial \varepsilon_f}{\partial(\cos\theta_f)} \right| \approx \gamma_e \beta_e \omega_f \, [1 - \Psi], \quad \Psi = \frac{(1-\mu)\,\omega_f\,(\omega_i - \omega_f\mu)}{2\omega_i - \omega_f - \zeta}. \tag{A1}$$

The correction factor Ψ is small in the limits $B \to 0$ and $B \to \infty$, but contributes approximately 30%–40% in the near-critical field regime. In addition, the relative velocity factor $1 - \beta_e \cos\theta_f$ becomes approximately $\beta_e(1 - \cos\theta_f)$. Under these approximations, for isotropy of soft photons $f(\mu_i) \to 1$ on the cone (which is relaxed in Section 5), the monoenergetic cooling rate simplifies to

$$\dot{\gamma}_e \approx -\frac{n_s c}{\mu_+ - \mu_-} \frac{1}{\gamma_e \varepsilon_s^2} \int_{\omega_-}^{\omega_+} \omega_i \, d\omega_i \int_{-1}^{1} d(\cos\theta_f)\, [1 - \cos\theta_f]\, \omega_f\, [1 - \Psi]\, \frac{d\sigma}{d(\cos\theta_f)}. \tag{A2}$$

As a reminder, here $\omega_\pm = \gamma_e \varepsilon_s (1 + \beta_e \mu_\pm)$ defines the kinematic maximum and minimum of incoming photon energies in the ERF. The dominant contribution to the ω_i integration comes from the resonance, so that the non-resonant terms in the JL cross section in Equations (13) can be neglected; it is not present in the approximate form for the ST cross section near resonance in Equation (15). The JL differential cross section becomes

$$\frac{d\sigma_{\rm JL}}{d(\cos\theta_f)} \approx \frac{3\sigma_{\rm T}}{16} \frac{\omega_f^3 \, e^{-\kappa}}{\omega_i\,[2\omega_i - \omega_f - \zeta]} \frac{\omega_f\,\mathcal{T}}{(\omega_i - B)^2 + (\Gamma/2)^2}, \quad \kappa = \frac{\omega_f^2 \sin^2\theta_f}{2B} \tag{A3}$$

for $\zeta = \omega_i \omega_f (1 - \cos\theta_f)$. The polarization-averaged factor in the numerator is taken from Equation (14):

$$\omega_f\,\mathcal{T} = 2\omega_i - (1 + \omega_i)\,\omega_f(1 - \cos\theta_f)^2. \tag{A4}$$
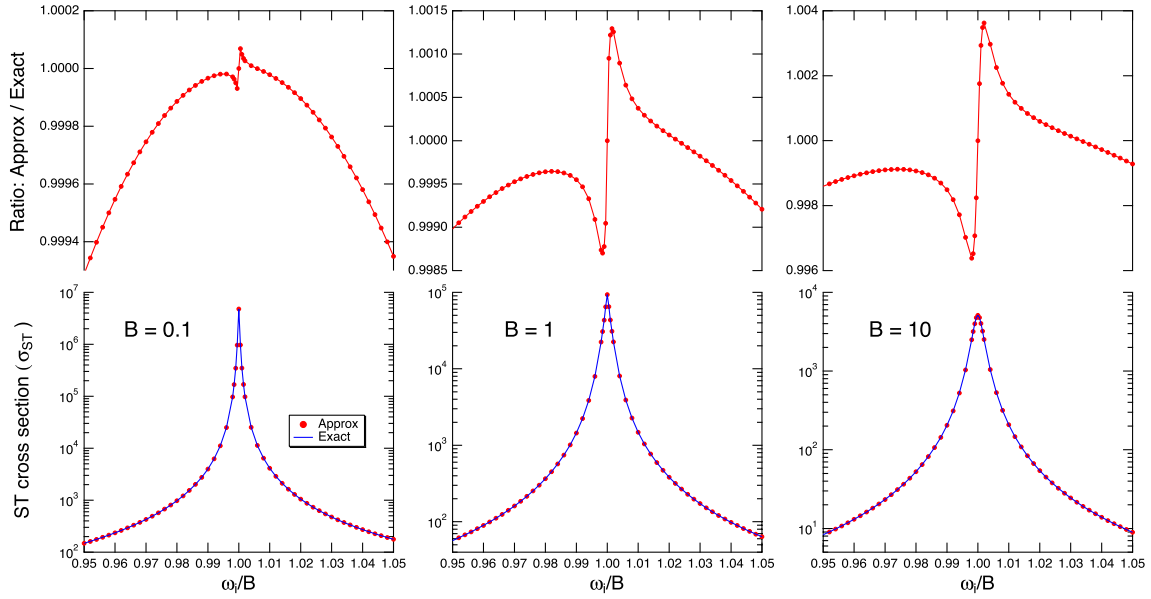
Figure 11. Total cross section for the Sokolov and Ternov (ST) QED formulation of magnetic Compton scattering, for the field strengths $B = 0.1, 1, 10$, as labeled. The panels focus on a small range $0.95 \leqslant \omega_i/B \leqslant 1.05$ centered on the cyclotron resonance. The numerical evaluation of the exact cross section derived in P. L. Gonthier et al. (2011, in preparation) is presented as the solid curves in the lower panels and includes the spin-dependent cyclotron decay widths in the resonant denominators. The approximation in Equation (A22), derived in P. L. Gonthier et al. (2011, in preparation), when integrated over θ_f produces the points on the lower panels. The ratio of the approximate cross section to the exact one is illustrated as points connected by lines in the upper three panels, clearly indicating the excellent precision of the approximation in Equation (A22) in this energy range near the peak and in the wings of the cyclotron resonance.

(A color version of this figure is available in the online journal.)

At this stage, the focus will be on analytic reduction of the JL formulation.

Using $r = 1/[1 + \omega_i(1 - \cos\theta_f)]$, a change of variables for the θ_f integration is employed, so that $d(\cos\theta_f) = -dr/(r^2\omega_i)$ with $1/(1 + 2\omega_i) \leqslant r \leqslant 1$. Therefore, the scattering kinematics is described via

$$\frac{\omega_f}{\omega_i} = \frac{2r}{1 + \sqrt{1 - q(r, \omega_i)}}, \quad q(r, \omega_i) = \frac{2}{\omega_i}(1 - r)[(2\omega_i + 1)r - 1]. \tag{A5}$$

The cooling rate reduces to

$$\dot{\gamma}_{e,\mathrm{JL}} \approx -\frac{3}{16}\frac{n_s\,\sigma_{\mathrm{T}}c}{\mu_+ - \mu_-}\frac{1}{\gamma_e\varepsilon_s^2}\int_{\omega_-}^{\omega_+}\frac{\omega_i^2\,d\omega_i}{(\omega_i - B)^2 + (\Gamma/2)^2}\int_{1/(1+2\omega_i)}^1 dr\,\frac{(1-r)}{r^3}\left(\frac{\omega_f}{\omega_i}\right)^4\frac{[1 - \Psi]\,\omega_f\mathcal{T}\,e^{-\kappa}}{2\omega_i - \omega_f - \zeta}. \tag{A6}$$

The following identities then prove useful:

$$\omega_f\sin^2\theta_f = \frac{1}{r}\{1 - \sqrt{1 - q}\},$$

$$\zeta = \frac{2\omega_i(1 - r)}{1 + \sqrt{1 - q}}, \tag{A7}$$

$$\phi = \frac{1 - \sqrt{1 - q}}{1 + \sqrt{1 - q}}.$$

Accordingly, the argument κ of the exponential is purely a function of q at the peak of the resonance and is most compactly expressed as $\kappa = \phi\omega_i/B$. It follows that $r(2\omega_i - \omega_f - \zeta) = \omega_f\sqrt{1 - q}$ and $r\omega_f\mathcal{T} = 2\omega_i r - (1 + \omega_i)[1 - \sqrt{1 - q}]$, defining two useful identities that can compactly express the last factor in Equation (A6).

The next step is to change to use ϕ as the angular integration variable, since it proves more convenient than r. For this development, the ERF incoming photon energy is expressed via the parameter

$$z_\omega = \frac{1}{2}\left(\Phi + \frac{1}{\Phi}\right) \equiv 1 + \frac{1}{\omega_i}, \quad \Phi = \frac{\sqrt{1 + 2\omega_i} - 1}{\sqrt{1 + 2\omega_i} + 1}. \tag{A8}$$

To facilitate the algebra, it proves convenient to effect the re-scaling $R = (1 + z_\omega)(1 + \phi)r$, which spawns the identities

$$\omega_i = \frac{1}{z_\omega - 1}, \quad \omega_f = \frac{R}{z_\omega^2 - 1}, \quad \mu = z_\omega - \frac{z_\omega^2 - 1}{R}(1 + \phi). \tag{A9}$$

The cooling rate can then be recast in the form

$$\dot{\gamma}_{e,\mathrm{JL}} \approx -\frac{3}{8} \frac{n_s \sigma_\mathrm{T} c}{\mu_+ - \mu_-} \frac{1}{\gamma_e \varepsilon_s^2} \int_{\mathcal{R}_-}^{\mathcal{R}_+} \frac{e^{-\phi} \, dR}{(1 + z_\omega)^3} \frac{1 + \phi}{1 - \phi} (\mathcal{R}_+ - R)\{R - z_\omega(z_\omega + 1)\phi\}[1 - \Psi], \tag{A10}$$

for $\mathcal{R}_\pm = (z_\omega \pm 1)(1 + \phi)$. We note also the identity

$$\Psi = \frac{(1 - \mu) \, r \, (\omega_i - \omega_f \mu)}{\sqrt{1 - q}} = \frac{\{\mathcal{R}_+ - R\} \{(z_\omega - 1)\mathcal{R}_+ + 1 + z_\omega - R z_\omega\}}{(1 - \phi)(1 + z_\omega)^2}. \tag{A11}$$

Since $q(r, \omega_i)$ is quadratic in r, there are two branches to the $R \to \phi$ transformation, defined by $R = R_\pm$, where

$$R_\pm = z_\omega (1 + \phi) \pm \sqrt{1 - 2\phi z_\omega + \phi^2}. \tag{A12}$$

Both branches, $\mathcal{R}_- \leqslant R_- \leqslant z_\omega(1 + \phi)$ and $z_\omega(1 + \phi) \leqslant R_+ \leqslant \mathcal{R}_+$, span the domain $0 \leqslant q \leqslant 2\omega_i/(1 + 2\omega_i)$, or equivalently, $0 \leqslant \phi \leqslant \Phi$, and for each we have

$$\left| \frac{dR}{d\phi} \right| = \frac{1 - \phi}{1 + \phi} \frac{1 + z_\omega}{\sqrt{1 - 2\phi z_\omega + \phi^2}}. \tag{A13}$$

After substantial cancellation from contributions from the two branches, the algebra routinely yields a resonant asymptotic approximation for the JL cooling rate in and near the resonance:

$$\dot{\gamma}_{e,\mathrm{JL}} \approx -\frac{3}{4} \frac{n_s \sigma_\mathrm{T} c}{\mu_+ - \mu_-} \frac{1}{\gamma_e \varepsilon_s^2} \int_{\omega_-}^{\omega_+} \frac{\mathcal{F}(z_\omega, p) - \mathcal{G}(z_\omega, p)}{(\omega_i - B)^2 + (\Gamma/2)^2} \frac{\omega_i^4 \, d\omega_i}{(1 + 2\omega_i)^2}, \quad z_\omega = 1 + \frac{1}{\omega_i}, \tag{A14}$$

for $p = \omega_i/B \approx 1$, where the leading order term in the $z_\omega \approx 1$ and $z_\omega \gg 1$ domains has the functional form

$$\mathcal{F}(z, p) = \int_0^{\Phi(z)} \frac{f(z, \phi) e^{-p \phi} \, d\phi}{\sqrt{1 - 2z\phi + \phi^2}}, \quad f(z, \phi) = z - 1 + z(3 - z)\phi - (1 + z^2) \phi^2. \tag{A15}$$

Here, $\Phi(z) = z - \sqrt{z^2 - 1}$. The correction term corresponding to the Ψ contribution is

$$\mathcal{G}(z, p) = \frac{2(z - 1)}{(1 + z)^2} \int_0^{\Phi(z)} \frac{g(z, \phi) e^{-p \phi} \, d\phi}{(1 - \phi)\sqrt{1 - 2z\phi + \phi^2}}, \tag{A16}$$

where

$$g(z, \phi) = 2z - \phi(1 - 2z + 5z^2) - \phi^2(1 - 5z + 3z^2 - 3z^3) - \phi^3(1 - 4z + z^2 - 2z^3) - \phi^4(1 + z^2). \tag{A17}$$

This separation is convenient, because it is trivial to show that $\mathcal{G}(z, p) \to 0$ in both the limits $z \to 1^+$ and $z \to \infty$. The integrals for $\mathcal{F}$ and $\mathcal{G}$ can be expressed in terms of series of special functions, an analytic path that does not facilitate computation. However, for numerical purposes, it suffices to evaluate them as series in the $(z - 1) \ll 1$ and $z \gg 1$ limits, as outlined in Appendix B below. Observe that Equation (A14) is reproduced in Equation (40).

Numerical evaluation of Equation (A14) is somewhat cumbersome and requires algorithmic intricacy and precision due to the presence of the rapidly varying Lorentz profile. Since $\Gamma/B \ll 1$ for all domains of interest in this paper, the Lorentz profile in Equation (13) can be approximated by a delta function in ω_i space of identical normalization:

$$\frac{1}{(\omega_i - B)^2 + (\Gamma/2)^2} \to \frac{2\pi}{\Gamma} \delta(\omega_i - B). \tag{A18}$$

This standard mapping was adopted in Dermer (1990, for the specific non-relativistic cyclotron decay case of $\Gamma = 4\alpha_\mathrm{f} B^2/3$) and Baring & Harding (2007) and renders the ω_i integration trivial. Accordingly, one integral is removed from the computation, the integral that offers the greatest potential for numerical imprecision. The result of this manipulation is

$$\dot{\gamma}_{e,\mathrm{JL}} \approx -\frac{3\pi}{2} \frac{n_s \sigma_\mathrm{T} c}{\mu_+ - \mu_-} \frac{B^2}{\gamma_e \varepsilon_s^2 \Gamma} \frac{\mathcal{F}(z) - \mathcal{G}(z)}{(1 + z)^2}, \quad z = 1 + \frac{1}{B}, \tag{A19}$$

with the functional identification $\mathcal{F}(z) \equiv \mathcal{F}(z, 1)$, $\mathcal{G}(z) \equiv \mathcal{G}(z, 1)$ representing the $p = \omega_i/B = 1$ specialization. In the high-field limit, $B \gg 1$, which is obtained via setting $z \to 1$, we have $\mathcal{G}(z) \to 0$ and the integrand in Equation (A15) possesses no divergence as $\phi \to \Phi \to 1$. Then $\mathcal{F} \to 2(1 - 2/e)$, giving

$$\dot{\gamma}_{e,\mathrm{JL}} \approx -\frac{n_s \sigma_\mathrm{T} c}{\mu_+ - \mu_-} \frac{3\pi B^2}{4\gamma_e \varepsilon_s^2 \Gamma} \left(1 - \frac{2}{e}\right), \quad B \gg 1. \tag{A20}$$

Likewise, for $B \ll 1$, $z \gg 1$, and $\Phi \approx 1/(2z)$, yielding $\mathcal{G} \to 0$ and $\mathcal{F} \to 2/3$, and the magnetic Thomson limit result becomes

$$\dot{\gamma}_{e,\mathrm{JL}} \approx -\frac{n_s \sigma_\mathrm{T} c}{\mu_+ - \mu_-} \frac{\pi B^4}{\gamma_e \varepsilon_s^2 \Gamma}, \quad B \ll 1. \tag{A21}$$

When substituting $\Gamma \to 4\alpha_f B^2/3$ for the "non-relativistic" cyclotron decay width, this result generates Equation (31) and is commensurate with the leading order, high-γ_e contribution from Equation (24) of Dermer (1990), specifically for monoenergetic soft photons. We note in concluding this reduction of the JL resonant formalism that Equations (A14) and (A19) can be routinely integrated over a Planck spectrum for soft photons to yield a separable temperature factor contributing to the thermal, resonant cooling rate; this aspect is outlined in Section 4.2.

A.2. Resonant Cooling Rates: Sokolov & Ternov Formulation

For ST states, the analytic manipulations proceed using an almost identical protocol. Equation (A3) is replaced by the spin-dependent form for the approximate differential cross section at and near resonance:

$$\frac{d\sigma_{ST}}{d(\cos\theta_f)} = \frac{3\sigma_T}{64} \frac{\omega_f^2 \, e^{-\kappa}}{\omega_i \left[2\omega_i - \omega_f - \zeta\right] \varepsilon_\perp^3} \sum_{s=\pm1} \frac{(\varepsilon_\perp + s)^2 \, \Lambda_s}{(\omega_i - B)^2 + (\Gamma_s/2)^2}, \tag{A22}$$

for $\kappa = \omega_f^2 \sin^2\theta_f / [2B]$ and

$$\Lambda_s = (2\varepsilon_\perp - s) \, \omega_f^2 \mathcal{T} + s \, \varepsilon_\perp^2 \, (\omega_i - \omega_f). \tag{A23}$$

Here, the quantum number s labels the intermediate electron's spin state, yielding the two Lorentz profiles that are described by the widths

$$\Gamma_s = (\varepsilon_\perp + s) \frac{1 + B}{\varepsilon_\perp} \, \Gamma, \quad \varepsilon_\perp = \sqrt{1 + 2B}. \tag{A24}$$

Again, Γ is the same spin-averaged cyclotron width/decay rate as is used in the JL formulation. Before proceeding with the analytic manipulations, a brief description of the origin of the approximation in Equation (A22) is offered. A full derivation, too lengthy to include here, is presented in P. L. Gonthier et al. (2011, in preparation), a paper on the physics of magnetic Compton scattering focusing on the use of ST electron spin states. The starting point for that work is Equation (3.25) of Sina (1996), with the S-matrix elements in the ST formulation being encapsulated in Equations (3.15) and (3.16) of Sina's (1996) thesis. P. L. Gonthier et al. (2011, in preparation) specialized this formal result to the case of incoming photons propagating along **B** and developed and simplified the algebra for the differential cross section. Near the resonance, the approximation $\omega_i \approx B$ was invoked, for efficacy, to condense the numerators of the squares of the S-matrix elements. The result was Equation (A22). A numerical illustration of the total cross section for the ST formulation is presented in Figure 11, exhibiting both the exact cross section (curves) and the integration over θ_f of the approximation in Equation (A22) in the bottom panels (as points). The upper panels in the figure highlight the ratio of the approximation to the exact computation and clearly demonstrate that the approximation is accurate to a fraction of a percent for the fields $B = 0.1, 1, 10$.

Now, in terms of the development algebra, the $\omega_f^2 \mathcal{T}$ piece has already been handled in the JL resonance asymptotics, yielding an integral involving the $\mathcal{F}(z_\omega, \, p) - \mathcal{G}(z_\omega, \, p)$ factor. The remaining piece possesses an integrand proportional to $\omega_i - \omega_f$ and can be manipulated in a similar fashion through the changes of variables $\theta_f \to \phi$, amounting to a replacement of the factor $R - z_\omega(z_\omega + 1)\phi$ in Equation (A10) by one proportional to $(1 + \phi)(R - z - 1)$. This algebraic rearrangement is routine. Progress can be expedited by extracting out the $\mathcal{F} - \mathcal{G}$ piece that reproduces half the JL result, i.e., provides the dominant contribution to the $B \ll 1$ limit. The end result for the ST cooling rate in and near the resonance can be cast in the form, summarized in Equation (43),

$$\dot{\gamma}_{e,ST} \approx -\frac{3}{16} \frac{n_s \sigma_T c}{\mu_+ - \mu_-} \frac{1}{\gamma_e \varepsilon_s^2} \sum_{s=\pm1} \int_{\omega_-}^{\omega_+} \frac{(s\varepsilon_\perp + 1) \, \Upsilon_s (z_\omega, \, p)}{(\omega_i - B)^2 + (\Gamma_s/2)^2} \frac{\omega_i^4 \, d\omega_i}{(1 + 2\omega_i)^2}, \quad z_\omega = 1 + \frac{1}{\omega_i}, \tag{A25}$$

for $p = \omega_i/B \approx 1$, and

$$\Upsilon_s (z, \, p) = \left\{ \left(\frac{s}{\varepsilon_\perp} + 1\right) [\mathcal{F}(z, \, p) - \mathcal{G}(z, p)] + \left(\frac{s}{\varepsilon_\perp} - 1\right) [\mathcal{F}_\Delta(z, \, p) - \mathcal{G}_\Delta(z, p)] \right\}. \tag{A26}$$

This path of manipulation leads to the identification of two new integral functions:

$$\mathcal{F}_\Delta(z, \, p) = (z + 1) \int_0^{\Phi(z)} \frac{\phi(1 - \phi) e^{-p\phi}}{\sqrt{1 - 2z\phi + \phi^2}} \, d\phi$$

$$\mathcal{G}_\Delta(z, \, p) = 2 \frac{z - 1}{z + 1} \int_0^{\Phi(z)} \frac{\phi^2 (z + 2\phi z - \phi^2) e^{-p\phi}}{(1 - \phi)\sqrt{1 - 2z\phi + \phi^2}} \, d\phi. \tag{A27}$$

The incorporation of spin dependence necessitates a total of two integrals expressing the angular integrations, which in this paper are each divided into differences of terms ($\mathcal{F} - \mathcal{G}$ and $\mathcal{F}_\Delta - \mathcal{G}_\Delta$) that isolate the mathematical character of the contributions to the Jacobian in Equation (A1). As with the JL resonant analytics above, for numerical purposes, it suffices to evaluate each of these four functions as series in the $(z - 1) \ll 1$ and $z \gg 1$ limits, a development outlined below.

Again, one may form a more compact analytic approximation to the resonant ST contribution by appealing to the fact that $\Gamma/B \ll 1$ for all domains of interest in this paper. The Lorentz profile in Equation (13) is then again approximated by a delta function in ω_i

space via Equation (A18). Then the $p \to 1$ limit can be taken, the ω_i integration is trivial, and the two-dimensional integral in Equation (A25) reduces to

$$\dot{\gamma}_{e,\mathrm{ST}} \approx -\frac{3\pi}{4} \frac{n_s \, \sigma_\mathrm{T} c}{\mu_+ - \mu_-} \frac{1}{\gamma_e \varepsilon_s^2 \Gamma} \frac{B^2}{(1+z)^2} \{ [\mathcal{F}(z) - \mathcal{G}(z)] + [\mathcal{F}_\Delta(z) - \mathcal{G}_\Delta(z)] \}, \quad z = 1 + \frac{1}{B}, \tag{A28}$$

again with the functional identification $\mathcal{F}(z) \equiv \mathcal{F}(z, 1)$, $\mathcal{G}(z) \equiv \mathcal{G}(z, 1)$, etc., representing the $p = \omega_i/B = 1$ specialization. Observe that the magnetic field-dependent factors here are just represented by the $\mathcal{R}_\mathrm{ST}(B)$ function defined in Equation (51). Observe also that Equation (A28) can be derived in an alternative fashion by asserting the Equation (A18) correspondence early on, and then following the same changes of variables for the angular integration. This amounts to employing the spin-averaged ST differential cross section

$$\frac{d\sigma_\mathrm{ST}}{d(\cos\theta_f)} \approx \frac{3\pi\sigma_\mathrm{T}}{16\Gamma} \frac{\omega_f^2 \, e^{-\kappa} \, \delta(\omega_i - B) \, \mathcal{S}}{\omega_i \, (1 + \omega_i) \, [2\omega_i - \omega_f - \zeta]} \,, \tag{A29}$$

for

$$\mathcal{S} = \frac{1}{2\varepsilon_\perp^2} \sum_{s=\pm 1} (\varepsilon_\perp + s) \, \Lambda_s = \left(2 - \frac{1}{\varepsilon_\perp^2} \right) \omega_f^2 \mathcal{T} + (\omega_i - \omega_f). \tag{A30}$$

This is slightly more involved than the corresponding JL form, which is obtained by substituting $\mathcal{S} \to 2(1 + B)\omega_f^2 \mathcal{T}$. Note that an identical alternative protocol for derivation applies to the JL resonant asymptotic result in Equation (A19).

The high-field limit of the ST resonant rate is readily obtained. Setting $z \to 1$, we have $\mathcal{F}(z) \to 2(1 - 2/e)$, as before, and $\mathcal{F}_\Delta \to 2(1 - 2/e)$ also. The $\mathcal{G}(z)$ and $\mathcal{G}_\Delta(z)$ terms contribute zero in this limit, yielding

$$\dot{\gamma}_{e,\mathrm{ST}} \approx -\frac{n_s \, \sigma_\mathrm{T} c}{\mu_+ - \mu_-} \frac{3\pi B^2}{4\gamma_e \varepsilon_s^2 \Gamma} \left(1 - \frac{2}{e} \right), \quad B \gg 1, \tag{A31}$$

a result identical to that in Equation (A20) for the JL cross-section formalism. In the $B \ll 1$ limit, since $z \gg 1$ and $\Phi \approx 1/(2z)$, again the $\mathcal{G}(z)$ and $\mathcal{G}_\Delta(z)$ terms can be neglected, indicating that the $\omega_i - \omega_f$ term is of order $O(1/z)$. Similarly, the $\mathcal{F}_\Delta(z)$ contribution is small. Then, since $\mathcal{F}(z) \to 2/3$ when $z \to \infty$, the Thomson limit result is

$$\dot{\gamma}_{e,\mathrm{ST}} \approx -\frac{n_s \, \sigma_\mathrm{T} c}{\mu_+ - \mu_-} \frac{\pi B^4}{2\gamma_e \varepsilon_s^2 \Gamma}, \quad B \ll 1, \tag{A32}$$

i.e., half that of the JL value in Equation (A21).

A.3. Compton Upscattering Collisional Rates

Now the focus turns to *collision rates*, i.e., inverse lifetimes for Compton upscattering collisions that are employed in the computation of mean energy losses for the electrons that are considered in Section 4.3. These are mathematically very similar to the cooling rates, being just devoid of an energy factor $\varepsilon_f - \varepsilon_i \approx \varepsilon_f$ in the integrand. Accordingly, the reaction rate can quickly be written down by introducing a factor $-1/\varepsilon_f = -(1 + z_\omega)/\gamma_e/(\mathcal{R}_+ - R)$ into Equation (A10) for the JL case. This reduces the order of the polynomial factors in the integrand by one. The manipulations then parallel those for the cooling rates, and the end result is of a very similar form. For JL states, one arrives at

$$\frac{1}{\tau_{e,\mathrm{JL}}} \approx \frac{3}{4} \frac{n_s \, \sigma_\mathrm{T} c}{\mu_+ - \mu_-} \frac{1}{\gamma_e^2 \varepsilon_s^2} \int_{\omega_-}^{\omega_+} \frac{\mathcal{F}_\tau (z_\omega, \, p) - \mathcal{G}_\tau (z_\omega, \, p)}{(\omega_i - B)^2 + (\Gamma/2)^2} \frac{\omega_i^3 \, d\omega_i}{1 + 2\omega_i}, \quad z_\omega = 1 + \frac{1}{\omega_i}, \tag{A33}$$

where again, $p = \omega_i/B$. Now we have two new functions expressing the integrals over photon scattering angles in the ERF:

$$\mathcal{F}_\tau (z, \, p) = \int_0^{\Phi(z)} \frac{f_\tau(z, \, \phi) \, e^{-p\phi} \, d\phi}{\sqrt{1 - 2z\phi + \phi^2}}, \quad f_\tau(z, \, \phi) = z(1 - z\phi), \tag{A34}$$

where again, $\Phi(z) = z - \sqrt{z^2 - 1}$. The correction term corresponding to the Ψ contribution is

$$\mathcal{G}_\tau (z, \, p) = \frac{z - 1}{(1 + z)^2} \int_0^{\Phi(z)} \frac{g_\tau(z, \, \phi) \, e^{-p\phi} \, d\phi}{(1 - \phi)\sqrt{1 - 2z\phi + \phi^2}}, \tag{A35}$$

with

$$g_\tau(z, \, \phi) = 2z - \phi(1 - z + 4z^2) + \phi^2 z(5 + z + 2z^2) - \phi^3(1 + z^2). \tag{A36}$$

This separation yields a dominance of $\mathcal{F}_\tau$ in both the limits $z \to 1^+$ and $z \to \infty$, for which it is trivial to show that $\mathcal{G}_\tau(z, \, p) \to 0$. The reduction proceeds along similar lines for the ST states, resulting in

$$\frac{1}{\tau_{e,\mathrm{ST}}} \approx \frac{3}{16} \frac{n_s \, \sigma_\mathrm{T} c}{\mu_+ - \mu_-} \frac{1}{\gamma_e^2 \varepsilon_s^2} \sum_{s=\pm 1} \int_{\omega_-}^{\omega_+} \frac{(s\varepsilon_\perp + 1) \, \Upsilon_s^\tau (z_\omega, \, p)}{(\omega_i - B)^2 + (\Gamma_s/2)^2} \frac{\omega_i^3 \, d\omega_i}{1 + 2\omega_i}, \quad z_\omega = 1 + \frac{1}{\omega_i}, \tag{A37}$$

for $p = \omega_i / B \approx 1$ and

$$\Upsilon_s^\tau (z,\, p) = \left\{ \left(\frac{s}{\varepsilon_\perp} + 1 \right) [\mathcal{F}_\tau(z,\, p) - \mathcal{G}_\tau(z,\, p)] + \left(\frac{s}{\varepsilon_\perp} - 1 \right) [\mathcal{F}_{\tau\Delta}(z,\, p) - \mathcal{G}_{\tau\Delta}(z,\, p)] \right\}. \tag{A38}$$

This arrangement seeds the identification of two new integral functions:

$$\mathcal{F}_{\tau\Delta}(z,\, p) = \int_0^{\Phi(z)} \frac{(1 - z\phi)\, e^{-p\phi}}{\sqrt{1 - 2z\phi + \phi^2}}\, d\phi$$
$$\mathcal{G}_{\tau\Delta}(z,\, p) = \frac{z-1}{z+1} \int_0^{\Phi(z)} \frac{\phi^2(1 + 2z - \phi)\, e^{-p\phi}}{(1 - \phi)\sqrt{1 - 2z\phi + \phi^2}}\, d\phi. \tag{A39}$$

Analytics and evaluation of these functions are addressed in Appendix B.

As with the cooling rates, it is possible to form more compact analytic approximations to the resonant contributions by invoking the delta function in ω_i space to the Lorentz profile via Equation (A18), since $\Gamma/B \ll 1$ for all fields. Then the $p \to 1$ limit can be taken, the ω_i integrations are trivial, and the two-dimensional integral in Equation (A33) collapses to

$$\frac{1}{\tau_{e,\mathrm{JL}}} \approx \frac{3\pi}{2} \frac{n_s \sigma_\mathrm{T} c}{\mu_+ - \mu_-} \frac{B^2}{\gamma_e^2 \varepsilon_s^2 \Gamma} \frac{\mathcal{F}_\tau(z) - \mathcal{G}_\tau(z)}{1 + z}, \quad z = 1 + \frac{1}{B}, \tag{A40}$$

and likewise for the ST form in Equation (A37):

$$\frac{1}{\tau_{e,\mathrm{ST}}} \approx \frac{3\pi}{4} \frac{n_s \sigma_\mathrm{T} c}{\mu_+ - \mu_-} \frac{1}{\gamma_e^2 \varepsilon_s^2 \Gamma} \frac{B^2}{1 + z} \{[\mathcal{F}_\tau(z) - \mathcal{G}_\tau(z)] + [\mathcal{F}_{\tau\Delta}(z) - \mathcal{G}_{\tau\Delta}(z)]\}. \tag{A41}$$

Using the fact that $\mathcal{F}_\tau \to 2/3$ as $z \to \infty$ yields the dominant contribution for $B \ll 1$, and $\mathcal{F}_\tau \to 1 - 1/e$ and $\mathcal{F}_{\tau\Delta} \to 1 - 1/e$ as $z \to 1^+$ dominate the $B \gg 1$ case, one arrives at the asymptotic forms

$$\frac{1}{\tau_{e,\mathrm{JL}}} \approx \frac{n_s \sigma_\mathrm{T} c}{\mu_+ - \mu_-} \frac{\pi B^2}{\gamma_e^2 \varepsilon_s^2 \Gamma} \begin{cases} B, & B \ll 1, \\ \frac{3}{4}\left(1 - \frac{1}{e}\right), & B \gg 1, \end{cases} \tag{A42}$$

and

$$\frac{1}{\tau_{e,\mathrm{ST}}} \approx \frac{n_s \sigma_\mathrm{T} c}{\mu_+ - \mu_-} \frac{\pi B^2}{\gamma_e^2 \varepsilon_s^2 \Gamma} \begin{cases} \frac{B}{2}, & B \ll 1, \\ \frac{3}{4}\left(1 - \frac{1}{e}\right), & B \gg 1. \end{cases} \tag{A43}$$

As with the cooling rates, the collision rates for the JL and ST formulations differ by a factor of two in the highly subcritical field limit, but are identical in ultraquantum domains, $B \gg 1$, as expected. Combining these properties automatically gives a fractional mean energy loss per collision that is independent of the cross section employed in both the $B \ll 1$ and $B \gg 1$ limits.

In the non-resonant regime, either Equation (A33) or Equation (A37) can be used to derive the asymptotic collision rate appropriate to $\omega_+ \ll B$ cases. Remembering that they are both posited in the $\gamma_e \gg 1$ approximation, an extra factor of $1/\beta_e$ must be reintroduced to capture the more general nature of the integral over Equation (6). Considering the JL formulation, as $z_\omega \to \infty$ the $\mathcal{G}_\tau$ term becomes insignificant, and $\mathcal{F}_\tau \to 2/3$, resulting in an integrand that is proportional to ω_i^3 / B^2. This formally includes only the resonant term; the non-resonant term in the cross section contributes an identical value in this limit (deducible, for example, from the presentation in Section 3), so that a factor of two is introduced. The integral over ω_i is then trivial, producing a dependence $1/\tau_e \propto \varepsilon_s^2$. This can then be routinely integrated over the Planck spectrum in Equation (39) to assemble the limiting non-resonant result

$$\frac{1}{\tau_e} \approx \frac{6\zeta(5)\Omega_s}{\pi^2} \frac{\sigma_\mathrm{T} c}{\lambda^3} \frac{\gamma_e^2}{\beta_e} \frac{\Theta^5}{B^2} \{(1 + \beta_e \mu_+)^4 - (1 + \beta_e \mu_-)^4\}, \quad \gamma_e \Theta(1 + \beta_e \mu_+) \ll B. \tag{A44}$$

The subscripts JL and ST are suppressed because this form applies to either formalism. Generating a rate proportional to γ_e^2 is naturally expected given that the cross section in the ERF scales as ω_i^2, with $\omega_i \propto \gamma_e$.

APPENDIX B

EVALUATION OF THE ANGULAR INTEGRALS

The cooling and collisional rates developed in Appendix A subsume the angular integration into a set of relatively compact integrals. This appendix hones these integrals by expressing them in terms of four key integrals that are chosen to afford stability of numerical evaluation. Specifically, the $z \approx 1$ range can be problematic in some of the integrals due to singularities in the integrands. The first step is to isolate identities for the more numerically pernicious integrals in terms of the more benign ones. Consider first

$\mathcal{F}(z, p)$ and $\mathcal{F}_\Delta(z, p)$. Both are fairly routine to compute in the $z \to 1^+$ limit since the singularity at $\phi = \Phi \approx 1$ in the denominator is negated by an emerging root in the numerator. Define a class of integrals

$$\mathcal{I}_\nu(z, p) = \int_0^{\Phi(z)} e^{-p\phi}(1 - 2z\phi + \phi^2)^{\nu/2} \, d\phi. \tag{B1}$$

Then rearrangement of the quadratic factor in the numerator of the integrands can be employed to establish the identity

$$\mathcal{F}(z, p) = z \mathcal{F}_\Delta(z, p) + (z - 1) \mathcal{I}_1(z, p). \tag{B2}$$

All three of these integrals are particularly stable to numerical integration, and we opt to use $\mathcal{F}_\Delta$ and $\mathcal{I}_1$ as a basis for the determination of the JL and ST rates.

The integrals $\mathcal{G}(z, p)$ and $\mathcal{G}_\Delta(z, p)$ are more pathological around $z \approx 1$, and since $\mathcal{G}_\Delta(z, p)$ possess a more compact integrand, we seek a relation between the two functions. In analogy with the $\mathcal{F}(z, p)$ case, we define another class of integrals

$$\mathcal{J}_\nu(z, p) = \int_0^{\Phi(z)} \frac{e^{-p\phi}}{1 - \phi} (1 - 2z\phi + \phi^2)^{\nu/2} \, d\phi, \tag{B3}$$

which are introduced because the integral for $\mathcal{G}$ cannot be expressed simply in terms of the $\mathcal{I}_\nu$ functions. The integrand for $\mathcal{G}$ can be efficaciously simplified using the identification of a class of polynomials that result from useful perfect derivatives:

$$p_k(z, \phi) = e^{p\phi}\sqrt{1 - 2z\phi + \phi^2} \, \frac{d}{d\phi}\{\phi^k e^{-p\phi}\sqrt{1 - 2z\phi + \phi^2}\}. \tag{B4}$$

Because $1 - 2z\Phi + \Phi^2 = 0$, these readily generate the following useful integral identities:

$$\int_0^\Phi \frac{e^{-\phi} p_0(z, \phi)}{\sqrt{1 - 2z\phi + \phi^2}} \, d\phi = -1, \quad \int_0^\Phi \frac{e^{-\phi} p_n(z, \phi)}{\sqrt{1 - 2z\phi + \phi^2}} \, d\phi = 0 \quad \text{for} \quad n \geqslant 1. \tag{B5}$$

These are used to reduce the order of the polynomial $g(z, \phi)$ in Equation (A17). The same can be done for the quartic in the numerator of $\mathcal{G}_\Delta(z, p)$. This process incurs an increase in the polynomial order in the parameter z. Rather than solve each explicitly, which effectively incorporates $\mathcal{I}_{-1}$ terms, it is expedient to form a linear combination of $\mathcal{G}$, $\mathcal{G}_\Delta$, $\mathcal{J}_1$, and $\mathcal{I}_1$ and solve for the coefficients as a linear algebra problem, demanding identity in all powers of ϕ. The result is quickly obtained:

$$\begin{aligned}
[2 + p + 2(p - 1)z](z + 1)^2 \mathcal{G}(z, p) &= [2 + (p - 2)z + (3p + 2)z^2 + 2(p - 1)z^3](z + 1)\mathcal{G}_\Delta(z, p) \\
&\quad + 2(z - 1)[-3 - 2p + (p + 10)z + 9(p - 1)z^2 - 2(p - 1)z^3]\mathcal{J}_1(z) \\
&\quad - 2(z - 1)^2[4 + 3p + 3pz - 2(p - 1)z^2]\mathcal{I}_1(z) + 2(z - 1)^2.
\end{aligned} \tag{B6}$$

Through this relation and Equation (B2), we can express the cooling rates in terms of the basis integrals $\mathcal{F}_\Delta$, $\mathcal{G}_\Delta$, $\mathcal{J}_1$, and $\mathcal{I}_1$, and these four functions form the anchors of our numerical evaluations. The same protocol can be adopted for the collisional rates so that no new functions need to be computed. The relevant identities are

$$\begin{aligned}
(1 + 2z)\mathcal{F}_\tau(z, p) = z(1 + 2z)\mathcal{F}_{\tau\Delta}(z, p) &= z\{1 + \mathcal{F}_\Delta + (1 - p + z)\mathcal{I}_1\} \\
(1 + 2z)(1 + z)^2 \mathcal{G}_\tau(z, p) = z(z + 1)(1 + \mathcal{F}_\Delta) &- (1 + 2z)\{z[z(z - 2) + 4] - 1\}\mathcal{J}_1 \\
&- [1 + z(p + (-3 + p)z - 2z^3)]\mathcal{I}_1 \\
(1 + z)(1 + 2z)\mathcal{G}_{\tau\Delta}(z, p) &= 1 + \mathcal{F}_\Delta + (2z^2 - p)\mathcal{I}_1 - z(2z + 1)\mathcal{J}_1.
\end{aligned} \tag{B7}$$

These suffice to evaluate the reaction rates in Equations (A33) and (A37) in terms of the same four basis integrals. It should be remarked that $\mathcal{G}_\Delta$ is not more stable, numerically, in the neighborhood of $z = 1$ than $\mathcal{G}$, $\mathcal{G}_\tau$, or $\mathcal{G}_{\tau\Delta}$; it is preferred only because it is analytically more compact.

The procedure with evaluating all four integrals is to change variables to $x = 1 - \phi/\Phi$ and then form a Taylor series expansion of the exponential in the integrand in terms of the parameter $p\Phi$. The result is a convergent series, rapidly so in the limit of $p\Phi \ll 1$, and collectively, or term-by-term, each of the integrals assumes a form expressible in terms of elementary functions:

$$\left(A + B \arctan(\sqrt{\Phi}) + C \log_e\left[\frac{1 + \Phi}{1 - \Phi}\right]\right) e^{-p\Phi}, \tag{B8}$$

where A, B, and C are functions of p and $\Phi(z)$. The B terms are zero for the $\mathcal{F}_\Delta$ and $\mathcal{I}_1$ integrals. This method is computationally faster than a full numerical evaluation of the integrals, which slows down when tailoring the algorithm to achieve suitable precision near $z \approx 1$. Using the notation $q = (1 - \Phi^2)/\Phi^2$, we start with $\mathcal{I}_1$, and manipulate it as follows:

$$\mathcal{I}_1(z, p) \equiv \Phi^2 e^{-p\Phi}\int_0^1 e^{p\Phi x}\sqrt{x(x + q)} \, dx = e^{-p\Phi}\sum_{n=0}^\infty \frac{(p\Phi)^n}{n!} \, i_n, \tag{B9}$$

27

for series coefficients

$$i_n = \Phi^2 \int_0^1 x^{n+1/2} \sqrt{x+q}\, dx \qquad (B10)$$

that can be expressed as special cases of the standard hypergeometric function using identity 3.197.8 of Gradshteyn & Ryzhik (1980). For integer n, i_n are analytically tractable in terms of elementary functions, and the result can be expressed as a recurrence relation that is readily obtained by an integration by parts technique:

$$i_n = \frac{1}{2+n}\left[\frac{1}{\Phi} - \frac{1-\Phi^2}{\Phi^2}\left(n+\frac{1}{2}\right)i_{n-1}\right], \quad i_0 = \frac{1+\Phi^2}{4\Phi} - \frac{(1-\Phi^2)^2}{8\Phi^2}\log_e\left[\frac{1+\Phi}{1-\Phi}\right]. \qquad (B11)$$

In this way, retaining up to the $n = 3$ term of the series in Equation (B9) generated an analytic approximation, which, at $p = 1$, is accurate to $<0.85\%$ for $z \geqslant 1$. We also observe that $\mathcal{I}_1$ can be expressed as a series of Legendre functions of the second kind, $Q_\nu(z)$, in a manner similar to that in Equation (21), but that this offers no advantage of increased computational facility.

The $\mathcal{J}_1$ integral is treated in a similar fashion and includes terms with the arctan form. The same change of variables yields

$$\mathcal{J}_1(z, p) \equiv \Phi^2 e^{-p\Phi} \int_0^1 e^{p\Phi x} \frac{\sqrt{x(x+q)}}{1-\Phi+\Phi x}\, dx = e^{-p\Phi}\sum_{n=0}^\infty \frac{(p\Phi)^n}{n!}\, j_n, \qquad (B12)$$

where the series coefficients are

$$j_n = \Phi^2 \int_0^1 \frac{x^{n+1/2}\sqrt{x+q}}{1-\Phi+\Phi x}\, dx. \qquad (B13)$$

A partial fractions manipulation of the denominator in the integrand then quickly yields a recurrence relation for the j_n:

$$j_n = \frac{1}{\Phi}i_{n-1} - \frac{1-\Phi}{\Phi}j_{n-1}, \quad j_0 = 1 - \frac{2(1-\Phi)}{\sqrt{\Phi}}\arctan\sqrt{\Phi} + \frac{(1-\Phi)^2}{2\Phi}\log_e\left[\frac{1+\Phi}{1-\Phi}\right]. \qquad (B14)$$

Truncating the series in Equation (B12) at three terms is sufficient for the purposes of this paper: at $p = 1$, this is accurate to $<0.6\%$ for $z \geqslant 1$.

The $\mathcal{F}_\Delta$ integral is handled similarly. The presence of more powers of ϕ in the numerator of the integrand lengthens the algebra somewhat, but the manipulations involve partial fractions and integration by parts. In this way, one arrives at

$$\mathcal{F}_\Delta(z, p) \equiv \frac{(1+\Phi)^2}{2} e^{-p\Phi} \int_0^1 e^{p\Phi x}(1-x)\frac{1-\Phi+\Phi x}{\sqrt{x(x+q)}}\, dx = e^{-p\Phi}\sum_{n=0}^\infty \frac{(p\Phi)^n}{n!}\, f_n, \qquad (B15)$$

where the series coefficients are

$$f_n = \frac{(1+\Phi)^2}{2}\int_0^1 x^{n-1/2}(1-x)\frac{1-\Phi+\Phi x}{\sqrt{(x+q)}}\, dx$$
$$= \frac{3+4n(2+n)-(1+2n)\Phi(1-\Phi)-3\Phi^3}{2(2n+1)\,\Phi(1-\Phi)}i_n - \frac{2n+1-\Phi}{(2n+1)(1-\Phi)}, \qquad (B16)$$

thereby making use of the i_n recurrence relation. Accordingly, the $\mathcal{F}_\Delta$ integral exhibits the same elementary function structure as the $\mathcal{I}_1$ integral. Truncating the series at $n = 3$ generates, at $p = 1$, an accuracy of $<0.25\%$ for $z \geqslant 1$.

Finally, the $\mathcal{G}_\Delta$ integral can be expressed as

$$\mathcal{G}_\Delta(z, p) \equiv \frac{\Phi(1-\Phi)^2}{(1+\Phi)^2} e^{-p\Phi} \int_0^1 e^{p\Phi x}\frac{(1-x)^2(1+\Phi^2+2(1-x)\Phi+2(1-x)x\Phi^3)}{(1-\Phi+\Phi x)\sqrt{x(x+q)}}\, dx$$
$$= e^{-p\Phi}\sum_{n=0}^\infty \frac{(p\Phi)^n}{n!}\, g_n, \qquad (B17)$$

with

$$g_n = \frac{\Phi(1-\Phi)^2}{(1+\Phi)^2}\int_0^1 x^{n-1/2}\frac{(1-x)^2(1+\Phi^2+2(1-x)\Phi+2(1-x)x\Phi^3)}{(1-\Phi+\Phi x)\sqrt{(x+q)}}\, dx. \qquad (B18)$$

If we define

$$l_n = \frac{\Phi(1-\Phi)^2}{(1+\Phi)^2}\int_0^1 \frac{x^{n-1/2}}{(1-\Phi+\Phi x)\sqrt{(x+q)}}\, dx, \qquad (B19)$$

then

$$g_n = (1+\Phi)^2 l_n + 2(\Phi^3-\Phi^2-3\Phi-1)l_{n+1} + (1+6\Phi+\Phi^2-6\Phi^3)l_{n+2} + 2\Phi(3\Phi^2-1)l_{n+3} - 2\Phi^3 l_{n+4} \qquad (B20)$$

with a recurrence relation for the l_n in terms of the j_n and the i_n:

$$l_n = \frac{\Phi(1-\Phi)}{(1+\Phi)^2}\left\{ j_{n-1} - \frac{2(n+1)\Phi}{1-\Phi^2} i_{n-1} + \frac{2\Phi^2}{1-\Phi^2} \right\}, \quad l_0 = \frac{2(1-\Phi)\Phi^{3/2}}{(1+\Phi)^2} \arctan\sqrt{\Phi}. \tag{B21}$$

The result is, for $p \approx 1$, that retaining terms to second order in p gives an approximation for $\mathcal{G}_\Delta$ that is accurate to $<0.1\%$ for all $z \geqslant 1$.

REFERENCES

Abdo, A. A., et al. (*Fermi*-LAT Collaboration) 2010, ApJ, 725, L73
Abramowitz, M., & Stegun, I. A. 1965, Handbook of Mathematical Functions (New York: Dover)
Baring, M. G. 1994, in AIP Conf. Proc. 307, Gamma-Ray Bursts, ed. G. Fishman, K. Hurley, & J. J. Brainerd (Melville, NY: AIP), 572
Baring, M. G., Gonthier, P. L., & Harding, A. K. 2005, ApJ, 630, 430
Baring, M. G., & Harding, A. K. 2007, Astrophys. Space Sci., 308, 109
Becker, W., & Trümper, J. 1997, A&A, 326, 682
Bekefi, G. 1966, Radiation Processes in Plasmas (New York: Wiley)
Blumenthal, G. R., & Gould, R. J. 1970, Rev. Mod. Phys., 42, 237
Bulik, T., & Miller, M. C. 1997, MNRAS, 288, 596
Burwitz, V., Haberl, F., Neuhäuser, R., Predehl, P., Trümper, J., & Zavlin, V. E. 2003, A&A, 399, 1109
Bussard, R. W., Alexander, S. B., & Mészáros, P. 1986, Phys. Rev. D, 34, 440
Camilo, F., Ransom, S. M., Halpern, J. P., Reynolds, J., Helfand, D. J., Zimmerman, N., & Sarkissian, J. 2006, Nature, 442, 892
Canuto, V., Lodenquai, J., & Ruderman, M. 1971, Phys. Rev. D, 3, 2303
Daugherty, J. K., & Harding, A. K. 1982, ApJ, 252, 337
Daugherty, J. K., & Harding, A. K. 1986, ApJ, 309, 362
Daugherty, J. K., & Harding, A. K. 1989, ApJ, 336, 861
Daugherty, J. K., & Harding, A. K. 1996, ApJ, 458, 278
den Hartog, P. R., Kuiper, L., & Hermsen, W. 2008a, A&A, 489, 263
den Hartog, P. R., Kuiper, L., Hermsen, W., Kaspi, V. M., Dib, R., Knödlseder, J., & Gavriil, F. P. 2008b, A&A, 489, 245
Dermer, C. D. 1990, ApJ, 360, 197
Duncan, R. C., & Thompson, C. 1992, ApJ, 392, L9
Dyks, J., & Rudak, B. 2000, A&A, 360, 263
Gaensler, B. M. 2004, Adv. Space. Res., 33, 645
Goldreich, P., & Julian, W. H. 1969, ApJ, 157, 869
Gonthier, P. L., Harding, A. K., Baring, M. G., Costello, R. M., & Mercer, C. L. 2000, ApJ, 540, 907
Götz, D., Mereghetti, S., Tiengo, A., & Esposito, P. 2006, A&A, 449, L31
Gradshteyn, I. S., & Ryzhik, I. M. 1980, Table of Integrals, Series and Products (New York: Academic)
Graziani, C. 1993, ApJ, 412, 351
Güver, T., Özel, F., & Göğüş, E. 2008, ApJ, 675, 1499
Güver, T., Özel, F., Göğüş, E., & Kouveliotou, C. 2007, ApJ, 667, L73
Haberl, F. 2007, Astrophys. Space Sci., 308, 181
Harding, A. K., & Daugherty, J. K. 1991, ApJ, 374, 687
Harding, A. K., & Lai, D. 2006, Rep. Prog. Phys., 69, 2631
Harding, A. K., & Muslimov, A. G. 1998, ApJ, 508, 328
Harding, A. K., & Muslimov, A. G. 2002, ApJ, 568, 862
Herold, H. 1979, Phys. Rev. D, 19, 2868
Herold, H., Ruder, H., & Wunner, G. 1982, A&A, 115, 90
Hibschman, J. A., & Arons, J. 2001, ApJ, 554, 624
Ho, C., & Epstein, R. I. 1989, ApJ, 343, 227

Ho, W. C. G., Chang, P., Kaplan, D. L., Mori, K., Potekhin, A. Y., & van Adelsberg, M. 2007, Adv. Space. Res., 40, 1432
Johnson, M. H., & Lippmann, B. A. 1949, Phys. Rev., 76, 828
Kaspi, V. M., Gavriil, F. P., Woods, P. M., Jensen, J. B., Roberts, M. S. E., & Chakrabarty, D. 2003, ApJ, 588, L93
Kuiper, L., Hermsen, W., den Hartog, P. R., & Collmar, W. 2006, ApJ, 645, 556
Kuiper, L., Hermsen, W., & Mendeź, M. 2004, ApJ, 613, 1173
Latal, H. G. 1986, ApJ, 309, 372
Lyutikov, M., & Gavriil, F. P. 2006, MNRAS, 368, 690
Melrose, D. B., & Parle, A. J. 1983, Aust. J. Phys., 36, 755
Melrose, D. B., & Zheleznyakov, V. V. 1981, A&A, 95, 86
Mereghetti, S., Götz, D., Mirabel, I. F., & Hurley, K. 2005, A&A, 433, L9
Molkov, S., Hurley, K., Sunyaev, R., Shtykovsky, P., Revnivtsev, M., & Kouveliotou, C. 2005, A&A, 433, L13
Mori, K., Ho, W. G., & Wynn, C. G. 2007, MNRAS, 377, 905
Nobili, L., Turolla, R., & Zane, S. 2008a, MNRAS, 389, 989
Nobili, L., Turolla, R., & Zane, S. 2008b, MNRAS, 386, 1527
Özel, F. 2001, ApJ, 563, 276
Pavlov, G. G., Bezchastnov, V. G., Mészáros, P., & Alexander, S. G. 1991, ApJ, 380, 541
Pérez-Azorn, J. F., Miralles, J. A., & Pons, J. A. 2005, A&A, 433, 275
Perna, R., Heyl, J. S., Hernquist, L. E., Juett, A. M., & Chakrabarty, D. 2001, ApJ, 557, 18
Rea, N., Zane, S., Turolla, R., Lyutikov, M., & Götz, D. 2008, ApJ, 686, 1245
Rea, N., et al. 2009, MNRAS, 396, 2419
Rudak, B., Dyks, J., & Bulik, T. 2002, in Proc. 270th WE-Heraeus Seminar on Neutron Stars, Pulsars, and Supernova Remnants, ed. W. Becker, H. Lesch, & J. Trümper (MPE Report 278; Garching bei München: MPE), 142
Ruderman, M. A., & Sutherland, P. G. 1975, ApJ, 196, 51
Rybicki, G. B., & Lightman, A. P. 1979, Radiative Processes in Astrophysics (New York: Wiley)
Shibata, S. 1995, MNRAS, 276, 537
Sina, R. 1996, PhD thesis, Univ. Maryland
Sokolov, A. A., & Ternov, I. M. 1968, Synchrotron Radiation (Oxford: Pergamon)
Sturner, S. J., Dermer, C. D., & Michel, F. C. 1995, ApJ, 445, 736
Takata, J., Shibata, S., Hirotani, K., & Chang, H-K. 2006, MNRAS, 366, 1310
Thompson, C., & Beloborodov, A. M. 2005, ApJ, 634, 565
Thompson, C., & Duncan, R. C. 1996, ApJ, 473, 332
Thompson, C., Lyutikov, M., & Kulkarni, S. R. 2002, ApJ, 574, 332
Tiengo, A., Göhler, E., Staubert, R., & Mereghetti, S. 2002, A&A, 383, 182
Vasisht, G., & Gotthelf, E. V. 1997, ApJ, 486, L129
Vink, J. 2008, Adv. Space. Res., 41, 503
Xia, X. Y., Qiao, G. J., Wu, X. J., & Hou, Y. Q. 1985, A&A, 152, 93
Zane, S., Nobili, L., & Turolla, R. 2011, in Proc. ICREA Workshop on The High-Energy Emission from Pulsars and Their Systems, ed. N. Rea & D. Torres (Springer Astrophys. Space Sci. Series; Berlin: Springer), 329
Zavlin, V. E., Shibanov, Yu. A., & Pavlov, G. G. 1995, Astron. Lett., 21, 149
Zhang, B., & Harding, A. K. 2000, ApJ, 532, 1150